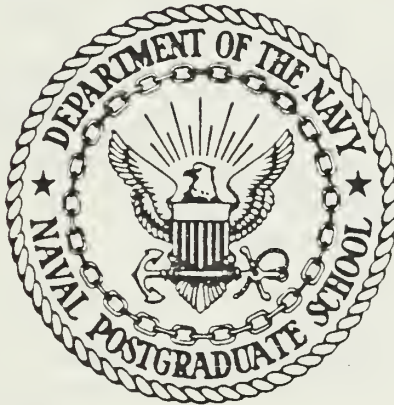


NEW YORK LIBRARY
AL POSTGRADUATE SCHOOL
TERRY, CALIFORNIA 95943-6002

NAVAL POSTGRADUATE SCHOOL

Monterey, California



THESIS

THERMAL IMAGE MEASUREMENTS
OF
INFRARED SIGNATURES

by

George Dimitriadis

December 1986

Thesis Advisor

A.W. Cooper

Approved for public release; distribution is unlimited.

T231552

REPORT DOCUMENTATION PAGE

REPORT SECURITY CLASSIFICATION UNCLASSIFIED		1b. RESTRICTIVE MARKINGS	
SECURITY CLASSIFICATION AUTHORITY		3 DISTRIBUTION/AVAILABILITY OF REPORT Approved for public release; distribution is unlimited	
DECLASSIFICATION/DOWNGRADING SCHEDULE			
PERFORMING ORGANIZATION REPORT NUMBER(S)		5 MONITORING ORGANIZATION REPORT NUMBER(S)	
NAME OF PERFORMING ORGANIZATION Naval Postgraduate School	6b OFFICE SYMBOL (If applicable) 61	7a NAME OF MONITORING ORGANIZATION Naval Postgraduate School	
ADDRESS (City, State, and ZIP Code) Monterey, California 93943-5000		7b. ADDRESS (City, State, and ZIP Code) Monterey, California 93943-5000	
NAME OF FUNDING/SPONSORING ORGANIZATION	8b OFFICE SYMBOL (If applicable)	9 PROCUREMENT INSTRUMENT IDENTIFICATION NUMBER	
ADDRESS (City, State, and ZIP Code)		10 SOURCE OF FUNDING NUMBERS	
		PROGRAM ELEMENT NO	PROJECT NO
		TASK NO	WORK UNIT ACCESSION NO
TITLE (Include Security Classification) THERMAL IMAGE MEASUREMENTS OF INFRARED SIGNATURES			
PERSONAL AUTHOR(S) Dimitriadis, George			
TYPE OF REPORT Master's Thesis	13b TIME COVERED FROM TO	14 DATE OF REPORT (Year, Month, Day) 1986 December	15 PAGE COUNT 119
SUPPLEMENTARY NOTATION This work was funded by NEPRE under Program 62759N, Project WF59-551 "ELECTRO_OPTICS, OPTICAL PROPAGATION, FLIR."			
COSATI CODES		18 SUBJECT TERMS (Continue on reverse if necessary and identify by block number)	
FIELD	GROUP	Thermal Measurement, Infrared Signatures,	
		Background Radiation, Reflected Sky Radiation	
ABSTRACT (Continue on reverse if necessary and identify by block number) Thermal images of an instrumented ship target against a sea background have been recorded under varying environmental conditions, using an AGA Thermovision 780 radiometric imaging system with digital data recording. Data were obtained in the 8 - 14 μ m spectral band at an angle of incidence of approximately 89° against the sea background. These pictures have been analysed together with measured target emissivity and meteorological parameters to give the temperature and radiance distributions of the target. The influence of reflected sky radiation on the background radiance was observed under varying sea surface conditions. A predictive model of effective radiance temperature difference of the target versus sea background in terms of the environmental parameters using the LOWTRAN 6 Radiance/Transmittance computer code was developed. This effective temperature difference has			
DISTRIBUTION/AVAILABILITY OF ABSTRACT <input type="checkbox"/> UNCLASSIFIED/UNLIMITED <input type="checkbox"/> SAME AS RPT <input type="checkbox"/> DTIC USERS		21 ABSTRACT SECURITY CLASSIFICATION unclassified	
NAME OF RESPONSIBLE INDIVIDUAL A.W. Cooper		22b TELEPHONE (Include Area Code) (408) 646 2452	22c OFFICE SYMBOL 61Cr

Block 19 contd.

been shown to vary both positively and negatively compared with the thermometric temperature difference depending on the wind speed and the air and sea surface temperatures.

Approved for public release; distribution is unlimited.

Thermal Image Measurements
of
Infrared Signatures

by

George Dimitriadis
Lieutenant, Hellenic Navy
B.S., Hellenic Naval Academy, 1978

Submitted in partial fulfillment of the
requirements for the degree of

MASTER OF SCIENCE IN ENGINEERING SCIENCE

from the

NAVAL POSTGRADUATE SCHOOL
December 1986

ABSTRACT

Thermal images of an instrumented ship target against a sea background have been recorded under varying environmental conditions, using an AGA Thermovision 780 radiometric imaging system with digital data recording. Data were obtained in the 8 - 14 μm spectral band at an angle of incidence of approximately 89° against the sea background. These pictures have been analysed together with measured target emissivity and meteorological parameters to give the temperature and radiance distributions of the target. The influence of reflected sky radiation on the background radiance was observed under varying sea surface conditions. A predictive model of effective radiance temperature difference of the target versus sea background in terms of the environmental parameters using the LOWTRAN 6 Radiance Transmittance computer code was developed. This effective temperature difference has been shown to vary both positively and negatively compared with the thermometric temperature difference depending on the wind speed and the air and sea surface temperatures.

TABLE OF CONTENTS

I.	INTRODUCTION	13
II.	TARGET AND BACKGROUND	16
	A. BACKGROUND RADIATION NOISE	16
	B. BACKGROUND RADIATION CONTRAST	17
	C. BACKGROUND SUPPRESSION	18
III.	BACKGROUND RADIANCE	20
	A. MARINE BACKGROUND	20
	1. Introduction	20
	2. Infrared Optical Properties of Sea Water	20
	3. Geometry of the Sea Surface	24
	4. Sea Water Temperature Distribution	25
	5. Properties of the Bottom Materials	26
	B. SPECTRAL RADIANCE OF THE SKY	27
	1. Introduction	27
	2. Atmospheric Emission	29
	3. Scattering of the Sky Radiation	32
IV.	ATMOSPHERIC TRANSMITTANCE	35
	A. ATMOSPHERIC PROPAGATION	35
	B. LOWTRAN 6 CODE	36
	1. General Description	36
	2. LOWTRAN 6 Input Data	36
	C. LOWTRAN 6 CODE USED IN THIS WORK	37
V.	FAMILIARIZATION WITH THE EQUIPMENT	38
	A. GENERAL	38
	B. AGA THERMOVISION 780	38
	1. Basic Description	38

2.	The Infrared Scanner	38
3.	Black and White Monitor Chassis	40
4.	Technical Data	42
5.	Digital Image Processing System	42
6.	DISCO 3.0 Software Description	42
C.	THERMAL MEASUREMENT TECHNIQUES	45
1.	Introduction	45
2.	Calibration Curves	45
3.	Basic Thermal Measurements	50
4.	Direct Measurement Procedure	50
D.	COMPLEX THERMAL MEASUREMENTS	53
1.	Introduction	53
2.	Variables Affecting the Measurement	53
3.	Exact Measurement Formula Derivation	53
VI.	EMPIRICAL CALIBRATION OF AGA THERMOVISION 780	56
A.	CALIBRATION PROBLEM	56
B.	THE CALIBRATION PROCESS	56
1.	General	56
2.	Blackbody Source	56
3.	Calibration	57
C.	CONCLUSIONS	58
VII.	SIGNATURE MEASUREMENTS	65
A.	GENERAL	65
B.	PARAMETERS FOR TEMPERATURE EVALUATION	67
1.	Atmospheric Transmittance	67
2.	Emissivity	67
3.	Atmospheric Air Temperature	69
4.	Ambient Temperature	69
C.	TEMPERATURE DATA EVALUATION AND PRESENTATION	70
D.	TEMPERATURE DATA ACCURACY	76
E.	RADIANCE CALCULATION	78

VIII.	DATA ANALYSIS	84
A.	INTRODUCTION	84
B.	EFFECTIVE SEA SURFACE TEMPERATURE	84
1.	Sea Surface Radiance	84
2.	Reflectance of the Sea Surface	84
3.	Apparent Temperature Calculation	85
4.	Calculated Temperature Data Discussion and Presentation	86
C.	TARGET-TO-BACKGROUND TEMPERATURE DIFFERENCE	88
1.	Effective Temperature Difference	88
2.	Temperature Difference Data Discussion and Presentation	89
D.	CALCULATION EXAMPLE	90
1.	Introduction	90
2.	Apparent Sea Surface Temperature	91
3.	Effective Sea Surface Temperature	92
IX.	CONCLUSIONS AND RECOMMENDATIONS	100
A.	CONCLUSIONS	100
B.	RECOMMENDATIONS	101
APPENDIX A:	DATA ANALYSIS OF LATER MEASUREMENTS	102
1.	GENERAL	102
2.	CALIBRATION TEST	102
3.	MEASURED DATA	103
4.	DISCUSSION AND ANALYSIS OF THE RESULTS	108
5.	CONCLUSIONS AND RECOMMENDATIONS	109
APPENDIX B:	IN-BAND FLUX CALCULATION USING TI-59 PROGRAM	114
1.	GENERAL	114
2.	FORMULAE AND CONSTANTS	114
3.	PROCEDURE	115
4.	PROGRAM LISTING	115
	LIST OF REFERENCES	117
	INITIAL DISTRIBUTION LIST	118

LIST OF TABLES

1. AGA THERMOVISION 780 TECHNICAL CHARACTERISTICS	43
2. AGA THERMOVISION 780 LW CALIBRATION CURVE CONSTANTS	49
3. THERMAL RANGE 2 CALIBRATION TEMPERATURE MEASUREMENTS	59
4. THERMAL RANGE 5 CALIBRATION TEMPERATURE MEASUREMENTS	61
5. THERMAL RANGE 10 CALIBRATION TEMPERATURE MEASUREMENTS	63
6. INSERTED METEOROLOGICAL DATA AND ATMOSPHERIC TRANSMITTANCE	68
7. R/V "POINT SUR" TEMPERATURE MEASUREMENTS "A"	71
8. R/V "POINT SUR" TEMPERATURE MEASUREMENTS "B"	72
9. R/V "POINT SUR" TEMPERATURE MEASUREMENTS "C"	73
10. R/V "POINT SUR" TEMPERATURE MEASUREMENTS "D"	74
11. R/V "POINT SUR" TEMPERATURE MEASUREMENTS "E"	75
12. THERMOCOUPLE - AGA THERMOVISION TEMPERATURE COMPARISON	77
13. R/V "POINT SUR" RADIANCE MEASUREMENTS "A"	79
14. R/V "POINT SUR" RADIANCE MEASUREMENTS "B"	80
15. R/V "POINT SUR" RADIANCE MEASUREMENTS "C"	81
16. R/V "POINT SUR" RADIANCE MEASUREMENTS "D"	82
17. R/V "POINT SUR" RADIANCE MEASUREMENTS "E"	83
18. BEAUFORT SCALE	91
19. SEA SURFACE TEMPERATURE AND EFFECTIVE ΔT "A"	94
20. SEA SURFACE TEMPERATURE AND EFFECTIVE ΔT "B"	95
21. SEA SURFACE TEMPERATURE AND EFFECTIVE ΔT "C"	96
22. SEA SURFACE TEMPERATURE AND EFFECTIVE ΔT "D"	97
23. SEA SURFACE TEMPERATURE AND EFFECTIVE ΔT "E"	98
24. THERMAL RANGE 2 NEW CALIBRATION TEMPERATURE DATA	104
25. THERMAL RANGE 5 NEW CALIBRATION TEMPERATURE DATA	106

26. SEA SURFACE TEMPERATURE AND EFFECTIVE ΔT "F"	110
27. SEA SURFACE TEMPERATURE AND EFFECTIVE ΔT "G"	111
28. SEA SURFACE TEMPERATURE AND EFFECTIVE ΔT "H"	112
29. TI-59 PROGRAM LISTING	116

LIST OF FIGURES

2.1	Radiation contrast for the 8-14 μm region	18
3.1	Sea surface radiance	20
3.2	Sea water absorption for selected wavelength regions	21
3.3	Absorption coefficient K of sea water versus wavelength	21
3.4	Transmittance and reflectivity of 0.003 cm of sea water	22
3.5	Index of refraction of water	23
3.6	Reflection from water surface at different incidence angles	23
3.7	Reflectance and emissivity of water	23
3.8	Reflectance from a flat ($\sigma = 0$) and roughened sea surface ($\sigma = 0.2$)	24
3.9	Sea surface radiance divided by sky radiance at zenith	26
3.10	Thermal structure of sea boundary layer	27
3.11	An idealized spectral radiance of the sky	28
3.12	Sky radiance for several elevation angles above horizon	30
3.13	Variation of zenith sky radiance with ambient temperature	31
3.14	Spectral emissivity of cloud layers of thickness ΔZ	33
3.15	Integral emissivity (E),absorptivity (A),transmittance (T)	33
3.16	Radiance of the under side of a cumulus cloud	34
3.17	Spectral radiance of sky covered with cirrus clouds	34
5.1	Dual scanner system	39
5.2	Simplified scanner unit block diagram	39
5.3	Arrangement of electro-optical components in a scanner	41
5.4	Black and White monitor chassis	41
5.5	Block diagram of DISCO 3.0 software	44
5.6	AGA LW calibration curves from -20°C to 50°C	46
5.7	AGA LW calibration curves from -20°C to 150°C	47
5.8	AGA LW calibration curves from 0°C to 1000°C	48
5.9	Monitor chassis front panel controls and indicators	51
5.10	Direct measurement method	52

5.11	Radiation conditions in complex measurement	54
6.1	Blackbody source used for calibration procedure	57
6.2	Thermal Range 2 calibration temperature measurements	60
6.3	Thermal Range 5 calibration temperature measurements	62
6.4	Thermal Range 10 calibration temperature measurements	64
7.1	Area where the signature measurements were taken	66
8.1	ΔT ratios plotted versus wind speed (m/s)	99
A.1	Thermal Range 2 new calibration temperature data	105
A.2	Thermal Range 5 new calibration temperature data	107
A.2	ΔT ratios plotted versus wind speed	113

ACKNOWLEDGEMENTS

This work was sponsored by the Naval Environmental Prediction Research Facility, Monterey, California under Program Element 6275N, Project WF59-551 "Electro-Optics, Optical Propagation, FLIR."

The author would like to express his sincere appreciation to the Hopkins Marine Station, Stanford University for providing laboratory facilities and to the Oceanography and Meteorology Departments at N.P.S for their cooperation.

The assistance of Professor E.C Crittenden and Lab Technician Bob Sanders was much appreciated. The guidance of Professor A.W Cooper insured that the present work is complete.

I. INTRODUCTION

Every object in our environment emits thermal radiation. The peak energy of this radiation is characteristic of the object's temperature and, for temperatures commonly found in our environment, is concentrated mostly in the infrared region of the electromagnetic spectrum. This physical phenomenon has found many applications since the second world war as it enables passive detection of targets by their self-emission alone.

Passive search, detection, identification and tracking have always been of great importance in naval warfare. Also, the necessity to improve our combative capabilities in areas where radar performance is degraded (low flying small cross section targets) is imminent. Infrared technology promises much in this area. The rapid growth of technology in solid state integrated circuits, microprocessors, infrared detectors and the better understanding of infrared physics during the recent decades has made it possible for sophisticated infrared systems to be designed and developed.

A very important step in designing an infrared optical system is the knowledge of the spatial and spectral radiances of the target and its background as well as the atmospheric effects on the emitted thermal radiation. Almost always, targets appear against a background that complicates the detection process since radiation from objects surrounding the target is confused with radiation emitted or reflected from the target. In the analysis of thermal imaging systems the target-to-background radiance contrast is frequently described by the equivalent temperature difference. In the case of observation at low elevation angles above the sea surface the surface radiance is strongly influenced by the reflection of the radiation emitted by the sky. The actual thermometric temperature difference is no longer a good representation of the radiance contrast. An "effective temperature difference" can however be defined taking into account the reflected radiation. Any new information and additional data about background scenes will improve the understanding of these effects and may be used to optimize computer algorithms or to implement new or improved techniques in signal processing to minimize background effects, thus improving system capabilities and optimizing performance.

This thesis describes the collection and analysis of thermal images of an instrumented ship target and its background under various well defined environmental conditions, followed by the development of a model for the effective target-to-background temperature difference. The target was the oceanographic ship R V "POINT SUR" and the background was sea surface and sky. The data were collected, stored, and processed using the "AGA 780 THERMOVISION", a liquid nitrogen cooled thermographic device with digital recording and data analysis hardware. All measurements were taken from a distance of about 650 meters using the Mercury Cadmium Telluride (HgCdTe) detector of the Thermovision 780 scanning system in the 8 - 14 μm spectral region. Five experiments were conducted during an operational oceanography student cruise on mid May 1986 and an adequate number of thermal image pictures was taken for various environmental conditions on certain dates.

Analysing these thermal images using the measured ship surface emissivity and the AGA software package, both the radiance and the effective temperature distributions of the ship were obtained. The atmospheric transmittance for this purpose was computed using the LOWTRAN 6 code, and the emissivity was measured from samples of the ship paint. The effective sea surface temperature was also obtained from these pictures. It was observed that the apparent sea surface temperature was affected by reflected sky radiation, and a model was developed to describe the effective target-to-background temperature difference under varying environmental conditions.

Later, three more experiments were conducted in mid November 1986 in order to obtain further, more accurate, data under different environmental conditions, after the Thermovision had been calibrated. This was done to check the previous results and improve the information on the reflected sky thermal radiation and the effective target-to-background temperature difference relation.

The present work consists of eight chapters. In the first chapter we state the background problem. In the second chapter we discuss the background radiances which affected our measurements, the marine background and the sky background. The atmospheric propagation problem and the LOWTRAN code used to find the atmospheric transmittance for the various environmental conditions are discussed in chapter three. Chapter four provides a familiarization with the equipment used to collect the data. In the fifth chapter we describe the calibration problem and discuss the derivation of the empirical calibration relations. In the sixth chapter we discuss how the thermal data we had collected were analyzed to give the temperature and

radiance distribution of the target. A further analysis of these data, to see how the sea background radiance was affected by reflected sky thermal radiation, is given in Chapter seven. In this chapter we also calculate the apparent sea surface temperature based on environmental parameters and compare the target-to-background temperature difference sensed by our detector with the actual thermometric temperature difference measurements. In the last chapter we discuss our conclusions and recommendations for further work. The discussion and analysis of the data obtained during the mid November measurements are given in Appendix A. In Appendix B the TI-59 program used to get the in-band radiant flux for the radiance calculations is explained.

The results of this work will lead to a better understanding of the background effects and may add some information to be used for the implementation of techniques in signal processing.

II. TARGET AND BACKGROUND

A. BACKGROUND RADIATION NOISE

Background radiation noise is noise generated in an optical detector by photon flux reaching it from all points other than the target. This kind of noise usually is separated into two components [Ref. 1]:

1. Temporal, which is due to fluctuations in the background emitted photons.
2. Spatial, which is due to background structural details.

The temporal background noise is generated by the fluctuation in the number of incident photons at the detector. This noise usually is referred to as background photon noise and is not directly related to the target. Detectors sensitive enough to experience background photon fluctuations noise are called BLIP (Background Limited Photon Detectors).

In this work we are interested in the spatial component of the background noise, produced by the structural content of the background and mainly related to the target. Therefore, from now on whenever we refer to background noise we will mean the spatial component.

Since a target is always surrounded by some sort of background it is obvious that radiation reaching our detector from this background is confused with the radiation emitted or reflected from the target. This is a serious problem that complicates the detection process and must be well understood for designing a high performance optical or infrared system. [Ref. 1]

Background radiation is due to thermal emission and reflected or scattered incident radiation. Many parameters affect this kind of radiation. Of high importance among them are the changes in emissivity and reflectance of the various background surfaces under varied environmental conditions. All the above make the background problem complicated and the modeling of a universal background function impossible.

Background radiance can be considered mainly as two categories:

1. Terrestrial background
2. Celestial background

Terrestrial background refers to radiance seen by infrared systems working within the atmosphere of the earth. This kind of background consists of radiation that several

surfaces of the earth are emitting or reflecting (oceans, clouds, vegetation, etc.). It also includes sunlight scattered by particles in the atmosphere and atmospheric molecular emission (sky radiance).

Celestial refers to that background seen by a system working in space and consists of radiation from the stars and the sun reflectance from planets and space debris.

Of particular interest in this work are the background radiances of the sea surface and the sky. Detailed discussion of these backgrounds and their spectral radiance characteristics, especially for the spectral region of 8 to 14 μm , where we have taken our measurements, is given in Chapter III.

Since target and background radiances travel through the atmosphere to reach the detector, they are heavily influenced by the atmospheric absorption under various meteorological conditions. Detailed analysis of the atmospheric effects on thermal radiation is given in Chapter IV.

B. BACKGROUND RADIATION CONTRAST

The target-to-background temperature difference is an important factor in the target detection probability of an infrared system. The higher the temperature difference between a target and its background, the greater the distance and the probability of detection.

This temperature difference or radiance difference is usually expressed with the quantity *Radiation Contrast*, C_R , defined in [Ref. 2] as

$$C_R = \frac{W_T - W_B}{W_T + W_B} ,$$

where W_T , and W_B are the target (T) and background (B) radiant emittances (W/m^2).

The 8 to 14 μm wavelength radiation contrast versus target-to-background temperature difference for different background temperatures is shown in Fig 2.1 .

When the temperature difference between the target and its background is very small, or goes to zero, the radiation contrast goes to zero and the detection becomes very difficult if not impossible. This effect is known as the washout effect and happens for "ambient temperature" targets twice a day due to the solar cycle.

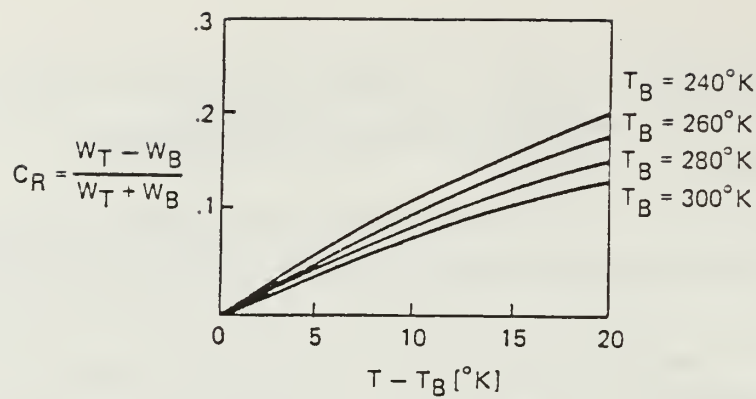


Figure 2.1 Radiation contrast for the 8-14 μm region.

In [Ref. 3] Hudson describes an experiment where the importance of the contrast effect is shown. In that experiment a vehicle parked in an open field was viewed by an infrared optical system over a period of 24 hours. During that observation, contrast variations were found. In the afternoon the contrast was positive, since the vehicle heated by the sun was warmer than its background. Later in the early evening hours the contrast was higher, since the vehicle with larger thermal capacity cooled more slowly than the background. As the night progressed, the contrast passed through zero and went negative, since the vehicle continued to cool rapidly and at some time became colder than its background. During the morning the negative contrast was still present because the background was warming more rapidly. After some hours the heating of the vehicle was enough to give a period of zero contrast and then turned to positive values again.

Hence, twice in a 24 hour period we are lacking sufficient contrast level between the target and its background, which means that the detection of any target at these periods is not possible, and since this effect can not be eliminated we have to utilize other methods of detection.

C. BACKGROUND SUPPRESSION

Target and background have different spectral radiances and different geometries, differences that make it easier for them to be distinguished. Whenever a spectral radiance difference exists between a target and its background an optical spectral filter can be used to reduce the unwanted background signals. Even if spectral filtering increases the target to background ratio, this is rarely sufficient to render a system

operational since usually the irradiance of the background is much higher than that of the target. A common characteristic of targets is that they are always smaller in angular extent than their backgrounds, a typical example being a ship against the sea. The differences in geometry between targets and background can be expressed as differences between their spatial frequency components. For such geometry differences, spatial filtering provides a good suppression of backgrounds of this extent relative to the target radiance.

Spatial filters include all types of reticles discussed in detail in [Ref. 3]. Spatial filtering is supplemented by spectral filters that define an effective spectral bandpass for the system and electrical filters that work on an average background threshold level to chop the background dc signal.

It is easily understood that spatial filtering is the basic suppression scheme mainly giving discrimination of the target in an extended background. But for many military systems, depending on the tasks they perform (identification, tracking, etc.), this is not enough. We have interference from other smaller kinds of background such as unwanted objects in the search area, for example buildings, rocks, clouds, etc. or unexpected objects crossing our detector's field of view such as birds, different kinds of ships, etc.

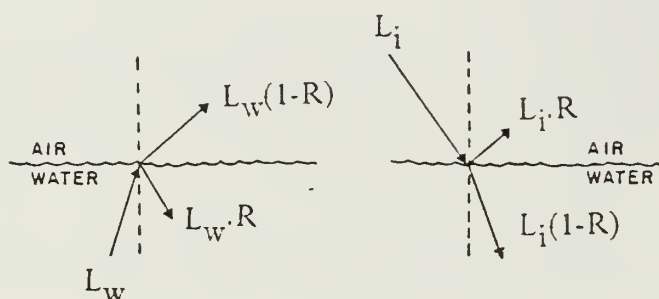
Therefore, more sophisticated and complicated spatial filtering systems have to be used for all the different purposes. These systems are supported by improved electronics and computer software, using different implementing techniques to minimize the background effects and optimize the system's performance.

III. BACKGROUND RADIANCE

A. MARINE BACKGROUND

1. Introduction

The sea surface infrared radiance (L_s) is the sum of the radiance caused by its thermal emission ($L_w(1-R)$) from below the surface and the radiance due to reflected incident radiation ($L_i.R$) (R : reflectance of the sea surface).



$$L_s = L_w(1-R) + L_i.R$$

Figure 3.1 Sea surface radiance.

Major factors that determine the marine background character are the following [Ref. 4]:

- Infrared optical properties of sea water
- Geometry of the sea-surface and wave slope distribution
- Sea water temperature distribution
- Properties of the bottom material .

2. Infrared Optical Properties of Sea Water

Thermal radiation from the sea surface occurs at wavelengths having their maxima close to the $10\text{ }\mu\text{m}$ region. As we can see in Fig 3.2 taken from [Ref. 5], at these wavelengths water is essentially opaque in thickness of about 0.02 mm . At wavelengths above $3.5\text{ }\mu\text{m}$ only the upper layers of the sea, of thickness about 0.01 cm and less, determine the sea surface thermal emission.

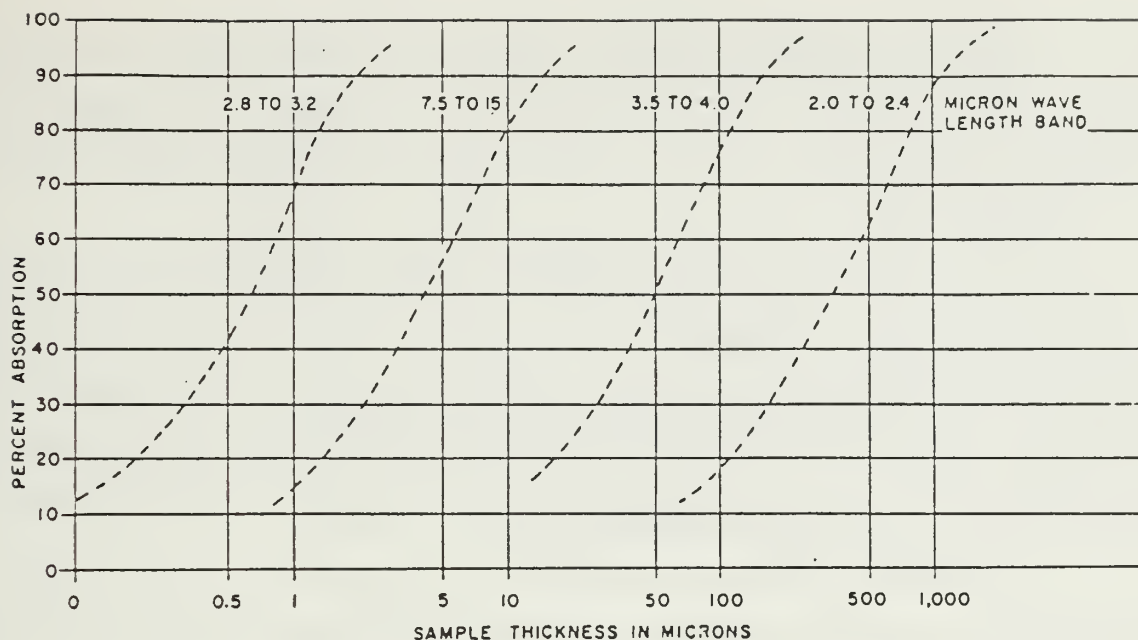


Figure 3.2 Sea water absorption for selected wavelength regions.

The radiation emitted from the sea surface is dependent on the underwater temperature profile, and is little affected by surface contamination. Since the emissivity is equal to the absorptivity the sea surface radiance is dependent on the distribution of the absorption coefficient K of the sea water as shown in Fig 3.3 .

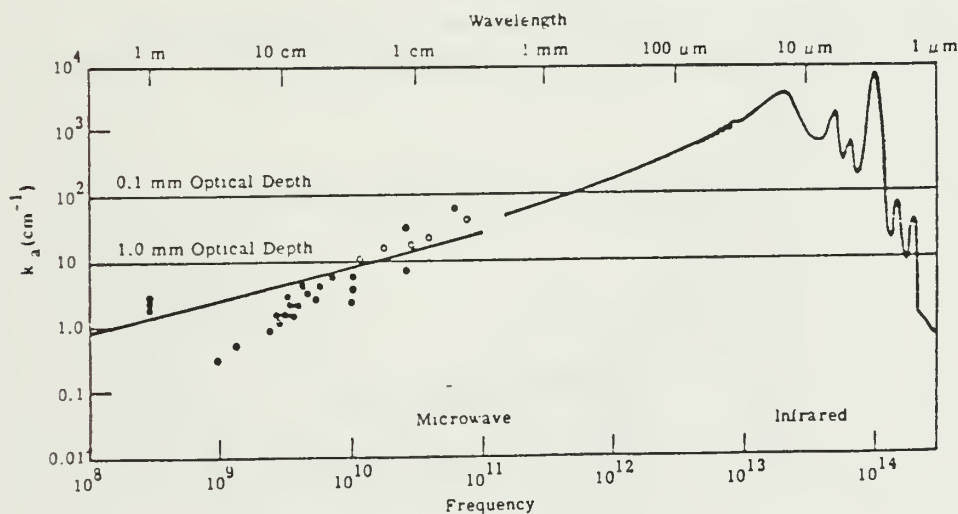


Figure 3.3 Absorption coefficient K of sea water versus wavelength.

Subsurface scattering of incident radiation is not significant in the infrared range, though it happens in the solar range ($0.35 - 3.0 \mu\text{m}$). In that region the absorption coefficient has a very low value and radiation penetrates deeply into the water and is scattered.

Reflected incident radiation is composed of solar radiation and sky thermal radiation. Solar radiation dominates at short wavelength and of course is present only in the daytime. In the region from $2 \mu\text{m}$ to $4 \mu\text{m}$ reflected solar emission especially at small angles of incidence is greater than the thermal emission of the sea surface. In comparison to this region only about 0.08 percent of the sun radiant energy is found in the region of $8 \mu\text{m}$ to $14 \mu\text{m}$ wavelengths, which means that only reflected sky thermal radiation influences this region by day and night.

The influence of reflected sky radiation was recognized by Mc Alister [Ref. 6] who found, for a clear sky at night, an apparent sea surface temperature a few tenths of a $^{\circ}\text{C}$ colder than the actual temperature.

Reflectance, transmittance, emissivity and index of refraction for water, are shown in Fig 3.4 to Fig 3.7 [Ref. 4]. Here we have to mention that distilled water and sea water transmittance do not have any significant difference.

For the purpose of this thesis, where we have worked in the 8 to $14 \mu\text{m}$ wavelength region, we have taken into account only reflected sky thermal radiation.

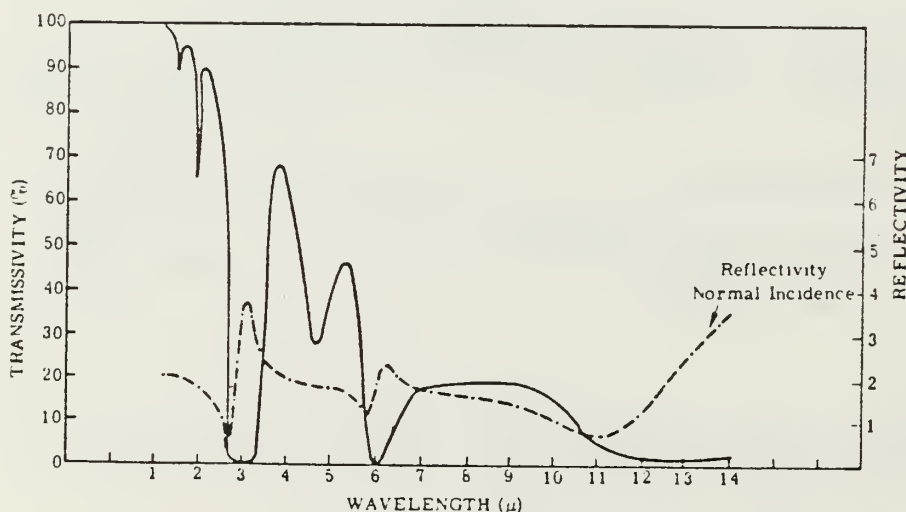


Figure 3.4 Transmittance and reflectivity of 0.003 cm of sea water.

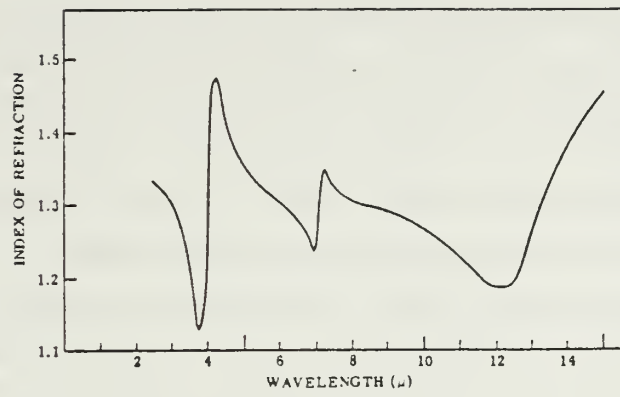


Figure 3.5 Index of refraction of water.



Figure 3.6 Reflection from water surface at different incidence angles.

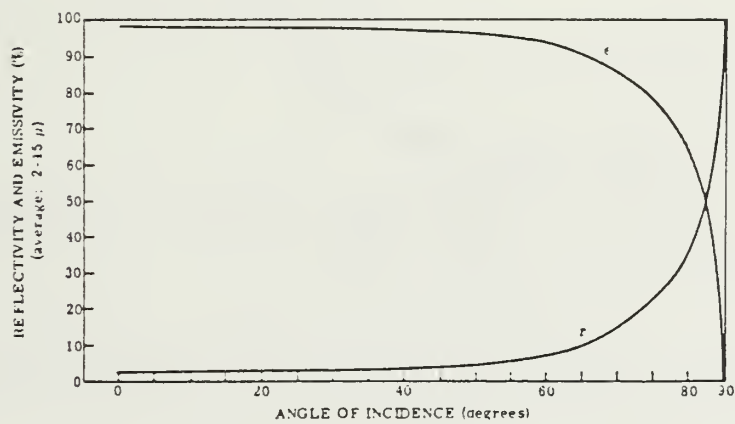


Figure 3.7 Reflectance and emissivity of water.

3. Geometry of the Sea Surface

The slope distribution of the waves is an important factor in the reflection and refraction of incident radiation on a roughened sea surface at various wind speeds. In Fig 3.8, taken from [Ref. 7], is shown the reflectance of solar radiation from a flat sea surface ($\sigma = 0$) and from seasurface roughened by a Beaufort 4 wind ($\sigma = 0.2$), where σ is the square root of the variance of the wave slope distribution. In this figure we can see that for an average rough sea (wind speed of Beaufort 4) the reflectance of the sea near the horizon goes to about 20% where as the reflectance of the flat surface is about 90% and above. Consequently we can see how high the emissivity ($1 - R$) of the roughened sea surface is near the horizon. Only at higher angles of incidence, about 40° , does the reflectance of the roughened sea surface go slightly higher than the reflectance of the flat surface.

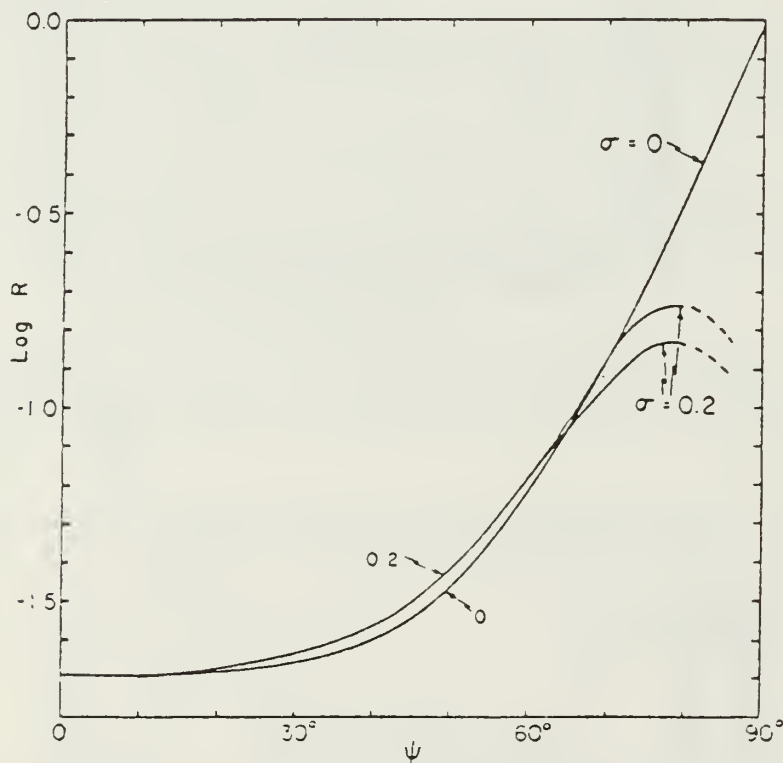


Figure 3.8 Reflectance from a flat ($\sigma = 0$) and roughened sea surface ($\sigma = 0.2$).

In [Ref. 7] Charles Cox and Walter Munk studied this phenomenon for solar radiation in the visible range. They assumed unpolarized sun light reflected once no double scattering. They used the index of refraction for uncontaminated sea water as $n = 1.338$. for calculating the reflection coefficient. Information is lacking for the infrared wavelength region and for night conditions, but since the sky radiance variation is almost the same during the day and night, and the reflectance of the sea water in the visible region of electromagnetic spectrum at zero angle of incidence is almost equal to the average reflectance in the infrared region from $2\text{ }\mu\text{m}$ to $15\text{ }\mu\text{m}$ (see Fig 3.4) these curves are considered helpful. For the purpose of this thesis, we have used these curves shown in Fig 3.8 from [Ref. 7] after making a correction for the index of refraction in the infrared range (8 to $14\text{ }\mu\text{m}$) we have used in our work. A detailed discussion of this is given in Chapter VIII.

The problem with these curves is that for the dashed portions near the horizon, above 80° angle of incidence, the function being used is not strictly applicable because of shadowing and multiple reflections. Also the lower and upper branches of the ($\sigma = 0.2$) curve represent two assumptions used in [Ref. 7] for the multiple reflection effect. The basic function used works for light reflected only once as we mentioned before. True values are expected according to C.Cox and W.Munk to lie between the indicated limits.

The curves in Fig 3.9 show the sea surface radiance $N(\mu)$ divided by the sky radiance $N_s(0)$ at the zenith, due to sun light scattering by air molecules, as a function of the vertical angle μ , for a clear sky and an overcast sky, and is also taken from [Ref. 7].

4. Sea Water Temperature Distribution

The sea surface temperature determines the emitted thermal radiation of the sea. This temperature is about 0°C (mainly about 4°C) in arctic regions and increases reaching about 29°C near the equator. Currents may produce anomalies of some degree in temperature. However the thermal emission of the sea surface has its maximum peak near the $10\text{ }\mu\text{m}$ wavelength. As we have said before in the infrared optical properties section, the temperature of the upper layers of the sea surface, of thickness about 0.01 cm , characterizes the thermal emittance.

Under evaporation conditions the temperature of the upper layer of 0.1 mm of the sea surface was measured [Ref. 4] as colder than the water temperature a few centimeters below the surface of about 0.6°C . In Fig 3.10 [Ref. 4] are shown

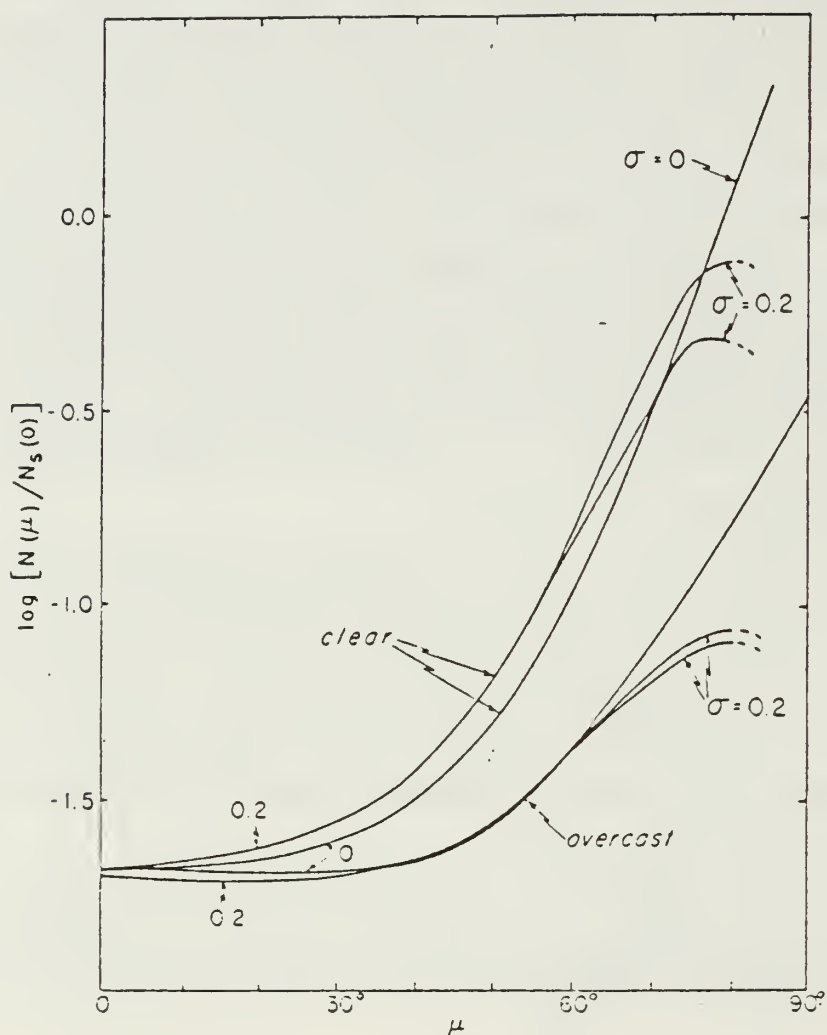


Figure 3.9 Sea surface radiance divided by sky radiance at zenith.

measurements of typical conditions showing the sharpest gradient in the upper layer of 1 nm.

5. Properties of the Bottom Materials

These properties are important in regions of short wavelengths where radiation can penetrate deep into the water causing subsurface scattering. Such properties are not important for the work done in this thesis, since we have worked in the region of longer wavelength (8 μm to 14 μm).

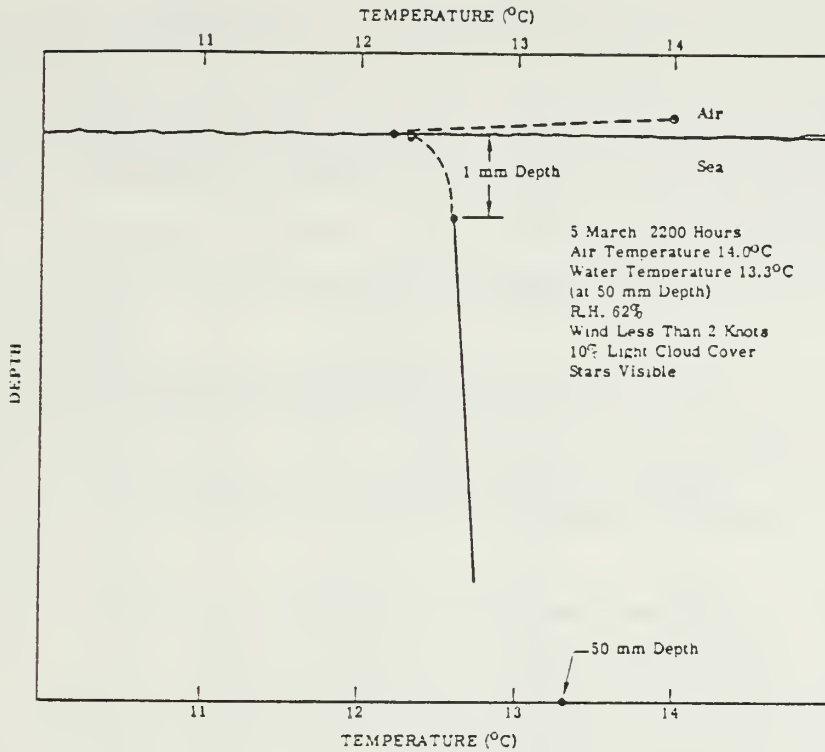


Figure 3.10 Thermal structure of sea boundary layer.

B. SPECTRAL RADIANCE OF THE SKY

1. Introduction

Sky background radiance in the infrared is caused by two different factors, the scattering of radiation from the sun and the thermal emission of the atmospheric constituents. The scattering factor is important in the short wavelength range, close to the visible, and is present only in daytime. The thermal emission happens at wavelengths longer than $4 \mu\text{m}$ and is present day and night.

An idealized form of this contribution to the sky spectral radiance is given in Fig 3.11 [Ref. 8]. This figure shows the spectral radiance of a blackbody at 300°K , close to the temperature of the earth, and the spectral radiance of a blackbody at 6000°K , close to the temperature of the sun. On estimating the sky radiance one can assume that the radiation from the sun is diffusely scattered and hence the sky appears to have a uniform radiant energy. This kind of maximum brightness, which has an average radiance about 2×10^{-5} times the radiance of the sun, can be approximated by a bright cloud shown as the lower dashed curve in the figure. But normally the sky

does not scatter this large amount of radiation; a nominal value is about one-tenth of this maximum spectral radiance, shown as the solid curve on the left, named "clear sky". So we can describe the combined effect of the thermal radiation emitted at the temperature of the earth and the scattered sunlight as combination of the two solid curves shown in this figure.

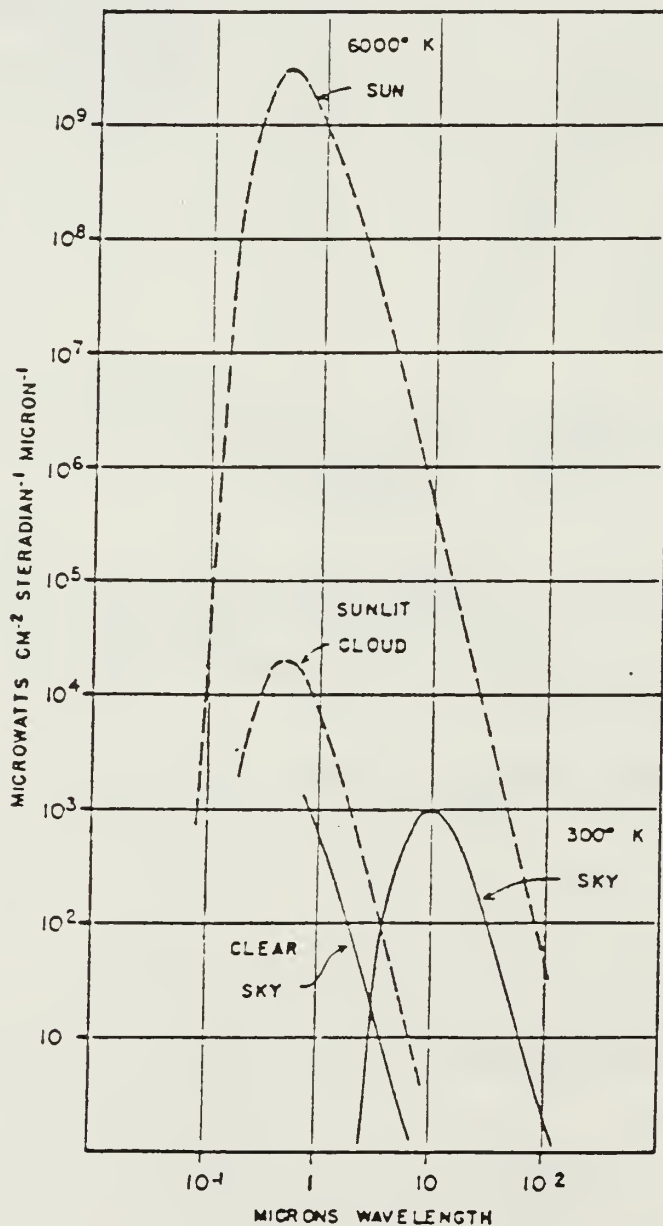


Figure 3.11 An idealized spectral radiance of the sky.

2. Atmospheric Emission

a. General

The atmospheric emissivity in the infrared depends on the amount of water vapor, carbon dioxide and other gases which give rise to absorption bands due to their vibrational and rotational transitions. Since the absorptivity equals the emissivity (Kirchhoff's law), we can predict the atmospheric emission from the absorption spectra of these gases.

b. Spectral Radiance of Clear Sky

Sky temperature and elevation angle are the main factors determining the radiance of a clear sky. The elevation angle determines the length of the atmospheric path and hence the emissivity, while the temperature determines the blackbody emission characteristics.

The effect of the elevation angle on spectral radiance is presented in Fig 3.12 [Ref. 8]. At low angles of elevation (near the horizon) we can see nearly blackbody radiation at the ambient temperature. But as the elevation increases above the horizon and the atmospheric path length decreases the optical density decreases and the emissivity is no longer blackbody ($\epsilon = 1$) everywhere. In the regions centered about $6.3 \mu\text{m}$ (water vapor absorption band) and about $15 \mu\text{m}$ (carbon dioxide absorption band) emissivity is very high, and the sky remains blackbody, even at the zenith (90°). But between these regions, in the region from about $8 \mu\text{m}$ to $13 \mu\text{m}$ the emissivity is poor and the sky is no longer black. The general background emission in this region is due to the wings of the water vapor and carbon dioxide bands. The peak that we see at about $9.6 \mu\text{m}$ is due to ozone emission, which increases as the elevation angle decreases from the zenith.

Fig 3.12, taken from [Ref. 8], shows spectra of clear sky radiance measured in September, at night, from a height of 11000 feet above sea level, at the ambient temperature of 8°C . The angles of elevation in sequence are 0° , 1.8° , 3.6° , 7.2° , 14.2° , 30° and 90° .

The effect of the ambient temperature is very strong for this kind of radiation, as shown in Fig 3.13 . This figure is also taken from [Ref. 8] and shows the zenith sky spectral radiance for two different ambient temperatures. The dashed curves are the spectral blackbody radiances corresponding to the ambient temperatures for the two separate measurements at 27.5°C and 2.5°C . These measurements were taken with different amounts of air mass, which affected the emissivity and hence the radiance of

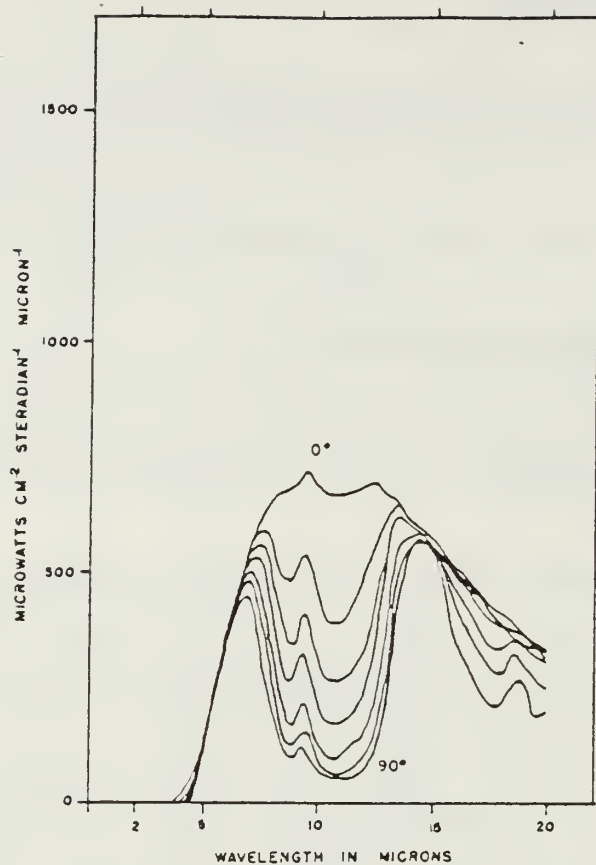


Figure 3.12 Sky radiance for several elevation angles above horizon.

the spectrum in the regions with poor emittance [Ref. 8]. The low temperature measurement was taken at 14110 feet above sea level and the higher temperature measurement at 6000 feet above sea level. The negative values shown are due to measurement error.

c. Spectral Radiance of an Overcast Sky

Overcast skies have been found to be very good blackbody radiators ($\epsilon = 1$), having a temperature at low altitudes within one or two $^{\circ}\text{C}$ from the ambient surface temperature [Ref. 8].

As mentioned before, water in the infrared is a good absorber (see Fig 3.3) with a small reflectivity. Clouds mostly at lower altitudes consist of water droplets with radii from $1\text{ }\mu\text{m}$ to about $10\text{ }\mu\text{m}$ at concentrations above 300 cm^{-3} with temperatures

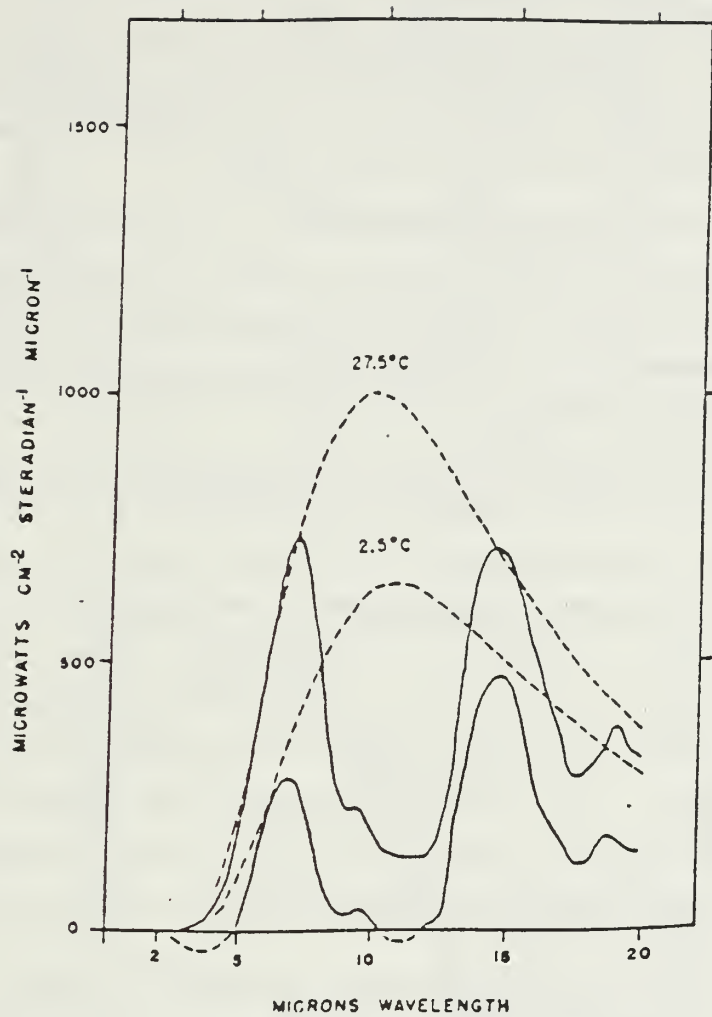


Figure 3.13 Variation of zenith sky radiance with ambient temperature.

not far from the surface temperature [Ref. 9]. So infrared radiation incident on a cloud water droplet is highly absorbed and partially reflected and transmitted. However due to multiple scattering from all neighbouring droplets in the cloud the transmittance of the cloud goes essentially to zero.

Hence we can say that clouds in the infrared region are good absorbers and consequently good emitters, causing overcast skies to behave as good blackbody radiators.

d. Spectral Radiance of Clouds

Clouds with thickness greater than 100 m and clouds with water droplet (or ice crystal for higher altitudes) counts greater than 0.5 g/cm^2 do not transmit. Thus absorptivity, and consequently emissivity, is high, approaching one, which means that clouds show a very good blackbody behavior [Ref. 10].

Fig 3.14 [Ref. 10] shows the emissivity of cloud layers versus wavelength and thickness ΔZ . Also in Fig 3.15 [Ref. 10] is shown how the integral emissivity (E), transmittance (T) and absorptance (A) changes with thickness ΔZ . Here we can clearly notice that at thickness ΔZ above 60 m the transmittance goes to zero and above 100 m the emissivity goes to zero.

However, looking at the spectrum of the under side of a cumulus cloud in a clear sky (Fig 3.16) at an elevation angle 14.5° [Ref. 8] we do not observe a blackbody spectrum . Since the emissivity of the cloud is expected to be high and since the sky is partially transparent in the region of $8 - 13 \mu\text{m}$ for the elevation angle of 14.5° , as shown before, we might expect to see clearly the emission of the cloud in that spectral region. From the figure we see that the emission in this region is characteristic of a blackbody at -10°C which is reasonable for the temperature of the cloud (lower dashed line in figure). What is really happening in this figure is that we have a combination of the atmospheric emission at the 6 and $15 \mu\text{m}$ wavelength regions from the path below the cloud together with the -10° blackbody emission from the cloud in the wavelength region at $8 - 13 \mu\text{m}$.

The effects of thin cirrus clouds in a clear sky modified situation is presented in Fig 3.18. Here we can see that the emission in region $8 - 13 \mu\text{m}$ has been raised in comparison with the clear sky situation (see Fig 3.13) , and also the ozone emission is reduced since it comes from a region higher than the clouds and is attenuated passing through them.

Fig 3.17, from [Ref. 8], shows spectra measured in June at sea level with an ambient temperature about 28°C . The elevation angles are 0° , 1.8° , 3.6° , 7.2° , 14.5° , 30° and 90° .

3. Scattering of the Sky Radiation

The position of the sun relative to the area of the observed sky and the length of the scattering path due to the elevation angle affect strongly the amount of scattered radiation. We have a large amount of scattering close to the sun direction as well as an increase in scattered radiance with a decreasing elevation angle. Decreasing the

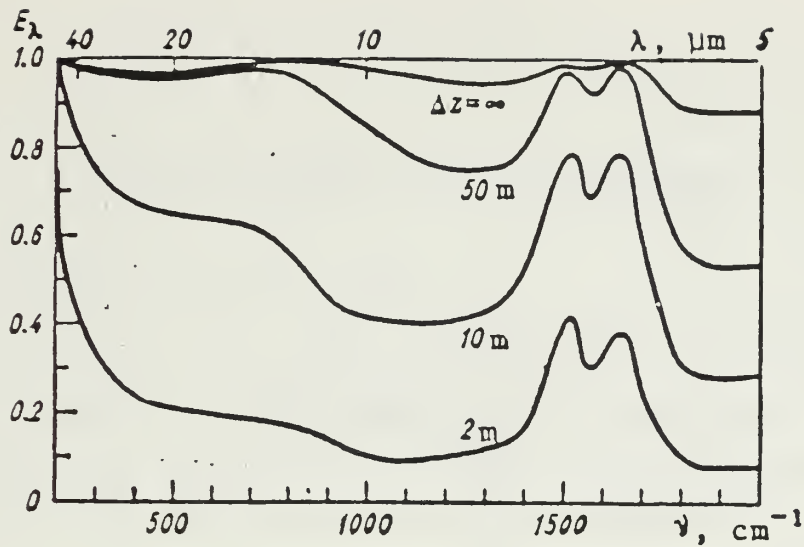


Figure 3.14 Spectral emissivity of cloud layers of thickness ΔZ .

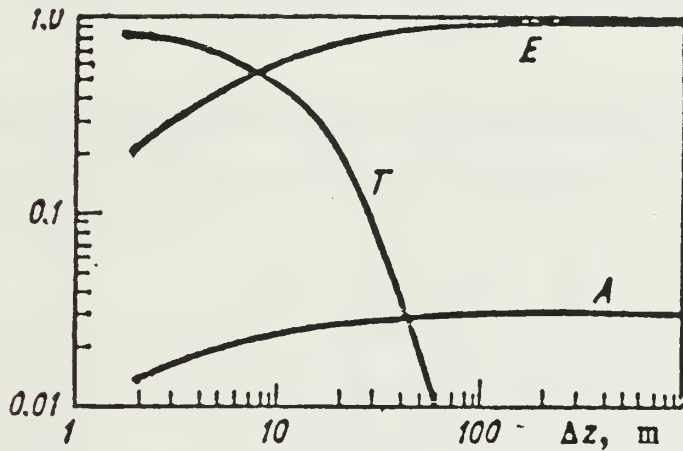


Figure 3.15 Integral emissivity (E), absorptivity (A), transmittance (T).

elevation angle we have a longer atmospheric path from which scattering can be produced. But very close to the horizon we have a reduction in the scattered radiance mainly because of water vapor absorption which reduces the effective observation path.

This kind of radiation is not important for the work done in this thesis since it occurs at short wavelengths.

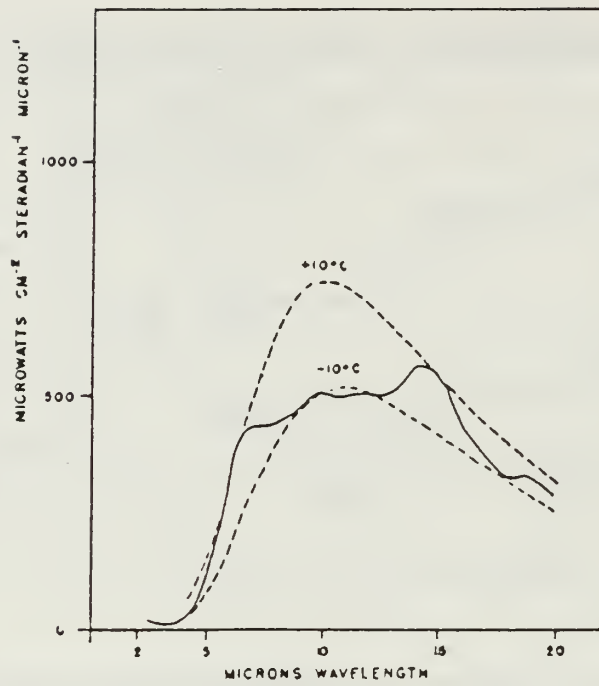


Figure 3.16 Radiance of the under side of a cumulus cloud.

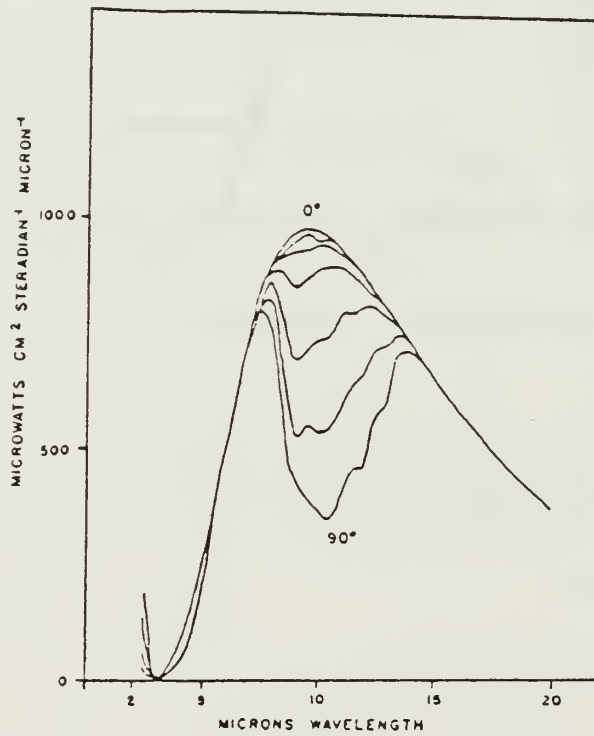


Figure 3.17 Spectral radiance of sky covered with cirrus clouds.

IV. ATMOSPHERIC TRANSMITTANCE

A. ATMOSPHERIC PROPAGATION

Thermal radiant flux from a target has to pass through the atmosphere of the earth before it reaches an infrared sensor. During this passage, the thermal radiation of the target is attenuated because of selective absorption due to several atmospheric gases and scattering by small particles suspended in the atmosphere, such as aerosols, rain, snow, smoke, fog and haze. Both absorption and scattering depend on wavelength (λ).

In general we call *atmospheric extinction* the process by which the radiant flux from a target is attenuated passing through the atmosphere. This can be expressed as:

$$\tau_A(\lambda) = e^{-\sigma(\lambda)R}$$

where $\tau_A(\lambda)$ is the atmospheric transmission, $\sigma(\lambda)$ is the extinction coefficient and R is the range. The extinction coefficient is the sum of the absorption coefficient $\alpha(\lambda)$ and the scattering coefficient $\gamma(\lambda)$

$$\sigma(\lambda) = \alpha(\lambda) + \gamma(\lambda)$$

Both absorption and scattering coefficients are sums of molecular and aerosol components [Ref. 2]. In the infrared region the absorption process is of greater importance (particularly in the 8 - 14 μm) than the scattering process which is important in the visible and near infrared region.

Water vapor, carbon dioxide and ozone are the most significant absorbing gases, having broad absorbing bands centered at the specified wavelengths: water vapor (2.7, 3.2, 6.3 μm), carbon dioxide (2.7, 4.3, 15 μm), ozone (4.8, 3.2, 6.3 μm). The bands of carbon dioxide at 2.7 and 15 μm and water vapor at 6.3 μm limit the atmospheric transmission in the infrared to two atmospheric windows at 3.5 to 5 μm and at 8 to 14 μm .

Infrared systems are designed to operate through these windows, and it is very important for the performance of our system to have a prediction of the atmospheric attenuation for the wavelength and the environmental conditions in which we are operating. This prediction process is a complicated problem and has been faced by computer modeling codes.

Such models are the high resolution models (HITRAN) and the low resolution model (LOWTRAN). The high resolution model codes provide direct computation with high resolution single frequency results. They are used to predict atmospheric attenuation for laser radiation. The low resolution model codes are used for a broad band prediction where the thermal systems work.

LOWTRAN code was used to predict atmospheric transmittance for the work done in this thesis and is considered in the next sections of this chapter.

B. LOWTRAN 6 CODE

1. General Description

LOWTRAN 6, the latest edition of the LOWTRAN simulation codes, is a FORTRAN computer curve-fitting program, relating empirical precomputed attenuation data to simple meteorological and environmental inserted parameters. It was designed to calculate average atmospheric transmittance and thermal radiance over a specified broad band, ranging from 359 to 40000 cm^{-1} (0.25 to 28.57 μm) with a resolution of 20 cm^{-1} averaging bandwidth in steps of 5 cm^{-1} .

The average transmittance is a function of the total extinction, the product of the transmittances due to water vapor line absorption, water vapor continuum absorption, uniformly mixed gases line absorption, nitrogen continuum absorption, aerosol absorption, aerosol scattering and molecular scattering. A consequence of the averaging over a finite spectral band is that the rapid fluctuations of the atmospheric transmittance in that band vanish.

Generally we can say that the LOWTRAN code is a fast but not very accurate computer simulation code.

2. LOWTRAN 6 Input Data

The LOWTRAN 6 code is activated by submitting four cards of sequential data. Each card provides data to be selected and asks for data values to be inserted as follows:

The first card provides a selection of six atmospheric models. These models are the tropical atmosphere, midlatitude summer, midlatitude winter, subarctic summer, subarctic winter and the 1962 U.S. standard atmosphere. Also in this card we have to indicate the type of atmospheric path (horizontal, vertical or slant), and determine the execution mode (transmittance - radiance).

The second card provides a selection of the type of extinction for nine boundary- layer aerosol models and gives a default meteorological range. These models are the rural (vis = 23 km), rural (vis = 5 km), navy maritime (computes visibility), maritime (vis = 23 km), urban (vis = 5 km), tropospheric (vis = 50 km), advection fog (vis = 0.2 km), radiation fog (vis = 0.5 km) and a user defined model (vis = 23 km). Also here we have to specify the air mass character for the navy maritime model and some meteorological conditions.

The third card defines the geometrical path and we have to insert some parameters like initial and final altitude, initial zenith angle and length of our path.

In the fourth card we have to specify the spectral range over which we want data for atmospheric transmittance or radiance and the frequency increment over which we want our data to be averaged.

A detailed description of the functions of these cards and the required input data is given in [Ref. 11].

C. LOWTRAN 6 CODE USED IN THIS WORK

For the work done in this thesis the LOWTRAN 6 code was used to find the atmospheric transmittance for the different meteorological conditions we experienced .

For our experimental conditions, mostly overcast skies and ambient temperatures about 10°C to 16°C we selected the midlatitude winter (45° N, January) atmospheric model for horizontal path. Also for the purpose of this work the navy maritime boundary layer aerosol model was selected. And thus because this model takes into account the existence of three components in determining the aerosol population. First is the *continental* component which is sensitive to the amount of time the air mass has spent over the sea; Second is the *stationary* component which depends on the wind history and represents aerosols formed by high winds and whitecap conditions, and the third one is the *fresh* component which is characterised by the current wind speed and consists of whitecap produced droplets. For our geometrical path we inserted target altitude 10 m and horizontal path length 650 m. Our spectral range was 710 - 1250 cm⁻¹ (8 - 14 μm) with frequency increment 5 cm⁻¹.

The results of these calculations are discussed in Chapter VII.

V. FAMILIARIZATION WITH THE EQUIPMENT

A. GENERAL

As mentioned in the introduction, all our data for this work were collected, stored and processed using the AGA Thermovision 780 system, supplemented with a digital microcomputer.

The system is designed for both thermal imaging and image analysis. It combines real infrared scanning with thermal image measurement capabilities and is supplemented by a microcomputer for digital image recording, storing and processing.

The particular system we used was a dual scanning system operating in the 3 - 5.6 μm and 8 - 14 μm windows with two different detectors. For the purpose of this experimental work only the 8 - 14 μm scanner was used.

B. AGA THERMOVISION 780

1. Basic Description

The AGA Thermovision 780 system consists of a real time scanner, a black and white monitor chassis display and a digital microcomputer.

The real time infrared scanner is the unit that converts the thermal radiant energy emitted from a target to electronic video signals. These signals are amplified and transmitted through a cable to the display monitor chassis where with further amplification they produce a thermal image on a black and white screen. The amplified signal can also be fed to a color monitor through an interconnecting device in order to have a real time thermal image presentation. Finally video and data signals are transmitted through an interconnecting link to a microcomputer. Here the thermal image is displayed in color and can be recorded, stored on a data disk and processed for temperature evaluation using color codes.

2. The Infrared Scanner

There are two kinds of scanning unit used in this system, the short wave (SW) scanner that operates in the 3 to 5.6 μm spectral band and the long wave (LW) scanner that operates in the 8 to 14 μm band. Scanner systems are designed with single or dual scanner units which cover both bands simultaneously. Our scanner as we have already mentioned was a dual type. Such a scanner system is shown in Fig 5.1.

Each scanner unit consists of the following parts :

- a. Electro-optical scanning mechanism

- b. Infrared detector
- c. Liquid nitrogen dewar for cooling the detector
- d. Control electronics and preamplifier

A simplified block diagram of the scanner unit is shown in Fig 5.2.

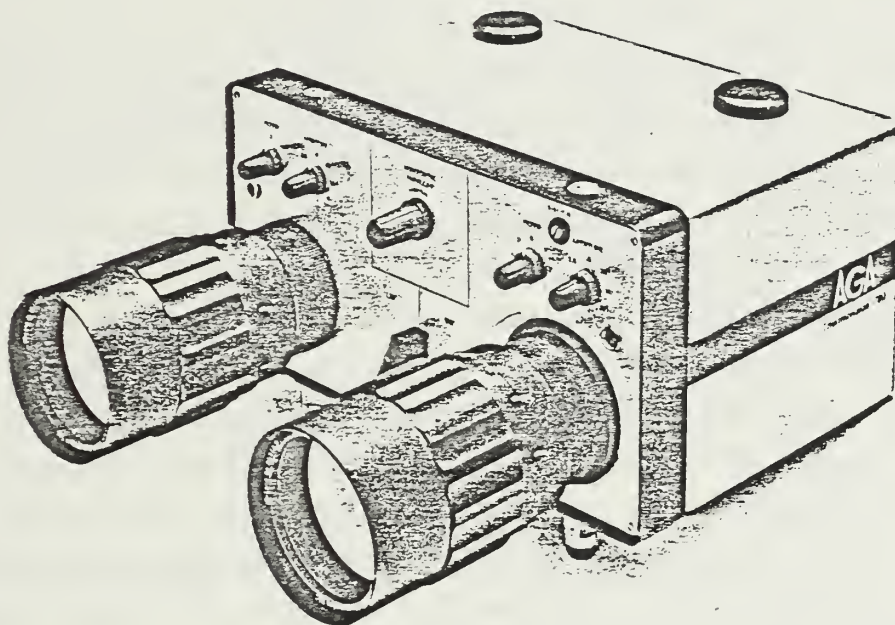


Figure 5.1 Dual scanner system.

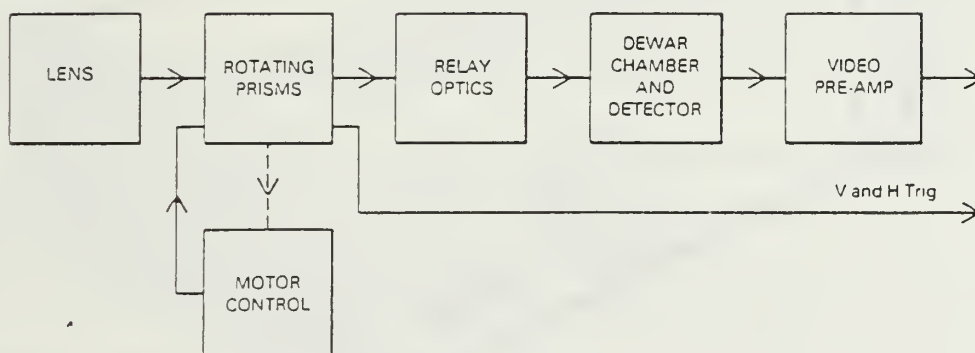


Figure 5.2 Simplified scanner unit block diagram.

Electromagnetic thermal energy emitted from a target is focussed by infrared lenses into a vertical prism. The lenses for the short wavelength band (SW) are made of silicon and those of the long wavelength band (LW) are made of germanium. Both kinds are covered with proper antireflecting coatings. The vertical prism is rotated at 180 rpm and its optical output is passed through a horizontal prism which rotates at 18000 rpm.

Rotating slotted discs control the rotation of both prisms and are electronically connected to the horizontal and vertical triggering circuits to provide horizontal and vertical triggering pulses for the monitor. The horizontal and vertical prisms are synchronized in such a way that four fields each having 100 horizontal scanning lines produce one interlaced frame. Of these lines only 70 lines per field or 280 per frame are used as active imaging lines.

The output from the horizontal prism passes through a set of relay optics containing a selectable aperture turret with eight aperture discs between $f\ 1.8$ and $f\ 20$ ($f\ 1.8$ disc was selected for our case). It then passes through a filter unit (no filter for our case) and finally is focussed on a single detector located on the wall of the dewar chamber. The detectors are a photovoltaic Indium-Antimonide (InSb) for the short wavelength band and a photoconductive Mercury - Cadmium - Telluride (HgCdTe) for the long wavelength band. Both detectors are cooled with liquid Nitrogen which maintains the chamber at a temperature of -196°C .

The signal output from the detector is preamplified within the scanner unit and the video signal produced is applied through a cable to the black and white monitor chassis [Ref. 12].

The arrangement of the electro-optical components of a scanner unit is shown in Fig 5.3 [Ref. 12].

3. Black and White Monitor Chassis

The video output signal from the scanner unit is applied to the input connector of the black and white chassis. This signal after a further amplification and processing within the monitor is applied to the display screen.

Outputs from this monitor chassis are used for a color monitor connection and the interconnecting link for the microcomputer connection with the system.

A Black and White monitor chassis is shown in Fig 5.4 [Ref. 12].

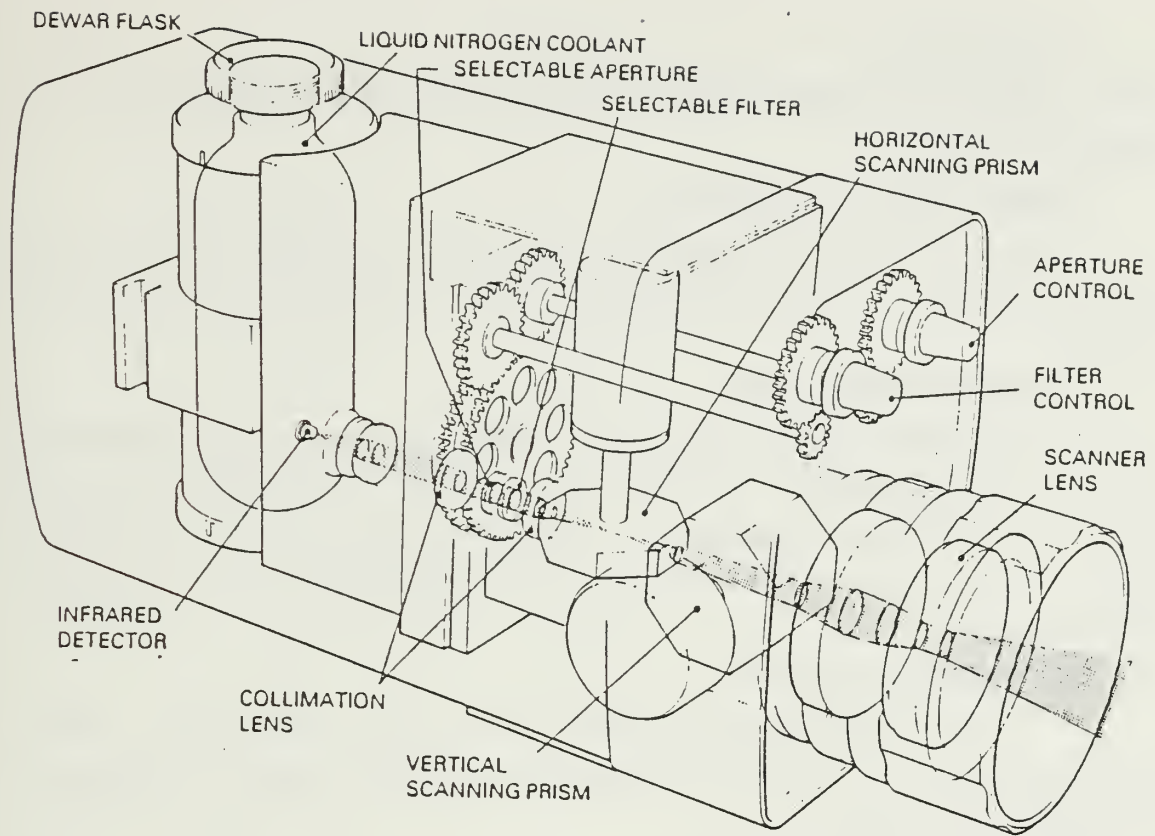


Figure 5.3 Arrangement of electro-optical components in a scanner.

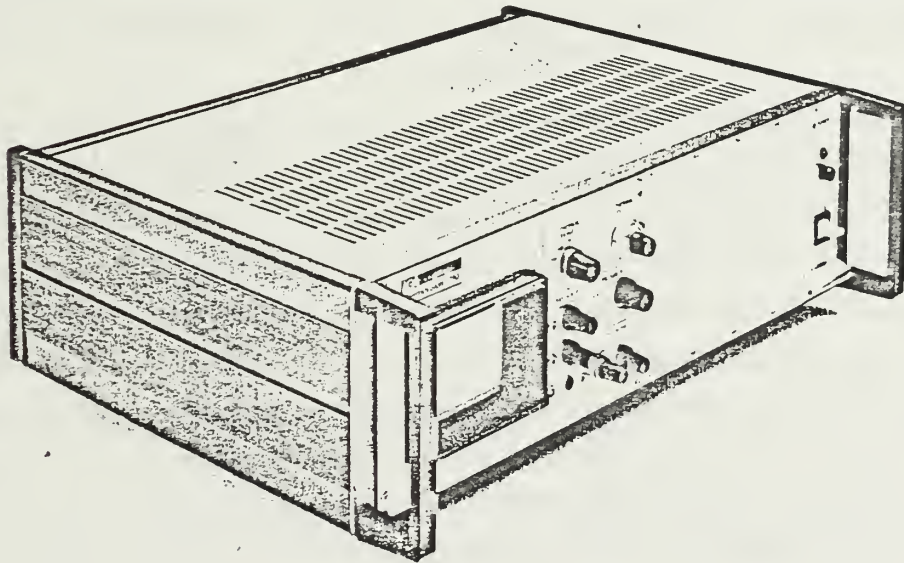


Figure 5.4 Black and White monitor chassis.

4. Technical Data

Technical data for the AGA Thermovision 780 were found in [Ref. 13] and are presented in Table 1.

5. Digital Image Processing System

This system supplements the AGA Thermovision 780 system and consists of an interconnecting link and the microcomputer which utilizes the systems software DISCO 3.0

a. Interconnecting Link

The interconnecting link is a digital on-line interface for direct interfacing between the Thermovision 780 and the IF 800 model 20 microcomputer. The main purpose is to digitize the image, hold the image data during the time required for transfer from the Thermovision to the microcomputer, and control the data transferring speed.

b. IF 800 Microcomputer

IF 800 is a business level personal computer which uses a Z-80A, 4 MHz clock microprocessor for its CPU. It comprises a keyboard, a printer, a display unit and a mini floppy disk drive.

6. DISCO 3.0 Software Description

The software used by this system consists of three main programs the DISCO, the IMAGE PROCESSING and the UTILITY programs. Various subprograms as shown in the DISCO 3.0 block diagram Fig 5.5 [Ref. 14] supplement the main programs.

The main program DISCO was the one mostly used for this work to record, store and process our data. Using this program infrared images were transferred from the Thermovision 780 system to the microcomputer. The subprogram F1 *Record Image* was used to record these thermal images and display them in color on the computer screen. Also this subprogram was used to enter or alter our parameters (emissivity, atmospheric transmittance etc.), to select and enter the scanner identification characteristics used and store the images on a data disk. The subprogram F2 *Evaluate Image* was used to evaluate the temperature measurement of the image using color scaling with tables of 3 to 36 different color combinations. Each color was assigned a particular temperature range. The standard table of the system uses 8 colors and was the one used in our case. This subprogram was also used to display histograms with a frequency distribution of the temperature values, to display single

TABLE 1

AGA THERMOVISION 780 TECHNICAL CHARACTERISTICS

PERFORMANCE

Spectral Range	:	3 - 5.6 μm and/or 8 - 14 μm
Frame Rate	:	6.25 sec^{-1}
Field Rate	:	25 sec^{-1}
Interlace	:	4 : 1

REPLACEABLE FORE OPTICS

FOV Azimuth *	:	7°
FOV Elevation *	:	7°
IFOV Azimuth	:	1.1 mrad
IFOV Elevation	:	1.1 mrad
NEAT	:	0.12°C at 22°C
MDT	:	< 0.1°C
Dynamic Range	:	-20 to 900°C

OPTICAL DATA

Effective Aperture Area	:	24 cm^2
Aperture Diameter	:	5.5 cm
Effective Focal Length	:	9.9 cm
f/number	:	1.8

DETECTOR

Type SW	:	Photovoltaic InSb
LW	:	Photoconductive HgCdTe
Number of Elements	:	1
Peak Wavelength SW	:	5 μm
LW	:	10 μm

COOLING SYSTEM

Liquid Nitrogen	:	-196°C
-----------------	---	--------

* Note: The system can take five different fore lenses with FOV 3.5X3.5, 7X7, 12X12, 20X20, and 40X40. The lens we used was the one with FOV 7X7.

DISCO 3.0

Block Diagram

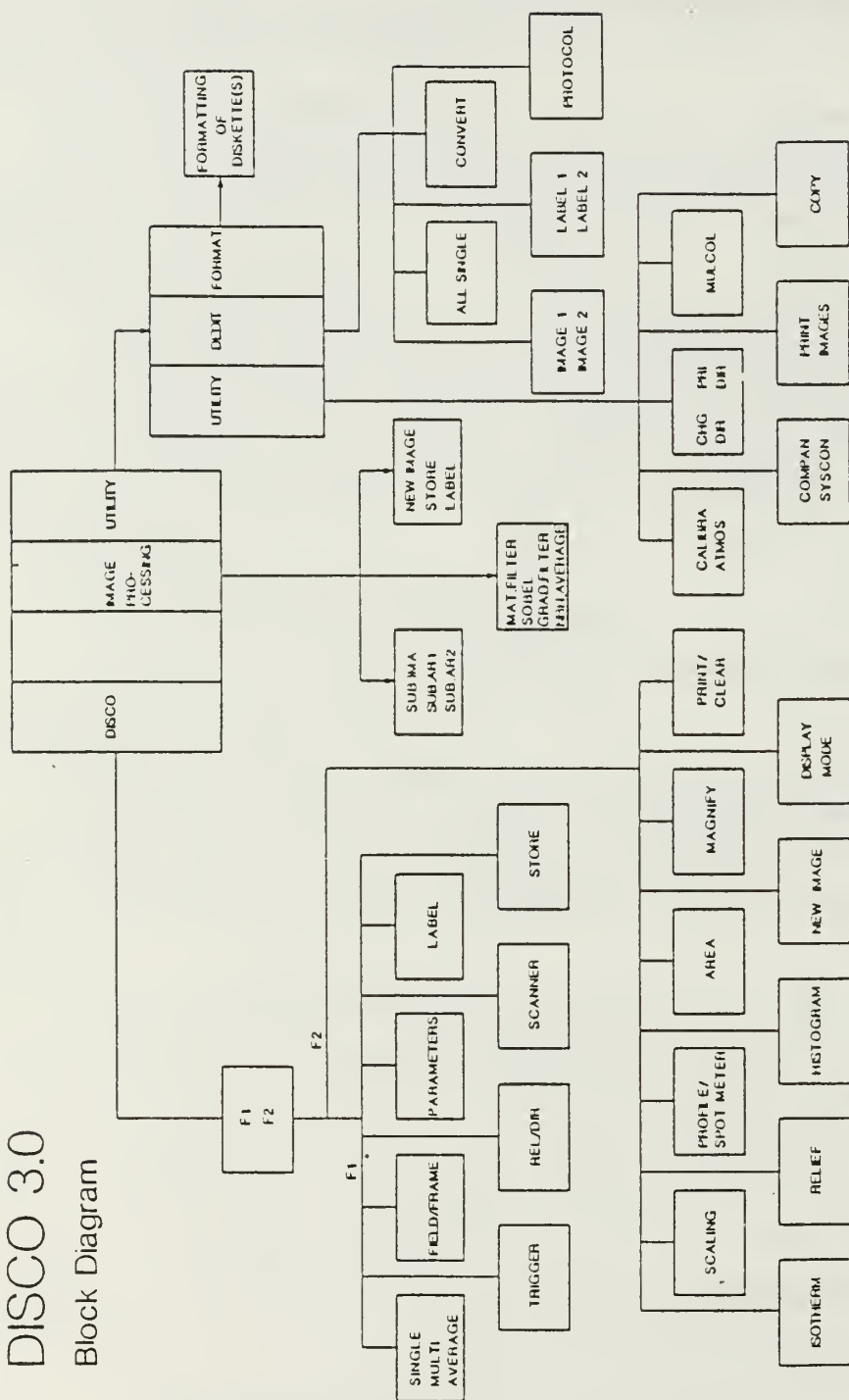


Figure 5.5 Block diagram of DISCO 3.0 software.

isotherms, magnify the image, transfer a new image on the display from those which had been stored on the data disk and print data such as temperature profiles using the system printer. For the last case our system had some limitations since the system's maximum capabilities are available only on a color printer which was not available.

C. THERMAL MEASUREMENT TECHNIQUES

1. Introduction

As we know the radiant flux density received by an infrared system does not have a linear relationship to the object temperature. It is always mixed with reflected or emitted background radiation and is attenuated by the atmosphere. Therefore, certain calibration and correction procedures have to be applied to a particular measurement in order to have an accurate temperature evaluation.

The AGA Thermovision 780 system measures thermal radiation between spectral limits as mentioned before. The numerical value of the received radiation is called the THERMAL VALUE and is measured in *Isotherm Units* (IU) which is an arbitrary unit system. This thermal value is proportional to the received photon flux density, but is not proportional to the temperature of the target. Therefore, we need a calibration function as a graphical curve or a computer program to relate the thermal value (isotherm units) with the temperature of the target.

2. Calibration Curves

Calibration curves for all aperture sizes used by the system in the long wavelength (LW) spectral band, in which we worked, are shown in Figs 5.6 through 5.8 [Ref. 12]. These curves have been obtained assuming emissivity $\epsilon = 1$ (blackbody radiator) and neglecting atmospheric damping $\tau_a = 1$. For situations different from the above it is obvious that we have to apply correction techniques.

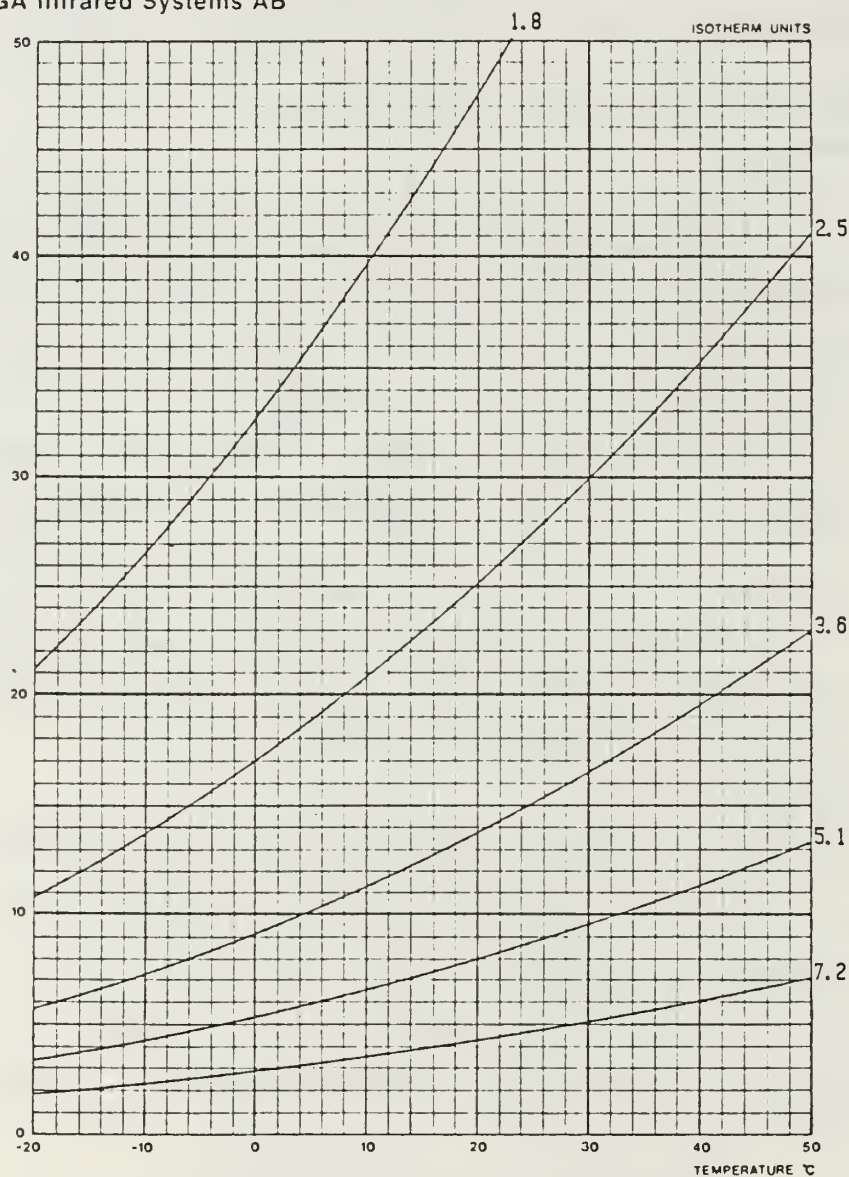
These calibration curves are accurately described by the following equation taken from [Ref. 12]

$$I = \frac{A}{C e^{(B/T)} - 1} , \quad (\text{eqn 5.1})$$

where I is the thermal value in isotherm units (IU) for the absolute temperature (T) in °K. A,B,C are calibration constants that depend on the aperture, filter, scanner etc.

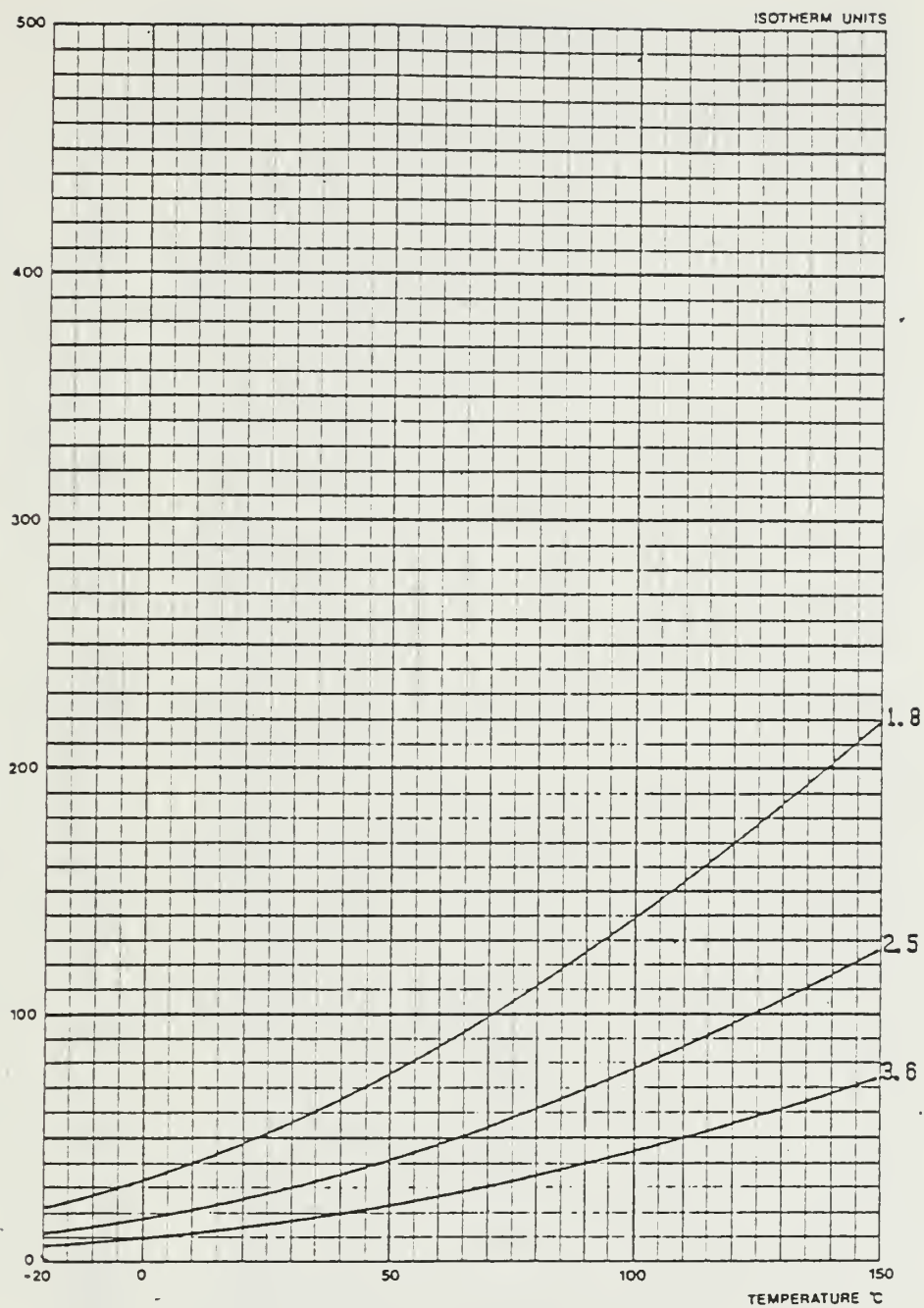
This equation was used by the microcomputer program to calculate the temperature of the target for a known thermal value after the calibration constants A,B,C for the LW shown in Table 2 had been inserted.

AGA Infrared Systems AB



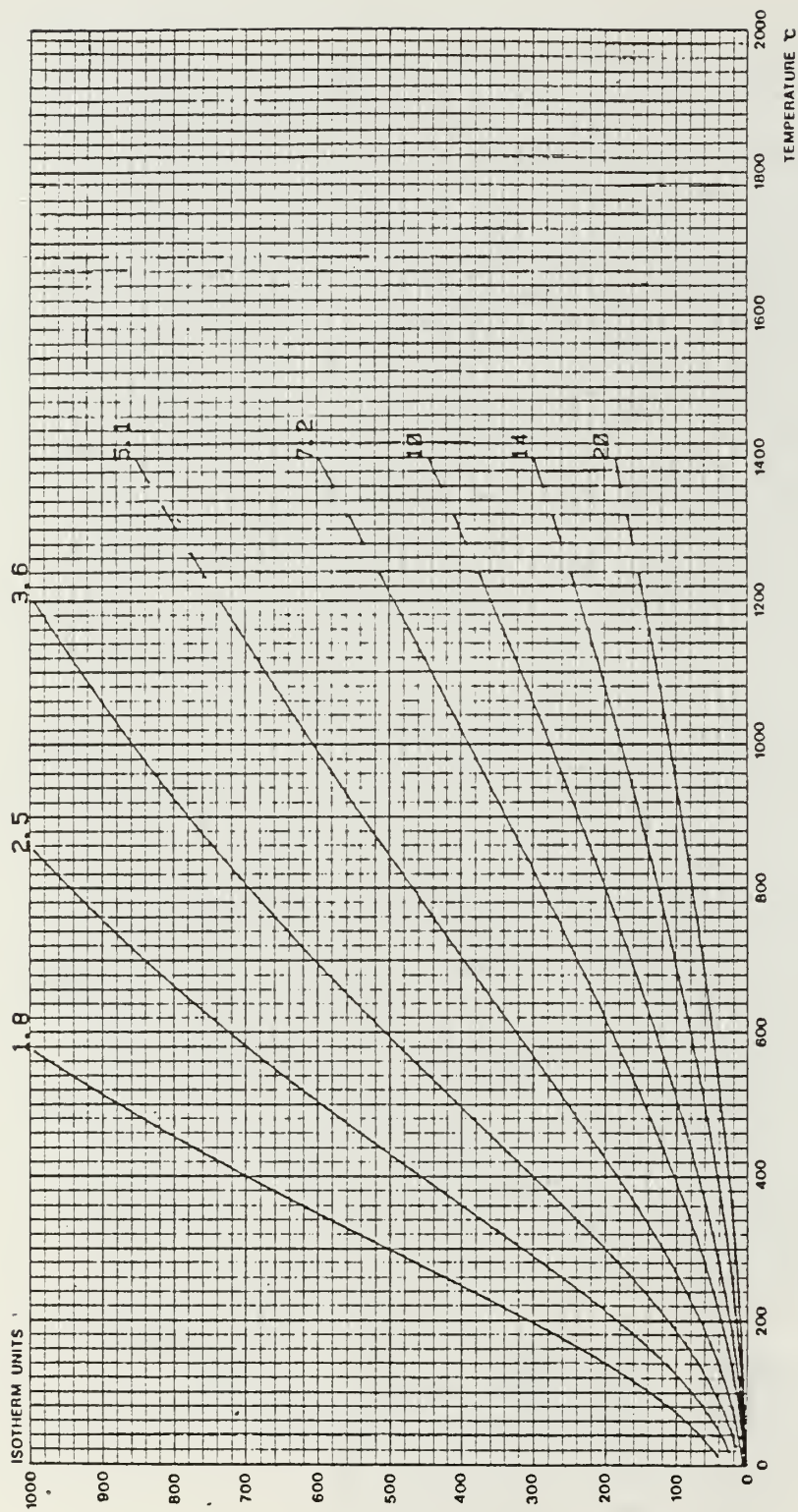
Scanner: LW08 4011 Date: 02-09-27 Operator: B.A
 Detector: G 1739 Ambient temp: 24 °C
 Filter: NOF Rel. humidity: 55 %
 Lens: 7 3105 Object distance: 1.0 m

Figure 5.6 AGA LW calibration curves from -20°C to 50°C.



Scanner: LYDB 4011 Date: 82-09-27 Operator: B. A
 Detector: G 1739 Ambient temp: 24 °C
 Filter: NCF Rel. humidity: 55 %
 Lens: 7. 3105 Object distance: 1.0 m

Figure 5.7 AGA LW calibration curves from -20°C to 150°C.



Scanner: LWDB 4011 Filter: NOF Date: 82-09-27 Rel. humidity: 55 % Operator: B. A
 Detector: G 1739 Lens: 7 3105 Ambient temp.: 24 °C Object distance: 1.0 m

Figure 5.8 AGA LW calibration curves from 0°C to 1000°C.

TABLE 2
AGA THERMOVISION 780
LW CALIBRATION CURVE CONSTANTS

INDIVIDUAL CALIBRATION OF 780 DUAL BBAR

SERIAL NUMBERS

SCANNER : LWDR 4011

DETECTOR : G 1739

FILTER : NOF

LENS : 7 3105

CALIBRATION CONDITIONS

AMBIENT TEMPERATURE : 24 C

RELATIVE HUMIDITY : 55 %

OBJECT DISTANCE : 1.0 m

CALIBRATION DATE : 82 - 09 - 27

CALIBRATION CURVE CONSTANTS

APERTURE	A	B	C
1.8	- 3581	1506.49	- 0.436
2.5	- 4060	1569.30	- 0.759
3.6	- 6514	1629.70	- 1.824
5.1	5420	1610.70	2.796
7.2	1123	1606.54	1.098
10.0	584	1604.29	0.885
14.0	306	1610.60	0.773
20.0	195	1650.51	0.767

3. Basic Thermal Measurements

There are two basic methods we can use to measure temperature using the thermovision 780. The *direct*, and the *relative* measurement method.

In the direct method of measurement the system built in capabilities (clamping and temperature compensation) permit measurement of the temperature of an object without using any other reference source of radiation.

In the relative measurement method the radiation of an external reference source with known temperature and emissivity is compared with the radiation received from the object to obtain the object temperature.

The direct method is easier to use but not as accurate as the relative method, which, however, has the disadvantage that it needs an accurate reference source to be available. In our case the direct method was used since we didn't have any reference source with known temperature and emissivity located near the target.

4. Direct Measurement Procedure

In this subsection we will describe briefly the procedure for the direct measurement method, using the Thermovision first alone and then supplemented with a microcomputer as was done to collect data for this work.

To aid in understanding this measurement procedure, the monitor chassis front panel controls and indicators are presented in Fig 5.9 [Ref. 12]. Subsequently a short description of the operation and function of the controls and indicators referred to in this measurement procedure is given.

- a. THERMAL RANGE (item 9): This is a nine position switch calibrated between 2 and 1000 isotherm units. This switch selects the thermal span of interest.
- b. THERMAL LEVEL (item 10): This control sets the thermal level of the image.
- c. PICTURE MODE "NORMAL" (item 12b): It selects the normal image display, where the cooler object temperature appears as black and the hotter as white.
- d. ISOTHERM LEVEL 1 (item 13): This control turns on the isotherm function and identifies the discrete thermal levels on the target. The isotherm function is indicated by saturated white areas, which represent areas of the same temperature. A marker on the vertical isotherm scale indicates the relative position of the selected level.
- e. ISOTHERM SCALE (item 16): This is a scale calibrated from -0.5 to +0.5. A reading of the isotherm marker multiplied by the thermal range gives the relative thermal value in isotherm units.

For both cases either with the thermovision itself or supplemented by the microcomputer, starting with picture mode in NORMAL, we have to adjust the THERMAL RANGE and LEVEL controls to obtain a good thermal picture. The

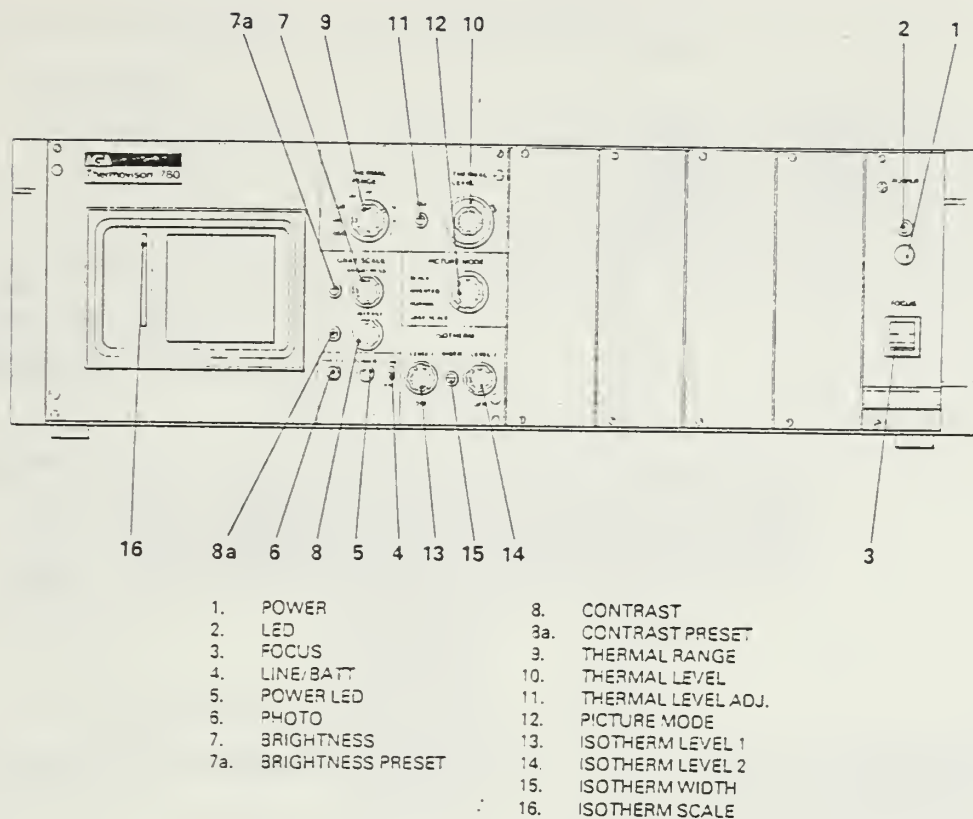


Figure 5.9 Monitor chassis front panel controls and indicators.

picture was shown on the Black/White monitor and on the color monitor used. The measurement procedure is shown schematically in Fig 5.10 [Ref. 12]. First with the THERMAL RANGE control switch we select the thermal span of interest in isotherm units (2 to 1000), about the thermal level of the image. In our case thermal ranges of 2, 5 and 10 isotherm units were selected. Then with the THERMAL LEVEL control knob we set the thermal level of the image. At the point at which a satisfactory thermal picture is obtained the corresponding thermal value "L" of the image in isotherm units, is measured (i.e., the thermal value of the isotherm scale at zero point, Fig 5.10).

Using the thermovision alone, the control ISOTHERM LEVEL 1 has to be adjusted to brighten up the point of interest on the target in view. A marker on the vertical scale indicates the relative position of the selected level. The reading of the isotherm marker multiplied by the thermal range gives the relative thermal value "i" in isotherm units, shown in Fig 5.10. Adding the two values "L" and "i" we have the

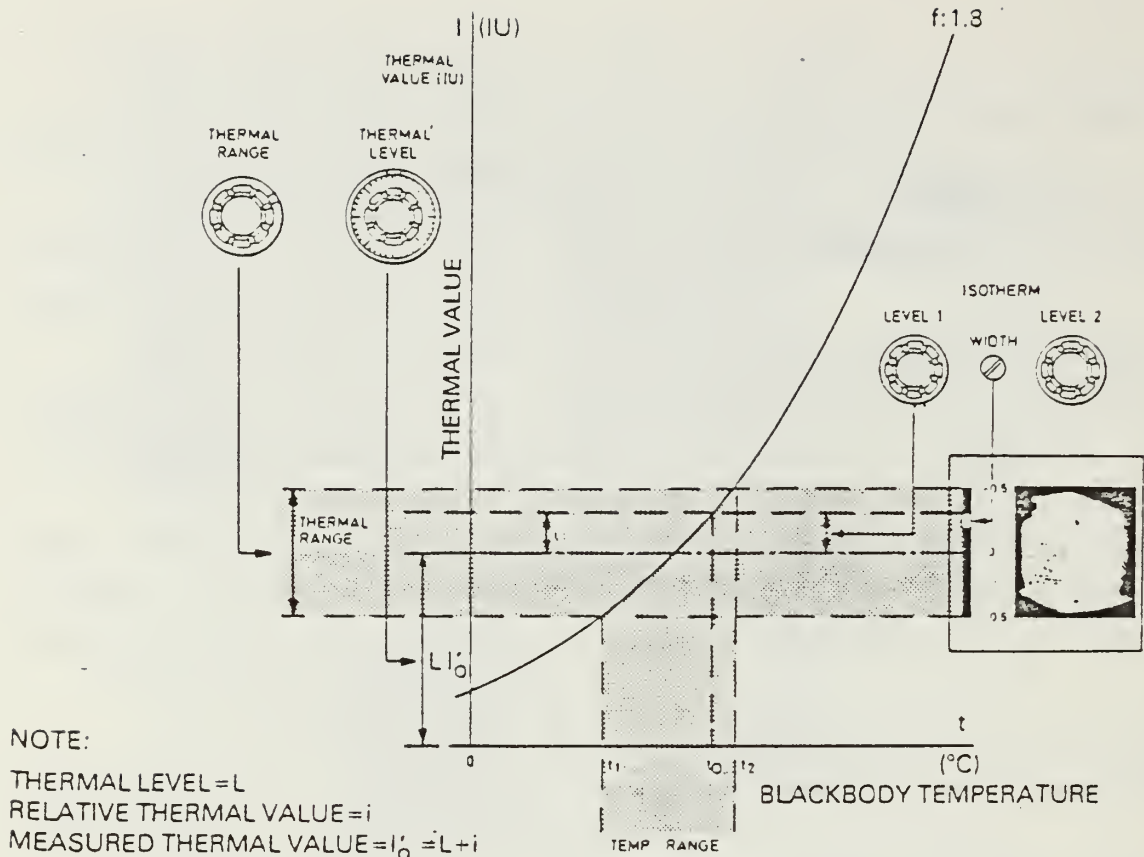


Figure 5.10 Direct measurement method.

measured thermal value I'_0 for the particular point of interest. Under the assumed simplified conditions, having $\tau_a = 1$ and $\epsilon = 1$, the calibration curve can be used, as in Fig 5.10, to translate the measured thermal value I'_0 to temperature.

Using the microcomputer as was done to collect data for this work there was no need to go through the isotherm procedure. The computer does not use isotherms but discrete thermal values. Therefore, we had the isotherm marker at zero. The subprogram F1 *Record Image* was used to record not only the thermal image picture but also the corresponding thermal value and thermal range. These values were used by the subprogram F2 *Evaluate Image* to evaluate and present on the display the temperature distribution of the recorded image in color scaling, using the standard eight color combination table of the system.

D. COMPLEX THERMAL MEASUREMENTS

1. Introduction

As mentioned before, the AGA Thermovision 780 system considers an ideal situation for the values it measures. But as we know there are several factors that influence these measurements. So the true object measurement must be derived by a calculation in which we must take into account all the factors that influence the received thermal radiation.

2. Variables Affecting the Measurement

The most important factors that affect the measured thermal radiation are the following:

- a. Emissivity of the target
- b. Background surrounding the target
- c. Target opacity
- d. Target size
- e. Atmospheric effects

Most of the objects in our environment are not blackbodies and hence their emissivities are less than one. For our case the emissivity of the R/V "POINT SUR" was found to be about 0.95 as will be explained later. The influence of the background was discussed in detail in Chapters II and III and the atmospheric effects were discussed in Chapter IV.

The target opacity has to be taken into account because some targets are more or less transparent to infrared radiation (glass, plastics, clouds, etc.). Radiation received from objects like these includes radiation transmitted from the background. Also the emissivity of the target is affected and is hard to estimate. For our case the target was considered as an opaque Lambertian surface.

The size of the target is another factor to be taken into account. Since the detector subtends a specific solid angle, if the target is not big enough to cover this angle the detector receives radiation from the target background. This will tend to affect the temperature difference indicated between the object and the background. In our case the target was not big enough to cover the field of view of a 7°X7° lens at a distance 650 m. For most measurements it occupied 1/3 to 2/5 of the display screen.

3. Exact Measurement Formula Derivation

The thermal radiation that reaches the detector of our system is the sum of the target-emitted thermal radiation, the radiation reflected by the target and the radiation emitted from the atmosphere as shown in Fig 5.11.

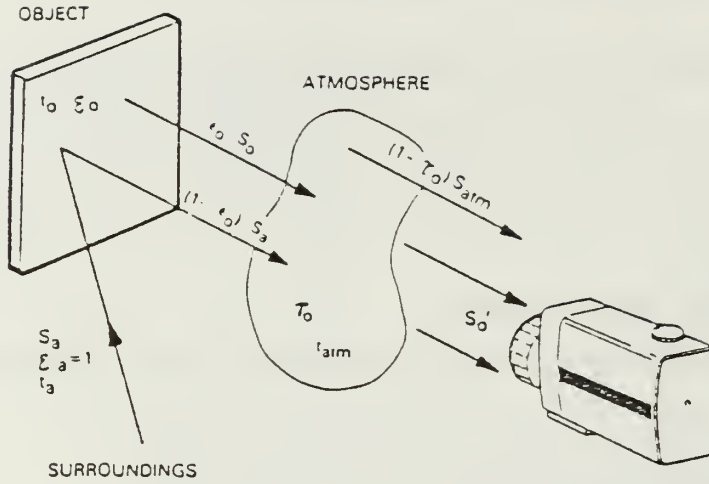


Figure 5.11 Radiation conditions in complex measurement.

If we assume an opaque object at temperature (T_o) and emissivity (ϵ_o), this object emits photon flux $\epsilon_o S_o$. S_o is the photon flux of a blackbody at the same (T_o) temperature. Since the above flux is attenuated by atmospheric transmittance (τ_a) the object radiation reaching our detector is $\epsilon_o \tau_a S_o$.

Also assuming that all surrounding surfaces are of the same ambient temperature (T_a) which determines that the emissivity is close to one ($\epsilon_a = 1$) we can say that the radiation reflected by the object is $\rho_o S_a$. S_a is the photon flux of the surroundings emitting as a blackbody ($\epsilon_a = 1$) at temperature (T_a) and ρ_o is the reflectance of the object. From the first assumption that the object is opaque we get $\rho_o = 1 - \epsilon_o$ and since the above radiation is attenuated by the atmosphere the reflected radiation reaching our detector is $\tau_a (1 - \epsilon_o) S_a$.

Finally the atmospheric radiation is given by $(1 - \tau_a) S_{atm}$ where S_{atm} is the photon flux due to atmospheric emission and scattering. Hence we can write that the photon flux S'_o reaching the detector is

$$S'_o = \epsilon_o \tau_a S_o + \tau_a (1 - \epsilon_o) S_a + (1 - \tau_a) S_{atm} \quad (\text{eqn 5.2}).$$

This photon flux relation can be converted into a thermal units relation since, as we mentioned before, the thermal value (IU) measured by the AGA Thermovision 780 is proportional to the photon flux reaching the detector. Therefore we can write

the relation $I = C \cdot S$ where I is the thermal value, C the proportionality constant and S the photon flux.

Substituting $S = I/C$ in Equation 5.1 we have the same equation in thermal values

$$I'_o = \tau_a \varepsilon_o I_o + \tau_a (1 - \varepsilon_o) I_a + (1 - \tau_a) I_{atm} \quad (\text{eqn 5.3}) .$$

This equation can be solved for I_o to find the exact temperature through the calibration curves or can be solved to find the emissivity ε_o if we know the exact temperature of the object and consequently I_o from the calibration curves. Therefore from Equation 5.3 we have

$$I_o = \frac{I'_o}{\tau_o \varepsilon_o} - \left(\frac{1}{\varepsilon_o} - 1 \right) I_a - \frac{1}{\varepsilon_o} \left(\frac{1}{\tau_a} - 1 \right) I_{atm} , \quad (\text{eqn 5.4}) \quad \text{or}$$

$$\varepsilon_o = \frac{I'_o - \tau_a I_a - (1 - \tau_a) I_{atm}}{\tau_a (I_o - I_a)} \quad (\text{eqn 5.6}) .$$

For our case the computer program calculated for us the exact temperature using Equation 5.3 after we had inserted certain values for the parameters emissivity, atmospheric transmittance, ambient temperature and temperature of the atmosphere.

VI. EMPIRICAL CALIBRATION OF AGA THERMOVISION 780

A. CALIBRATION PROBLEM

Trying to process the thermal images we had already recorded, we realized that the temperatures the computer was calculating were much higher than expected for the particular scene.

It was obvious that the Thermovision 780 was measuring thermal values ($1U$) higher than the values the calibration curves were giving for certain target temperatures.

To solve the problem we had to derive new calibration curves to use, for the exact temperature evaluation of the stored thermal images. At that time we had difficulty deriving new calibration constants to be inserted in the computer program. Therefore, we tried to find a relation between the exact temperature of a blackbody and the temperature the computer program was calculating using the faulty calibration curves for the blackbody thermal values measurements. In this way we had an empirical relation as a curve function, accurate enough to correct the temperatures the computer program was calculating using the faulty calibration curve on processing the thermal images we had stored.

B. THE CALIBRATION PROCESS

1. General

For the calibration procedure we required a blackbody working at about the temperatures we had when the images were recorded. The air temperature at that period was $9.7 - 11.3^{\circ}\text{C}$, the sea surface temperature was $11.2 - 12.8^{\circ}\text{C}$ and the laboratory ambient temperature, where the calibration procedure was carried out, was always $18 - 19^{\circ}\text{C}$. Therefore we needed to have a blackbody source to work below the ambient laboratory temperature in order to get the calibration relation we wanted.

2. Blackbody Source

For the purpose of this work we built our own blackbody source to use in our calibration procedure. As we have already mentioned we wanted this source to work at about the expected target temperatures, which were below the laboratory ambient temperature.

The core of this blackbody source was a cylinder 28 cm long and 7.5 cm wide made of thick (0.5 cm) aluminum. One end of this cylinder was cut at an angle about 60° from horizontal and it was covered with a plate of the same thickness of aluminum for minimizing reflected radiation escaping out of the cavity. The other end was cut at 90° and it was covered with a same thickness aluminum plate which had a hole of 2 cm diameter. The interior was painted with mat high emissivity black paint. Using a nichrome wire wound uniformly around the cylinder we could heat our source and by pouring liquid nitrogen inside the cylinder we could cool it below ambient temperature. The whole source was covered with a kind of fiber glass insulating material and four thermocouples were used to check the temperature stability of the core cylinder and the edge plates. In Fig 6.1 a schematic representation of this blackbody source is shown.

This source was well tested showing very good blackbody behavior, stabilizing and maintaining the temperature we needed quite fast.

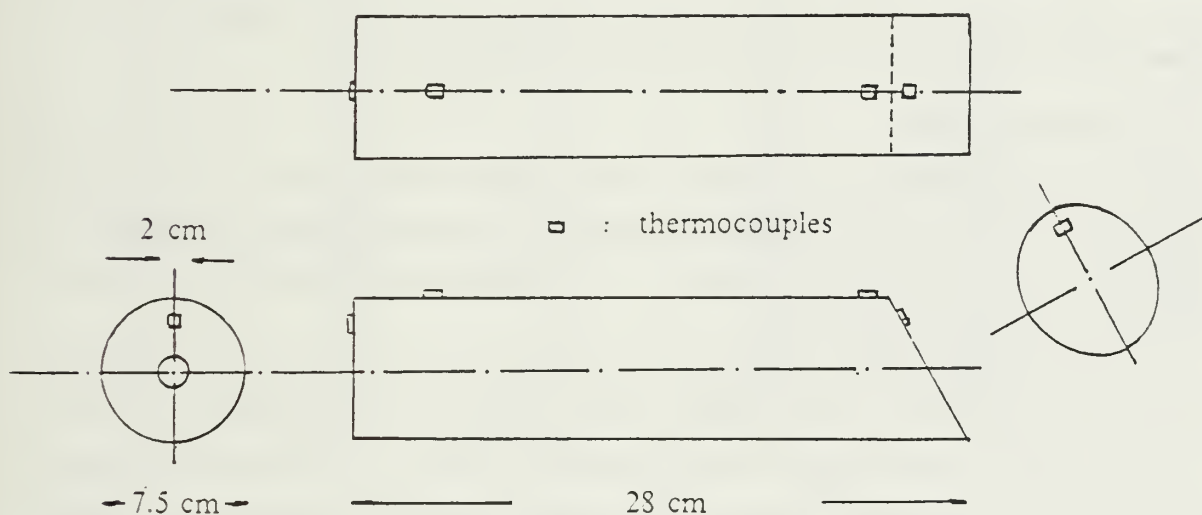


Figure 6.1 Blackbody source used for calibration procedure.

3. Calibration

We wished to find a relation between the exact temperature of an object and the temperature calculated by the computer program using the wrong calibration curves for the isothermal values measured by the Thermovision 780.

For this reason our blackbody was set to certain temperatures about the expected target temperature at the time of the experiment. After these temperatures were stabilized a measurement with the Thermovision 780 was taken from a distance of about 2 m. The thermal value was transferred to the computer and the thermal image was recorded, to be processed for temperature evaluation. For the distance of 2 m the atmospheric attenuation was neglected ($\tau_a = 1$). The above procedure was repeated for all three thermal ranges (2, 5, 10) used to collect data.

The above calibration temperature measurements for the three different thermal ranges are shown in the following Tables 3.4.5. Looking at these measurements we can notice that there is a linear relation between the blackbody exact temperature and the temperature the computer was calculating. Using the method of a least squares linear regression we found the equation of the best fitting straight line. This line was the calibration curve function we wanted to correct the temperatures of the stored thermal images.

Plotted calibration data measurements and the best fitting straight line for all three thermal ranges are shown in the following Figures 6.2 to 6.4.

C. CONCLUSIONS

From the calibration curves given in the previous chapter we can see that the portion of the curves in the temperature region used for the calibration procedure is a straight line. The linearity of that region was the confirmation that the linear relation we were getting was reasonable.

The corrections we were getting from these straight lines were accurate to within an error of about 5%. The thermal values measured by the thermovision were accurate to within half a thermal unit. This caused an error of 1.5 % in the calculated temperatures. The variance of the best fitting straight line for each thermal range caused a 3 % error in the thermal range 2, 3.5 % in the thermal range 5 and 3.7 % in the thermal range 10. Therefore, the total correction error was within 4.5 % in the thermal range 2, 5 % in the thermal range 5 and 5.2 % in the thermal range 10. Of course we have to keep in mind that these calibration functions are only valid for the temperature region about our target temperatures (9 to 18°C).

TABLE 3
THERMAL RANGE 2
CALIBRATION TEMPERATURE MEASUREMENTS

TEMPERATURES IN DEGREES C			TEMPERATURES IN DEGREES C		
BLACKBODY EXACT	AGA COMPUTED	DIFFERENCE	BLACKBODY EXACT	AGA COMPUTED	DIFFERENCE
3.0	16.1	13.1	15.5	26.9	11.4
4.2	16.5	12.3	16.0	27.3	11.3
5.0	17.2	12.2	16.5	27.6	11.1
5.6	17.8	12.2	17.0	28.0	11.0
6.3	18.2	11.9	17.5	28.3	10.8
7.0	18.7	11.7	18.0	28.9	10.9
8.0	19.7	11.7	18.5	29.4	10.9
8.5	20.1	11.6	19.0	29.8	10.8
9.0	20.5	11.3	19.5	30.2	10.7
9.5	21.2	11.6	20.0	30.7	10.7
10.0	21.8	11.8	20.5	31.1	10.6
11.0	22.5	11.5	21.0	31.6	10.6
12.0	23.4	11.5	21.5	32.0	10.5
12.5	23.8	11.3	22.0	32.4	10.4
13.0	24.5	11.5	22.5	33.0	10.5
13.5	25.1	11.6	23.0	33.6	10.6
14.0	25.7	11.7	23.5	33.9	10.4
14.5	26.1	11.6			

MEAN DIFFERENCE : 11.03

STANDARD DEVIATION : 1.724

VARIANCE : 2.887

BEST FIT STRAIGHT LINE : $Y = (1.0238) X - 11.62$

AGA CALIBRATION CURVE

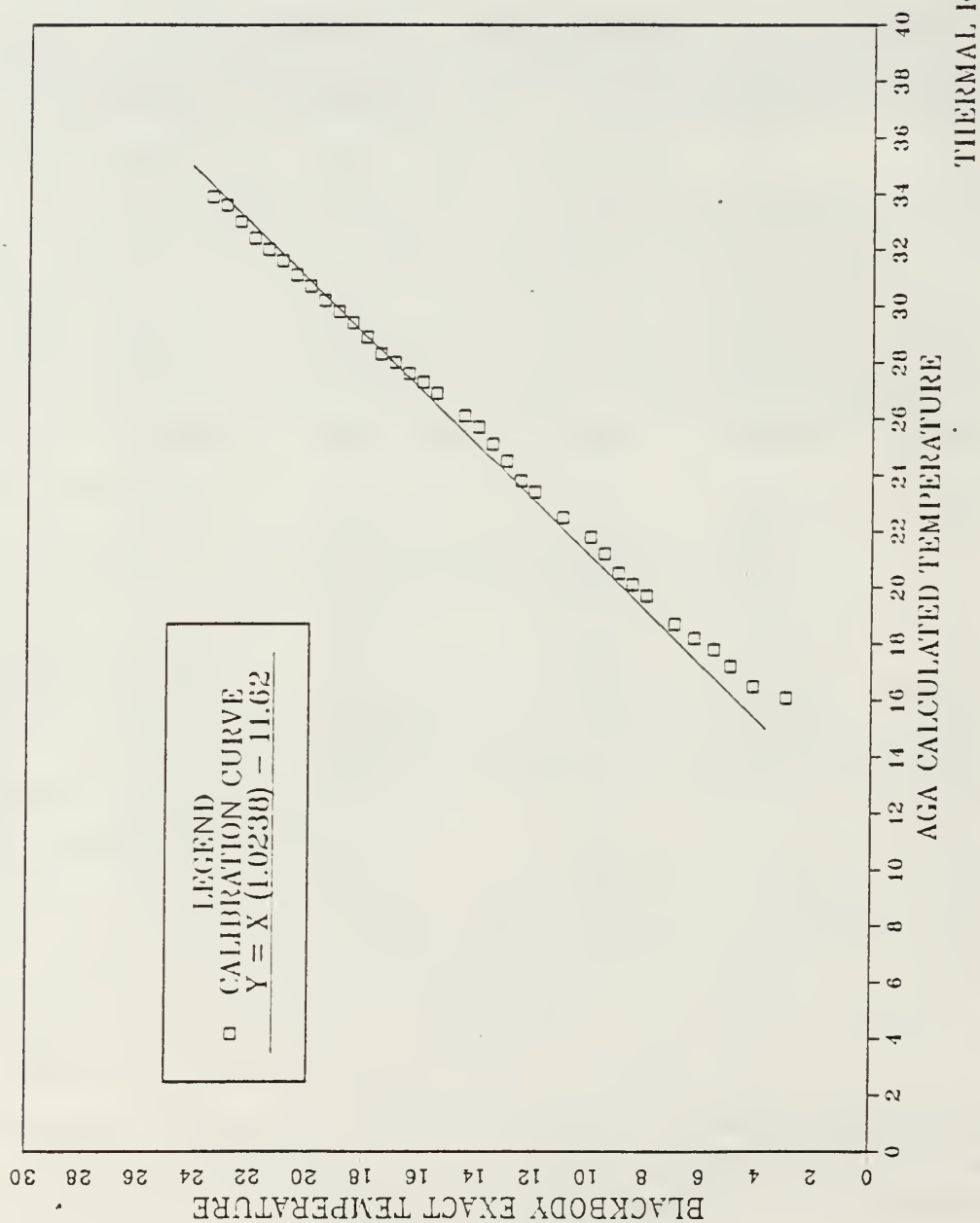


Figure 6.2 Thermal Range 2 calibration temperature measurements.

TABLE 4
THERMAL RANGE 5
CALIBRATION TEMPERATURE MEASUREMENTS

TEMPERATURES IN DEGREES C			TEMPERATURES IN DEGREES C		
BLACKBODY EXACT	AGA COMPUTED	DIFFERENCE	BLACKBODY EXACT	AGA COMPUTED	DIFFERENCE
0.0	14.1	14.1	16.0	26.7	10.7
1.0	15.1	14.1	17.0	27.6	10.6
2.0	15.8	13.8	18.0	28.2	10.2
3.0	16.8	13.8	19.0	29.6	10.6
4.0	17.6	13.6	20.0	30.5	10.5
5.0	18.2	13.2	21.0	31.0	10.0
6.0	18.9	12.9	22.0	32.3	10.3
7.0	19.2	12.2	23.0	32.6	9.6
8.0	20.4	12.4	24.0	34.2	10.2
9.0	21.7	12.7	25.0	34.8	9.8
10.0	22.3	12.3	26.0	36.5	10.5
11.0	23.0	12.0	27.0	36.9	9.9
12.0	24.2	12.2	28.0	37.6	9.6
13.0	25.0	12.0	29.0	38.5	9.5
14.0	25.7	11.7			

MEAN DIFFERENCE : 11.55

STANDARD DEVIATION : 1.531

VARIANCE : 2.265

BEST FIT STRAIGHT LINE : $Y = (1.1956) X - 16.646$

AGA CALIBRATION CURVE

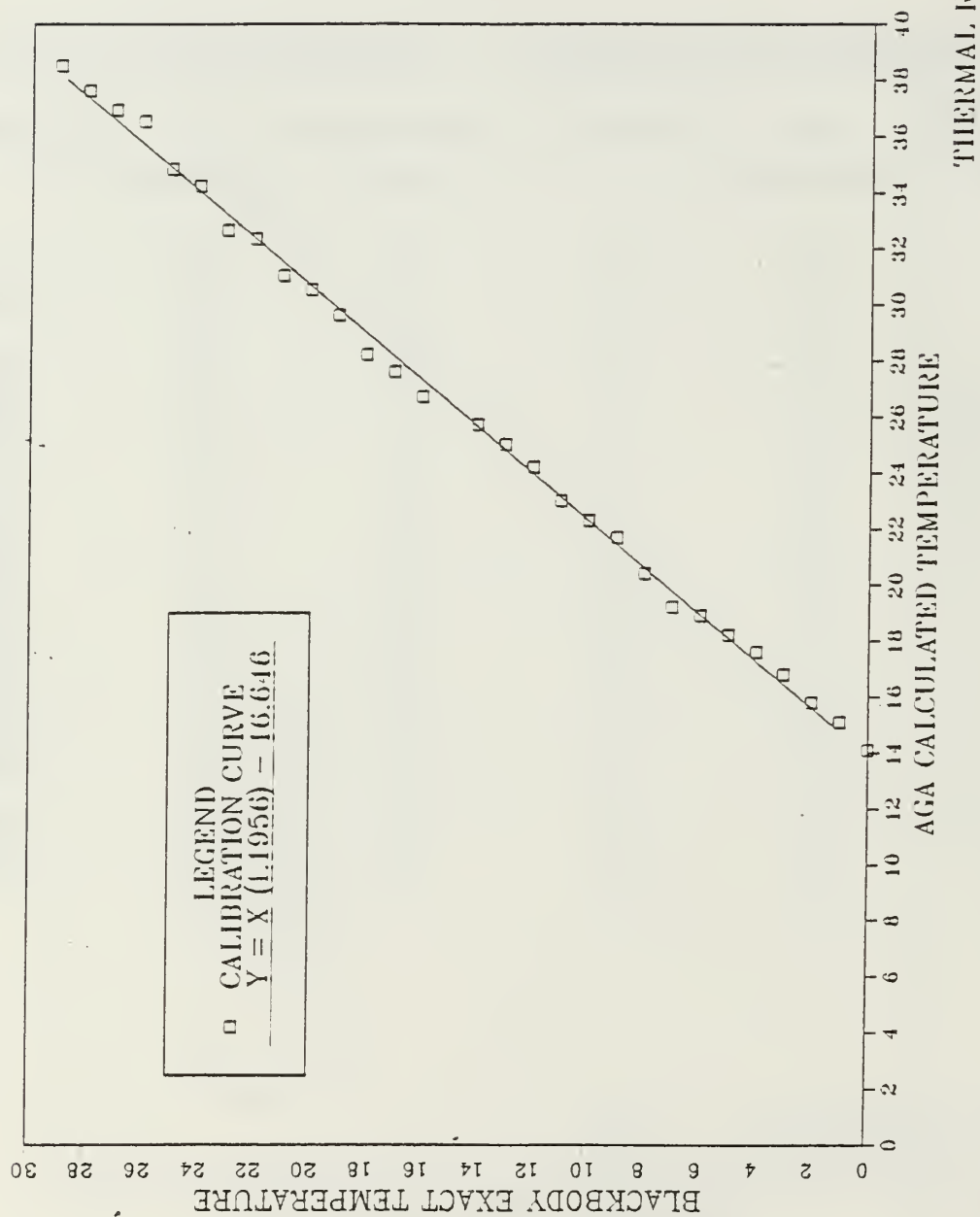


Figure 6.3 Thermal Range 5 calibration temperature measurements.

TABLE 5
THERMAL RANGE 10
CALIBRATION TEMPERATURE MEASUREMENTS

TEMPERATURES IN DEGREES C			TEMPERATURES IN DEGREES C		
BLACKBODY EXACT	AGA COMPUTED	DIFFERENCE	BLACKBODY EXACT	AGA COMPUTED	DIFFERENCE
0.5	14.2	13.7	16.5	27.2	10.7
1.5	15.0	13.5	17.5	27.5	10.0
2.5	15.6	13.1	19.5	29.5	10.0
3.5	16.8	13.3	20.5	30.6	10.1
4.5	17.7	13.2	21.5	31.2	9.7
5.5	17.9	12.4	22.5	32.4	9.9
6.5	18.6	12.1	23.5	32.8	9.3
7.5	19.4	11.9	24.5	34.3	9.8
8.5	20.1	11.6	25.5	35.0	9.5
9.5	20.6	11.1	26.5	35.6	9.1
10.5	21.0	10.5	27.5	36.9	9.4
11.5	22.9	11.4	28.5	37.5	9.0
12.5	24.1	11.6	29.5	38.6	9.1
13.5	25.2	11.7			
14.5	25.8	11.3			

MEAN DIFFERENCE : 11.00

STANDARD DEVIATION : 1.489

VARIANCE : 2.141

BEST FIT STRAIGHT LINE : $Y = (1.1807) X - 15.656$

AGA CALIBRATION CURVES

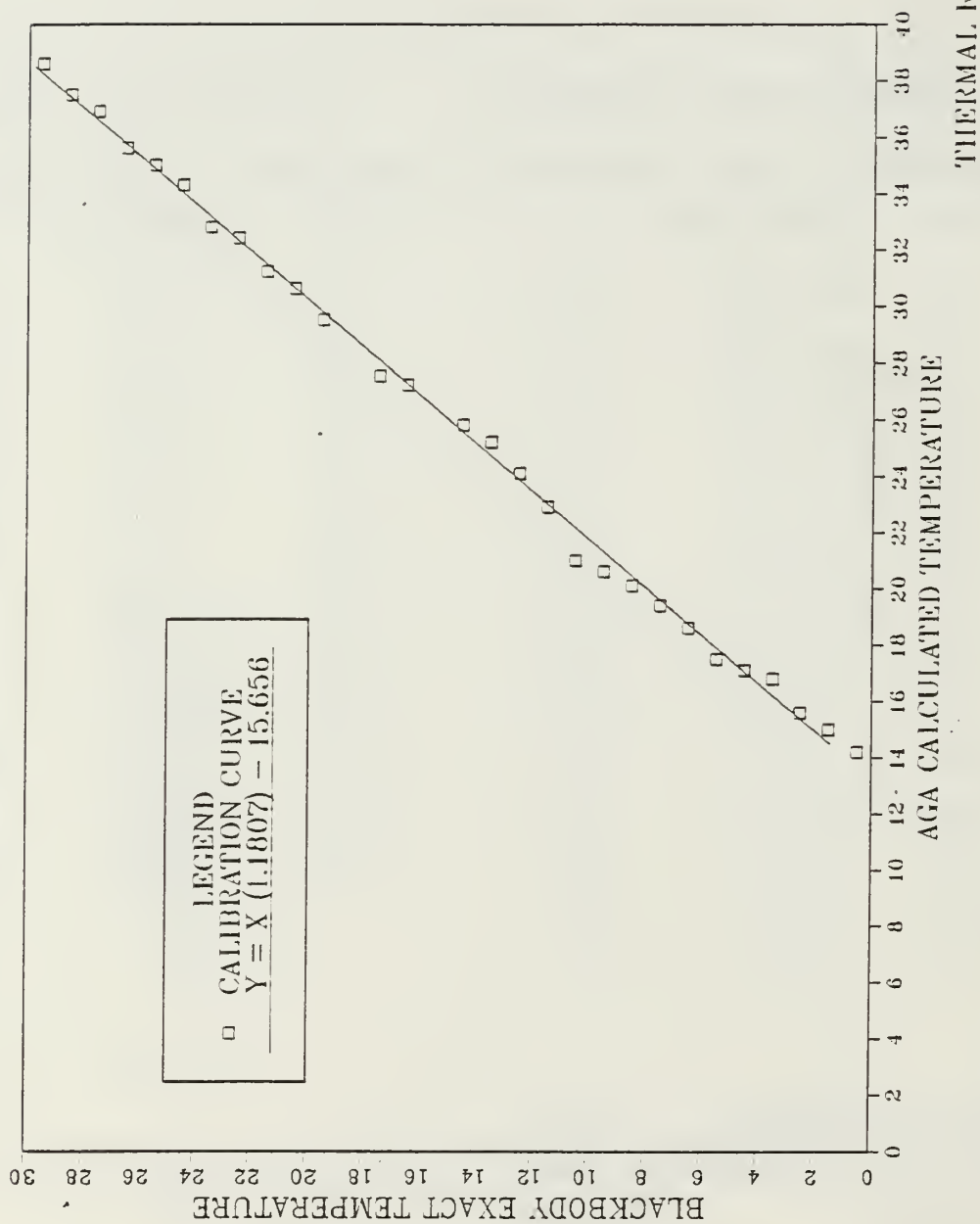


Figure 6.4 Thermal Range 10 calibration temperature measurements.

VII. SIGNATURE MEASUREMENTS

A. GENERAL

All signature measurements were taken during mid May 1986, on the following dates and time periods.

1. May 14 09:00 - 09:25
2. May 18 11:57 - 13:07
3. May 21 00:05 - 00:13
4. May 21 17:18 - 17:37
5. May 22 00:48 - 01:03

Thermal imaging data were collected for the spectral range 8 - 14 μm using the LW detector of the AGA Thermovision 780. The thermovision system and its supporting computer were set up in a laboratory building at the eastern side of the HOPKINS MARINE STATION grounds, at a window facing directly over the shore line toward the closest buoy. The laboratory is about 8 - 10 meters above sea level.

The target was the oceanographic ship R/V POINT SUR which was on an operational oceanography student cruise. During those periods in which it was made available for signature measurements the ship maneuvered in the vicinity of the off shore (635 meters) buoy, displaying various aspects as requested. The distance between the the ship and our detector was about 650 m. At that distance, the closest the ship could reach, using a 7°X7° FOV lens we had an image covering almost 2/3 of the screen. Six thermocouples installed about the superstructure were used to have a calibration of the actual ship temperature. The thermocouples were sampled at 10-seconds intervals and the output voltages were recorded, to be later converted into temperatures.

The environmental conditions for the time period in which the measurements were taken are shown in the data presentation tables. Generally for these periods the area was under the influence of a high pressure system, with North West winds and coastal fog, especially during the morning hours.

Thermal images for different ship aspects, were recorded and stored during time periods in which the ship was available for us and the environmental conditions allowed. All data were recorded assuming the ideal conditions appropriate to the

Thermovision system measurements, that the target was a blackbody source and atmospheric attenuation was neglected.

Fig 7.1 is a map of the Monterey Peninsula showing the area where the signature measurements were taken.

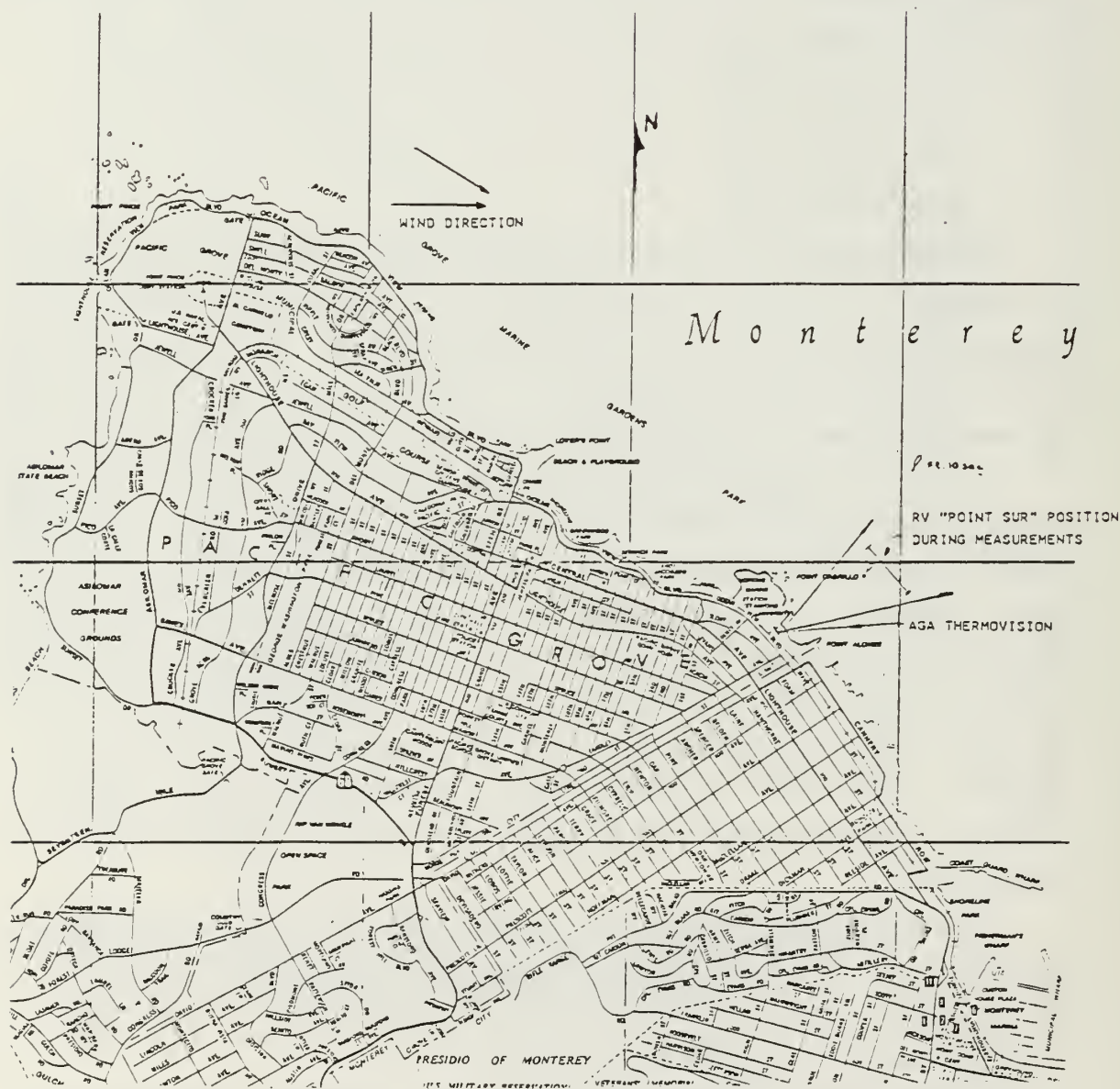


Figure 7.1 Area where the signature measurements were taken.

B. PARAMETERS FOR TEMPERATURE EVALUATION

As mentioned in Chapter five the processing of the recorded and stored thermal images was done using the DISCO 3.0 computer program. For temperature evaluation the program asks for certain parameters to be provided. These parameters, as we have discussed before in the derivation of the exact measurement formula, in Chapter five, are the atmospheric (air) temperature, the ambient temperature, the atmospheric transmittance and the target emissivity.

1. Atmospheric Transmittance

The atmospheric transmittance was calculated using the LOWTRAN 6 code. For our experimental conditions, temperatures about 10 to 15°C, we selected the midlatitude winter (45°, January) atmospheric model for a horizontal path. The Navy Maritime was selected for the boundary layer aerosol model, discussed in detail in chapter four. For the geometrical path we inserted target altitude 10 m and horizontal path length 650 m. The spectral range was set at 8 - 14 μm (710 - 1250 cm^{-1}) with frequency increment 5 cm^{-1} .

The meteorological data needed, mainly wind speed and wind direction, for determining the air mass character, continental influence, were taken from 10-minute logged meteorological data recorded from instruments stationed on the ship. Such data weren't recorded for the last two observation periods on May 21 (17:18 - 17:37) and May 22 (00:48 - 01:03). For these periods meteorological conditions were approximated using observations taken from the meteorological station at POINT PINOS, the closest station in the area of the experiment (see Fig 7.1). Since the direction of the wind was from North West the continental influence as we can see from the map in Fig 7.1 was not very strong. So on a scale from 0 (open ocean) to 10 (maximum continental influence) we inserted mass character scale from 2 to 3 .

In Table 6 are shown the meteorological data used, the air mass character scale (ICSTL) and the calculated atmospheric transmittance for each observation period.

2. Emissivity

The emissivity of the ship surface was found by evaluating the emissivity of two metallic pieces taken from different parts on the ship. These specimens were painted with slightly different white paint, representing the paint coatings of the ship surface. These had also been exposed under the same environmental conditions for the same time period as the whole ship surface.

TABLE 6
INSERTED METEOROLOGICAL DATA AND ATMOSPHERIC
TRANSMITTANCE

DATE	WIND SPEED	WIND DIR.	ICSTL	ATMOSP. TRANSM.
MAY 14 (09:00-09:25)	4.80 m/s	290 - 300	3	0.8677
MAY 18 (11:57-13:07)	6.26 m/s	270 - 280	3	0.8539
MAY 21 (00:05-00:13)	5.20 m/s	270 - 300	3	0.8640
MAY 21 (17:18-17:37)	10.20 m/s	320	2	0.8178
MAY 22 (00:48-01:03)	9.25 m/s	290 - 300	3	0.8282

Assuming that the emissivity was constant over the spectral region involved, we used Equation 5.5 derived in Chapter five, for our calculations

$$\epsilon_o = \frac{I'_o - \tau_a I_a - (1 - \tau_a) I_{atm}}{\tau_a (I_o - I_a)}$$

Making some more assumptions for the laboratory environment in which we were working, this equation was simplified further. First we had to assume that the ambient temperature and the atmospheric temperature were the same in our case. This meant that the equivalent source thermal value for the surroundings (I_a) had to be the same as the atmospheric path (I_{atm}). So the above equation was then reduced to

$$\epsilon_o = \frac{I'_o - I_{atm}}{\tau_a (I_o - I_a)}$$

Second, for the distance of about 2 m between the detector and specimens being measured, we assumed no atmospheric attenuation, so $\tau_a = 1$, and the emissivity equation was reduced again to

$$\epsilon_o = \frac{I'_o - I_a}{I_o - I_a},$$

where I'_O is the Thermovision 780 measured thermal value, I_a is the calibrated thermal value for the known ambient temperature and I_O is the calibrated thermal value for the known object temperature.

With this last equation we could calculate the emissivity of the specimens, accurately enough, if we knew exactly the ambient temperature and the temperature of the specimens. The procedure was started by heating the specimens as uniformly as we could, using a blower, to a temperature giving good thermal images above the ambient temperature. This temperature was checked using a thermocouple. With the best thermal image on the screen, the temperature of the specimen, the ambient temperature and the Thermovision thermal value measurement were recorded. The ambient temperature was measured using a common thermometer.

Knowing the exact temperatures, the calibration curves with an appropriate correction, discussed in Chapter six, were used to get the thermal values (I_O) for the specimen and (I_a) for the surroundings. Therefore, we had what we wanted for our calculation.

The above procedure was repeated several times at different temperatures for each specimen. The results were averaged to the following values.

- a. 0.943 first specimen
- b. 0.958 second specimen

These values are very close to the values we found in different books for the emissivity of all kinds of paint, which was 0.95. For the calculations done in this work we considered the emissivity of the ship surface to be 0.95, taking the average of the two values we found.

3. Atmospheric Air Temperature

The atmospheric air temperature measurements were taken from logged meteorological data recorded on the ship. The air mass temperatures measured close to our station had strong continental influence, so that they were higher than the temperatures measured at the ship location and not representative for our situation.

The atmospheric air temperatures are shown for each date in the data presentation tables.

4. Ambient Temperature

These temperatures were measured using a common mercury thermometer near the open window, where our scanner was operating. Their value was between the higher room temperature and the lower outside temperature.

The ambient temperature for each date is shown in the data presentation tables.

C. TEMPERATURE DATA EVALUATION AND PRESENTATION

Inserting the correct parameters, the computer subprogram *Evaluate image* was used to evaluate the temperature distribution of the ship, for each thermal picture recalled from storage. This temperature distribution was presented on the computer screen with the standard 8 color scaling combination.

For better presentation of these temperatures we divided the ship image for each aspect in small squares and we tried to assign an average temperature to each square. A cartesian system was used to present these temperatures for the starboard side, the port side and the stern. These temperatures were averaged for each aspect, for each date, in order to have the final temperature distribution for the particular aspect at the time period our data were averaged.

The problem was that the aspect shown by the ship was not always the same, because she was drifting and had to keep in station using the engines. So pictures, say of the starboard side, taken under several time periods had different aspect angles with the line of sight. This caused reflection problems, with thermal radiation from hot surfaces such as the stack reflecting from cooler surfaces. Therefore, our scanner measured not only the emitted thermal radiation but both the reflected and the emitted thermal radiation from that surface. So the temperature measurement we were evaluating was higher than the correct temperature corresponding to that surface. To minimize this problem we tried to average the temperatures only from those pictures showing the most perpendicular aspect to the line of sight.

However the temperatures obtained were not correct, as discussed in detail in Chapter six, since the computer-calculated temperatures had still to be corrected using the empirical relation already derived. Hence the average temperature for each square had to be corrected using the best fit straight line equation corresponding to the thermal range in which the data were collected.

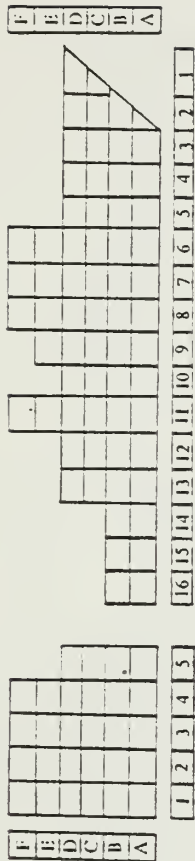
The corrected average temperature distribution for the starboard side, the port side and the stern, available for each date, are given in the following Tables 7 to 11.

TABLE 7

R/V "POINT SUR" TEMPERATURE MEASUREMENTS "A"

DATE / TIME : 14 MAY 09:00 - 09:25
 WIND SPEED / DIRECTION : 4.8 m/sec 290° - 300°
 AIR TEMPERATURE : 10.5°C
 AMBIENT TEMPERATURE : 15°C
 SEA SURFACE TEMPERATURE : 12.6°C
 OVERCAST, HAZY, VISIBILITY 4 NM
 ATMOSPHERIC TRANSMITTANCE : 0.8679

TEMPERATURES IN °C



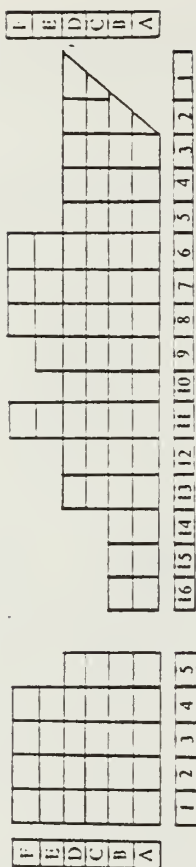
STARBOARD SIDE						
	A	B	C	D	E	F
1			11.97	11.75		
2	12.26	12.56	12.43	12.12		
3	12.75	13.08	12.53	12.35		
4	12.57	13.43	12.65	12.77		
5	12.97	13.30	12.91	12.75		
6	13.04	14.22	12.92	12.73	12.20	11.84
7	13.50	14.63	13.10	12.73	12.46	12.18
8	13.64	13.96	13.90	12.71	12.66	12.28
9	13.80	14.08	14.36	13.47	13.06	
10	14.00	15.63	15.46	13.67		
11	14.21	16.16	15.58	16.05	16.16	14.55
12	13.74	15.81	14.51	13.33		
13	13.46	14.69	14.51	13.04		
14	13.53	13.12				
15	13.39	13.16				
16	13.38	12.88				

PORT SIDE						
	A	B	C	D	E	F
1			11.98	12.22		
2	11.61	12.48	12.43	12.55		
3	12.22	12.68	12.75	12.50		
4	12.31	12.58	12.54	12.35		
5	12.50	12.86	12.58	12.75		
6	12.57	13.50	12.64	12.40	11.93	11.85
7	12.85	14.02	13.18	13.78	12.26	12.29
8	13.10	14.29	13.11	12.68	12.88	12.45
9	13.21	14.27	12.90	12.50	12.69	
10	13.76	14.40	13.68	13.03		
11	14.06	15.20	16.03	16.27	16.27	14.32
12	13.52	15.00	14.78	13.46		
13	13.40	14.95	14.41	12.84		
14	12.94	13.46				
15	12.55	13.20				
16	12.47	13.20				

STERN						
	A	B	C	D	E	F
1	13.64	14.61	14.35	16.00	16.02	15.13
2	13.64	14.45	13.53	14.25	14.88	14.56
3	13.84	14.56	14.05	14.05	14.25	
4	13.74	14.45	14.15	13.74	14.25	
5	13.64	14.10				

TABLE 8
R/V "POINT SUR" TEMPERATURE MEASUREMENTS "B"

DATE / TIME : 18 MAY 11:57 - 13:07
WIND SPEED / DIRECTION : 6.26 m/sec 270°- 280°
AIR TEMPERATURE : 9.7°C
AMBIENT TEMPERATURE : 17°C
SEA SURFACE TEMPERATURE : 13.1°C
OVERCAST, HAZY, VISIBILITY 3 NM
ATMOSPHERIC TRANSMITTANCE : 0.8539



STARBOARD						
	A	B	C	D	E	F
1			12.44	12.03		
2	11.82	12.33	12.13	12.44		
3	12.13	12.95	12.23	12.48		
4	12.33	13.05	12.33	12.54		
5	12.44	13.46	12.74	12.54		
6	12.54	13.87	12.84	12.44	11.31	11.62
7	12.23	12.97	12.74	12.33	11.31	11.82
8	12.33	13.97	12.95	12.23	11.62	12.03
9	12.64	13.97	13.05	12.03	11.82	
10	12.85	13.97	12.64	11.92		
11	13.15	14.18	14.18	14.18	14.18	13.46
12	13.15	13.77	13.05	13.36		
13	13.05	13.66	12.84	12.84		
14	12.95	13.56				
15	12.74	12.84				
16	11.82	12.33				

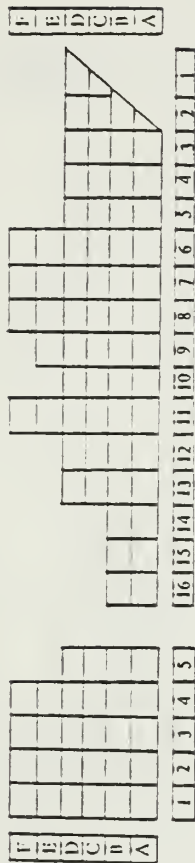
PORT						
	A	B	C	D	E	F
1			12.44	12.13		
2	11.92	12.54	12.44	12.44		
3	12.13	13.15	12.44	12.64		
4	12.33	13.26	12.54	12.84		
5	12.44	13.66	12.95	12.95		
6	12.64	13.66	12.95	13.05	11.92	11.82
7	12.74	14.07	13.15	13.05	12.44	11.93
8	12.95	14.28	13.15	12.46	12.74	12.34
9	13.15	14.28	12.46	12.54	12.64	
10	13.15	14.28	13.66	12.54		
11	13.87	14.28	14.28	14.28	14.28	13.46
12	13.66	14.28	14.28	13.46		
13	13.46	14.07	13.15	12.85		
14	13.05	13.56				
15	12.74	13.15				
16	12.03	12.85				

STERN						
	A	B	C	D	E	F
1	12.13	12.85	12.85	13.97	14.28	13.77
2	12.13	12.85	12.74	13.56	14.07	13.05
3	12.13	12.85	12.74	12.54	12.85	12.34
4	12.13	12.64	12.85	12.34	12.34	
5	12.13	12.54	12.64	12.34		

TABLE 9

R/V "POINT SUR" TEMPERATURE MEASUREMENTS "C"

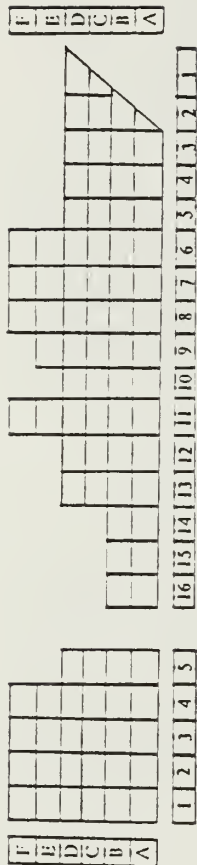
DATE / TIME : 21 MAY 00:05 - 00:13
 WIND SPEED / DIRECTION : 5.2 m/sec 270-- 300•
 AIR TEMPERATURE : 11.3°C
 AMBIENT TEMPERATURE : 17°C
 SEA SURFACE TEMPERATURE : 11.9°C
 CLEAR, VISIBILITY 9 NM
 ATMOSPHERIC TRANSMITTANCE : 0.8640



STARBOARD							PORT							STERN						
	A	B	C	D	E	F		A	B	C	D	E	F		A	B	C	D	E	F
1			11.14	11.19			1							1						
2	11.54	12.21	12.28	11.79			2							2						
3	11.88	12.46	12.40	11.84			3							3						
4	12.00	12.39	12.45	11.94			4							4						
5	12.00	12.39	12.39	11.94			5							5						
6	11.89	12.28	12.07	11.84	11.34	11.34	6													
7	11.89	12.18	12.12	12.12	11.62	11.69	7													
8	11.94	12.12	12.12	12.76	12.55	12.25	8													
9	11.94	12.17	12.32	12.79	12.67		9													
10	11.94	12.22	13.11	12.54			10													
11	13.07	13.57	14.30	14.60	14.60	14.07	11													
12	13.16	13.57	13.97	12.59			12													
13	12.98	13.23	13.10	12.23			13													
14	12.92	12.56					14													
15	12.45	12.22					15													
16	11.77	12.06					16													

TABLE 10
R/V "POINT SUR" TEMPERATURE MEASUREMENTS "D"

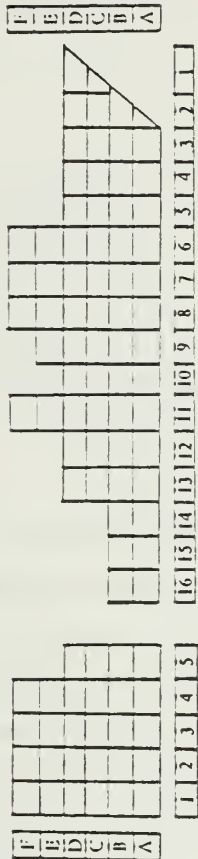
DATE / TIME : 21 MAY 17:18 - 17:37
WIND SPEED / DIRECTION : 10.2 m/sec 320°
AIR TEMPERATURE : 12.2°C
AMBIENT TEMPERATURE : 19°C
SEA SURFACE TEMPERATURE : 13.2°C
SUN, CLEAR, VISIBILITY 10 NM
ATMOSPHERIC TRANSMITTANCE : 0.8178



STARBOARD SIDE							PORT SIDE						
	A	B	C	D	E	F		A	B	C	D	E	F
1			13.17	13.28			1			12.54	12.89		
2	13.22	13.58	13.43	13.28			2	12.06	12.77	13.37	13.13		
3	13.22	13.58	13.48	13.43			3	12.30	13.25	13.85	13.37		
4	13.22	13.48	13.48	13.48			4	13.13	13.73	14.21	13.49		
5	13.28	13.48	13.38	14.40			5	13.25	14.09	14.45	13.49		
6	13.58	13.89	14.09	14.71	13.99	13.38	6	13.37	14.45	14.21	13.97	13.37	13.01
7	13.78	14.13	14.40	14.71	14.13	13.48	7	13.37	14.33	14.45	14.09	13.99	13.25
8	13.78	13.99	14.50	14.50	13.99	13.48	8	13.53	14.69	14.45	14.21	13.85	13.37
9	13.99	14.13	14.13	14.50	14.24		9	13.73	14.92	14.57	14.21	14.02	
10	13.99	14.13	14.40	14.50			10	14.09	14.05	15.17	14.21		
11	13.99	15.01	15.63	15.63	15.63	15.12	11	15.05	17.20	18.15	18.15	18.15	16.96
12	13.99	14.91	14.60	14.30			12	14.68	16.48	15.28	14.45		
13	13.68	14.50	14.50	14.30			13	13.73	15.28	14.45	13.97		
14	13.58	14.30					14	13.37	13.85				
15	13.58	14.09					15	12.89	13.37				
16	13.58	13.99					16	12.65	13.12				

TABLE II
R/V "POINT SUR" TEMPERATURE MEASUREMENTS "E"

DATE / TIME : 22 MAY 00:48 - 01:03
WIND SPEED / DIRECTION : 9.5 m/sec 290°
AIR TEMPERATURE : 9.7°C
AMBIENT TEMPERATURE : 17°C
SEA SURFACE TEMPERATURE : 10.8°C
CLEAR, VISIBILITY 10 NM
ATMOSPHERIC TRANSMITTANCE : 0.8232



STARBOARD SIDE							PORT SIDE							STERN							
	A	B	C	D	E	F		A	B	C	D	E	F		A	B	C	D	E	F	
1			9.67	9.32			1			9.47	9.31				1	9.57	9.98	10.10	11.82	11.82	11.72
2	9.67	10.59	9.88	9.37			2	9.47	10.39	9.78	9.42				2	9.57	9.67	10.29	10.39	10.18	9.98
3	9.72	10.44	9.82	9.57			3	9.47	10.19	9.78	9.42				3	9.57	9.67	10.80	10.60	9.83	9.67
4	9.72	10.08	9.82	9.57			4	9.47	9.88	9.57	9.37				4	9.57	9.67	10.08	10.60	9.73	9.47
5	9.62	10.08	9.62	9.47			5	9.37	9.67	9.37	9.26				5	9.57	9.57	9.67	9.88	9.67	9.47
6	9.47	9.57	9.47	9.67	9.47	9.37	6	9.37	9.67	9.26	9.26	9.47	9.98	9.67							
7	9.47	9.57	9.52	9.82	9.78	9.47	7	9.52	9.47	9.26	9.47	9.98	9.78								
8	9.47	9.37	9.62	10.29	10.08	9.67	8	9.52	9.57	9.26	9.57	10.19	9.88								
9	9.37	9.26	9.67	9.72	9.90		9	9.47	9.47	9.37	9.37	9.78									
10	9.37	9.37	9.67	9.78			10	9.57	9.78	9.67	9.67										
11	9.47	9.47	9.78	10.39	11.72	11.00	11	10.19	11.72	11.72	11.72	11.72	11.00								
12	9.67	10.19	10.29	9.78			12	9.78	11.21	10.80	10.19										
13	9.67	10.19	10.19	9.57			13	9.67	11.00	10.80	9.98										
14	9.57	9.78					14	9.57	10.19												
15	9.42	9.67					15	9.57	9.78												
16	9.42	9.67					16	9.47	9.67												

D. TEMPERATURE DATA ACCURACY

As mentioned before, six thermocouples were installed about the superstructure, at the following locations:

- T1 : On the after starboard side of the deckhouse
- T2 : On the forward starboard side of the deckhouse
- T3 : On the aft bulkhead of the bridge (away from the stack)
- T4 : On the aft bulkhead of the deckhouse
- T5 : On the port side of the deckhouse
- T6 : On the after deckhouse forward of the stack

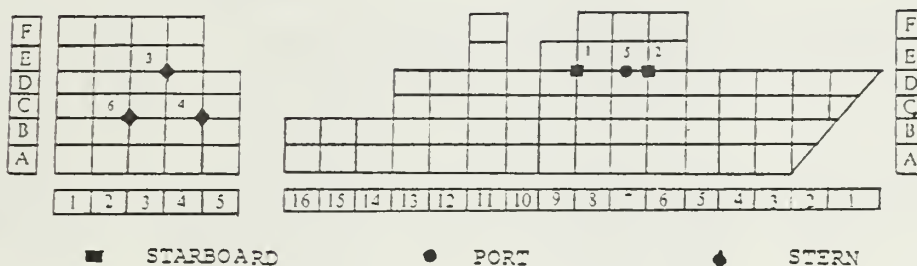
These thermocouples were sampled at 10-seconds intervals and the output voltages were recorded and later converted into temperatures. Thus, we had an indication of the actual temperature at six different locations on the ship, for the whole time period we were taking our measurements. In this way we had an absolute reference to compare our data with to estimate the accuracy of the process of calculating the temperature of the target from measurements of thermal radiation.

First we had to fit the thermocouples in the squares covering the areas where they were located. Then we had to find the mean calculated temperature corresponding to these locations. For example for a thermocouple located at the intersection of two or four squares, the calculated temperature corresponding to this thermocouple was taken as the mean temperature of the two or four squares. Finally we had to compare the above temperature with the thermocouple temperature averaged over for the same period as the calculated temperature for each square.

In the following Table 12 are shown the thermocouple locations and the comparison of the actual with the measured and calculated temperatures in degrees C for each date.

As we can see, for most of the time the temperature differences were small. The big negative differences in the stern area for the two first dates (temperature of thermocouple higher than AGA thermovision temperature), are believed to occur because the thermocouples were not yet stabilized at that period. That is, at a time when the ship was turning, hot air from the stack area was blown onto these thermocouples, making their measurements fluctuate. So for measurements at this time, just after the turn, the thermocouples did not have the time to be stabilized.

TABLE 12
THERMOCOUPLE - AGA THERMOVISION TEMPERATURE COMPARISON



		MAY 14 (09:00 - 09:25)			MAY 18 (11:57 - 13:07)			
		SENSOR	THERMOC.	AGA	DIFFER.	THERMOC.	AGA	DIFFER.
STERN PORT STARB	T1		13.34	12.98	- 0.36	11.84	11.92	+ 0.08
	T2		12.41	12.53	- 0.12	12.26	11.84	- 0.42
	T5		15.41	14.23	- 1.18	14.13	12.66	- 1.47
	T3		13.27	13.02	- 0.25	14.02	12.74	- 1.28
	T4		16.17	14.07	- 2.10	13.81	12.51	- 1.30
	T6		15.84	14.15	- 1.69	14.95	12.80	- 2.15
DATE		MAY 21(00:05 - 00:13)						
		SENSOR	THERMOC.	AGA	DIFFER.			
STARB	T1		11.06	12.69	+ 1.63			
	T2		10.81	11.73	+ 0.92			
DATE		MAY 21 (17:18 - 17:37)			MAY 22 (00:48 - 01:03)			
		SENSOR	THERMOC.	AGA	DIFFER.	THERMOC.	AGA	DIFFER.
STERN PORT STARB	T1		13.28	14.30	+ 1.02	9.52	9.99	- 0.47
	T2		13.32	14.38	- 1.06	9.24	9.68	- 0.44
	T5		13.79	14.73	+ 0.94	9.91	9.74	- 0.17
	T3		14.04	14.04	0.00	9.76	9.72	- 0.04
	T4		14.50	14.85	+ 0.35	10.06	10.21	+ 0.15
	T6		14.60	15.15	+ 0.55	9.53	10.10	+ 0.57

E. RADIANCE CALCULATION

Knowing the temperature distribution of the ship, we could calculate the radiance for the spectral region of the measurements.

Starting with the Planck blackbody radiation law we could write

$$M = \int_{\lambda_2}^{\lambda_1} W(\lambda, T) d\lambda = \int_{\lambda_2}^{\lambda_1} \left(\frac{2\pi hc^2}{\lambda^5} \right) \left(\frac{1}{e^{hc/\lambda KT} - 1} \right) d\lambda \quad \frac{W}{cm^2} .$$

If we let $C_1 = 2\pi hc^2$ and $C_2 = \frac{hc}{K}$ we could write the above equation as follows

$$M = \int_{\lambda_2}^{\lambda_1} \frac{C_1}{\lambda^5 (e^{C_2/\lambda T} - 1)} d\lambda \quad \frac{W}{cm^2} .$$

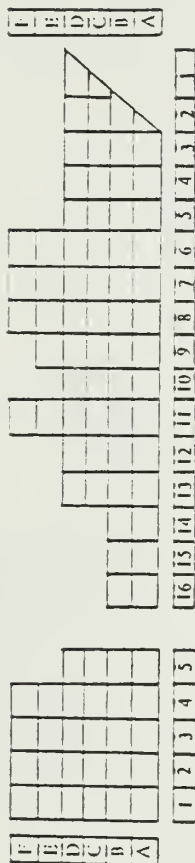
Solving this integral in the spectral region 8 - 14 μm , for the known temperatures we found the in-band radiant flux density M in W/cm^2 . With the assumption that our surface was an opaque Lambertian surface, we could divide the radiant flux by π and multiply by the emissivity (ϵ) to obtain the required spectral radiance,

$$L = \frac{\epsilon M}{\pi} \quad \frac{W}{cm^2 sr} .$$

The integration was done numerically using a program for the TI - 59 calculator, details of which are given in Appendix B. The results of our calculations are shown in the following Tables 13 to 17.

TABLE 13
R/V "POINT SUR" RADIANCE MEASUREMENTS "A"

DATE / TIME : 14 MAY 09:00 - 09:25
WIND SPEED / DIRECTION : 4.8 m/sec 290-- 300°
AIR TEMPERATURE : 10.5°C
AMBIENT TEMPERATURE : 15°C
SEA SURFACE TEMPERATURE : 12.6°C
OVERCAST, RAZY, VISIBILITY 4 NM
ATMOSPHERIC TRANSMITTANCE : 0.8679

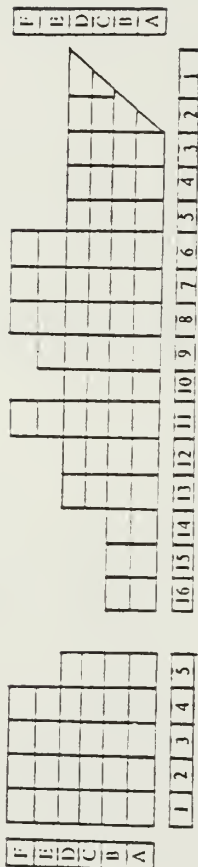


RADIANCE ($W/cm^2 \cdot sr \times 10^{-3}$)

STARBOARD SIDE						PORT SIDE						STERN					
A	B	C	D	E	F	A	B	C	D	E	F	A	B	C	D	E	F
1		4.1027	4.0875			1		4.1034	4.1199			1	4.2186	4.2868	4.2604	4.3857	4.3236
2	4.1226	4.1434	4.1344	4.1130		2	4.0779	4.1378	4.1344	4.1427		2	4.2186	4.2755	4.2108	4.2614	4.2832
3	4.1565	4.1795	4.1413	4.1289		3	4.1199	4.1517	4.1565	4.1392		3	4.2326	4.2832	4.2473	4.2473	4.2614
4	4.1444	4.2039	4.1496	4.1579		4	4.1261	4.1468	4.1420	4.1289		4	4.2256	4.2755	4.2543	4.2255	4.2614
5	4.1718	4.1948	4.1676	4.1565		5	4.1392	4.1642	4.1448	4.1565		5	4.2186	4.2508			
6	4.1767	4.2592	4.1683	4.1552	4.1185	6	4.1441	4.2088	4.1489	4.1323	4.0999						
7	4.2088	4.2882	4.1809	4.1552	4.1365	7	4.1635	4.2452	4.1864	4.2284	4.1226	4.1247					
8	4.2185	4.2410	4.2368	4.1538	4.1503	8	4.1809	4.2642	4.1816	4.1517	4.1656	4.1358					
9	4.2298	4.2494	4.2691	4.2067	4.1785	9	4.1885	4.2628	4.1670	4.1392	4.1524						
10	4.2438	4.3592	4.3471	4.2207		10	4.2269	4.2719	4.2213	4.1760							
11	4.2585	4.3972	4.3556	4.3893	4.3972	11	4.2480	4.3286	4.3878	4.4050	4.4050	4.2661					
12	4.2255	4.3721	4.2797	4.1969		12	4.2102	4.3144	4.2988	4.2059							
13	4.2059	4.2924	4.2797	4.1767		13	4.2018	4.3108	4.2726	4.1628							
14	4.2109	4.1823				14	4.1697	4.2059									
15	4.2011	4.1850				15	4.1427	4.1878									
16	4.2004	4.1656				16	4.1372	4.1878									

TABLE 14
R/V "POINT SUR" RADIANCE MEASUREMENTS "B"

DATE / TIME : 18 MAY 11:57 - 13:07
WIND SPEED / DIRECTION : 6.26 m/sec 270° - 280°
AIR TEMPERATURE : 9.7°C
AMBIENT TEMPERATURE : 17°C
SEA SURFACE TEMPERATURE : 13.1°C
OVERCAST, HAZY, VISIBILITY 3 NM
ATMOSPHERIC TRANSMITTANCE : 0.8539



RADIANCE ($W/cm^2 \cdot sr \times 10^{-3}$)

STERN						
	A	B	C	O	E	F
1	4 1137	4 1635	4 1635	4 2417	4 2635	4 2276
2	4 1137	4 1635	4 1558	4 2129	4 2487	4 1774
3	4 1137	4 1635	4 1558	4 1420	4 1635	4 1282
4	4 1137	4 1489	4 1635	4 1282	4 1282	
5	4 1137	4 1420	4 1489	4 1282		

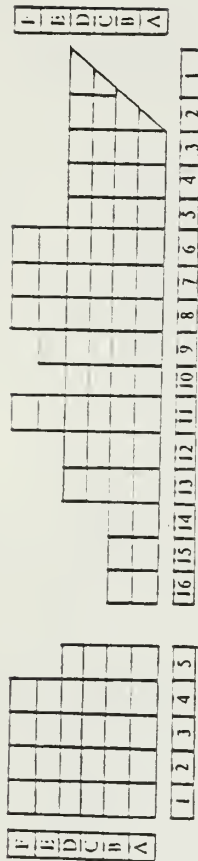
PORT SIDE						
	A	B	C	O	E	F
1			4 1351	4 1137		
2	4 0992	4 1420	4 1351	4 1351		
3	4 1137	4 1843	4 1351	4 1489		
4	4 1275	4 1920	4 1420	4 1628		
5	4 1351	4 2199	4 1704	4 1704		
6	4 1489	4 2199	4 1704	4 1774	4 0992	4 0924
7	4 1559	4 2487	4 1843	4 1774	4 1558	4 0999
8	4 1704	4 2635	4 1843	4 1365	4 1558	4 1282
9	4 1843	4 2635	4 1365	4 1420	4 1489	
10	4 1843	4 2635	4 2199	4 1420		
11	4 2347	4 2635	4 2635	4 2635	4 2635	4 2059
12	4 2199	4 2635	4 2635	4 2059		
13	4 2059	4 2487	4 1843	4 1635		
14	4 1774	4 2129				
15	4 1558	4 1843				
16	4 1068	4 1635				

STARBOARD SIDE						
	A	B	C	O	E	F
1			4 1351	4 1068		
2	4 0924	4 1275	4 1137	4 1351		
3	4 1137	4 1704	4 1206	4 1378		
4	4 1275	4 1774	4 1275	4 1420		
5	4 1351	4 2059	4 1558	4 1420		
6	4 1420	4 2347	4 1628	4 1351	4 0574	4 0786
7	4 1206	4 2417	4 1558	4 1275	4 0574	4 0924
8	4 1275	4 2417	4 1704	4 1206	4 0786	4 1068
9	4 1489	4 2417	4 1774	4 1068	4 0927	
10	4 1635	4 2417	4 1489	4 0992		
11	4 1843	4 2564	4 2564	4 2564	4 2564	4 2059
12	4 1843	4 2276	4 1774	4 1969		
13	4 1774	4 2199	4 1628	4 1628		
14	4 1704	4 2129				
15	4 1558	4 2129				
16	4 0924	4 1275				

TABLE 15

R/V "POINT SUR" RADIANCE MEASUREMENTS "C"

DATE / TIME : 21 MAY 00:05 - 00:13
 WIND SPEED / DIRECTION : 5.2 m/sec 270° - 300°
 AIR TEMPERATURE : 11.3°C
 AMBIENT TEMPERATURE : 17°C
 SEA SURFACE TEMPERATURE : 11.9°C
 CLEAR, VISIBILITY 9 NM
 ATMOSPHERIC TRANSMITTANCE : 0.8640



RADIANCE ($\text{W/cm}^2 \cdot \text{sr} \times 10^{-3}$)

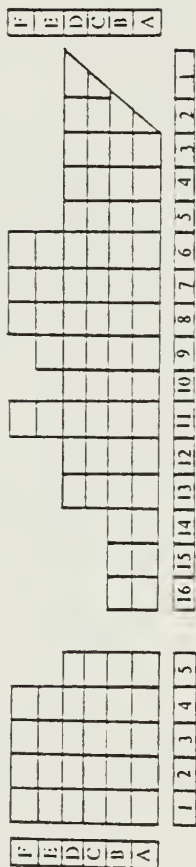
STARBOARD SIDE						
A	B	C	D	E	F	
1		4.0458	4.0492			
2	4.0731	4.1191	4.1239	4.0902		
3	4.0964	4.1363	4.1321	4.0936		
4	4.1046	4.1341	4.1356	4.1005		
5	4.1046	4.1314	4.1314	4.1005		
6	4.0970	4.1239	4.1094	4.0936	4.0594	4.0594
7	4.0970	4.1170	4.1129	4.1129	4.0786	4.0833
8	4.1005	4.1129	4.1129	4.1570	4.1425	4.1204
9	4.1005	4.1163	4.1266	4.1591	4.1508	
10	4.1005	4.1197	4.1613	4.1418		
11	4.1785	4.2134	4.2645	4.2860	4.2860	4.2484
12	4.1753	4.2134	4.2416	4.1454		
13	4.1723	4.1897	4.1809	4.1206		
14	4.1681	4.1432				
15	4.1356	4.1197				
16	4.0888	4.1067				

PORT SIDE						
A	B	C	D	E	F	
1						
2						
3						
4						
5						
6						
7						
8						
9						
10						
11						
12						
13						
14						
15						
16						

STERN						
A	B	C	D	E	F	
1						
2						
3						
4						
5						

TABLE 16
R/V "POINT SUR" RADIANCE MEASUREMENTS "D"

DATE / TIME : 21 MAY 17:18 - 17:37
WIND SPEED / DIRECTION : 10.2 m/sec 320°
AIR TEMPERATURE : 12.2°C
AMBIENT TEMPERATURE : 19°C
SEA SURFACE TEMPERATURE : 13.2°C
SUN, CLEAR, VISIBILITY 10 NM
ATMOSPHERIC TRANSMITTANCE : 0.8178



RADIANCE ($W/cm^2 \cdot sr \times 10^{-3}$)

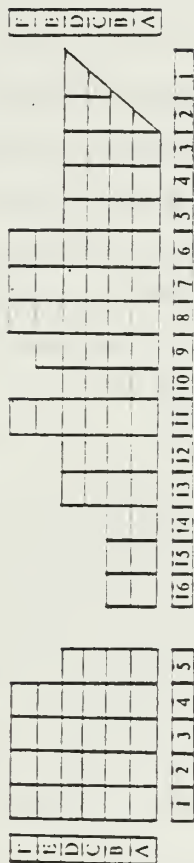
STARBOARD SIDE						
A	B	C	D	E	F	
1		4.1857	4.1933			
2	4.1892	4.2142	4.2036	4.1933		
3	4.1892	4.2142	4.2072	4.2038		
4	4.1892	4.2072	4.2072	4.2072		
5	4.1933	4.2072	4.2003	4.2718		
6	4.2142	4.2359	4.2500	4.2936	4.2430	4.2003
7	4.2282	4.2528	4.2718	4.2936	4.2528	4.2072
8	4.2282	4.2429	4.2786	4.2788	4.2430	4.2072
9	4.2359	4.2528	4.2528	4.2788	4.2609	
10	4.2359	4.2528	4.2718	4.2788		
11	4.2429	4.3149	4.3589	4.3589	4.3222	
12	4.2359	4.3078	4.2858	4.2647		
13	4.2212	4.2786	4.2786	4.2647		
14	4.2142	4.2647				
15	4.2142	4.2500				
16	4.2142	4.2359				

PORT SIDE						
A	B	C	D	E	F	
1		4.1420	4.1662			
2	4.1090	4.1579	4.1995	4.1829		
3	4.1255	4.1912	4.2330	4.1995		
4	4.1629	4.2247	4.2582	4.2079		
5	4.1912	4.2499	4.2751	4.2079		
6	4.1995	4.2751	4.2582	4.2414	4.1995	4.1745
7	4.1995	4.2667	4.2751	4.2499	4.2414	4.1912
8	4.2107	4.2920	4.2751	4.2582	4.2330	4.1995
9	4.2246	4.3083	4.2836	4.2582	4.2456	
10	4.2499	4.3175	4.3260	4.2582		
11	4.3348	4.4713	4.5404	4.5404	4.5404	4.4540
12	4.2913	4.4195	4.3338	4.2751		
13	4.2247	4.3338	4.2752	4.2414		
14	4.1996	4.2330				
15	4.1662	4.1995				
16	4.1496	4.1829				

STERN						
A	B	C	D	E	F	
1	4.1739	4.2409	4.3078	4.4972	4.5402	4.5139
2	4.1780	4.3255	4.3589	4.3847	4.3511	4.1989
3	4.1822	4.2577	4.3589	4.3419	4.2661	4.1989
4	4.1739	4.2577	4.3511	4.3419	4.3419	4.2072
5	4.1739	4.2479	4.3255	4.3419	4.3000	4.1989

TABLE 17
R/V "POINT SUR" RADIANCE MEASUREMENTS "E"

DATE / TIME : 22 MAY 00:48 - 01:03
WIND SPEED / DIRECTION : 9.5 m/sec 290°
AIR TEMPERATURE : 9.7°C
AMBIENT TEMPERATURE : 17°C
SEA SURFACE TEMPERATURE : 10.8°C
CLEAR, VISIBILITY 10 NM
ATMOSPHERIC TRANSMITTANCE : 0.8232



RADIANCE ($W/cm^2 \cdot sr \times 10^{-3}$)

STARBOARD SIDE						PORT SIDE						STERN								
	A	B	C	D	E	F		A	B	C	D	E	F		A	B	C	D	E	F
1			3.9463	3.9226			1			3.9329	3.9222			1	3.9396	3.9672	3.9753	4.0923	4.0923	4.0855
2	3.9463	4.0084	3.9604	3.9262			2	3.9329	3.9948	3.9537	3.9295			2	3.9396	3.9463	3.9881	3.9949	3.9807	3.9672
3	3.9497	3.9982	3.9564	3.9396			3	3.9329	3.9813	3.9537	3.9295			3	3.9396	3.9463	4.0227	4.0091	3.9571	3.9463
4	3.9497	3.9739	3.9564	3.9396			4	3.9329	3.9604	3.9396	3.9262			4	3.9396	3.9463	3.9739	4.0091	3.9503	3.9329
5	3.9429	3.9739	3.9429	3.9329			5	3.9262	3.9463	3.9262	3.9181			5	3.9396	3.9396	3.9463	3.9604	3.9463	3.9329
6	3.9329	3.9396	3.9329	3.9463	3.9329	3.9262	6	3.9262	3.9463	3.9181	3.9181	3.9329	3.9463							
7	3.9329	3.9396	3.9362	3.9564	3.9537	3.9329	7	3.9362	3.9329	3.9181	3.9329	3.9672	3.9537							
8	3.9329	3.9262	3.9429	3.9881	3.9739	3.9463	8	3.9362	3.9396	3.9181	3.9396	3.9813	3.9604							
9	3.9262	3.9181	3.9463	3.9497	3.9618		9	3.9329	3.9329	3.9262	3.9262	3.9537								
10	3.9262	3.9262	3.9463	3.9537			10	3.9396	3.9537	3.9463	3.9463									
11	3.9329	3.9329	3.9537	3.9948	4.0855	4.0363	11	3.9813	4.0855	4.0855	4.0855	4.0855	4.0363							
12	3.9463	3.9813	3.9881	3.9537			12	3.9537	4.0500	4.0227	3.9813									
13	3.9463	3.9813	3.9813	3.9396			13	3.9463	4.0363	4.0226	3.9672									
14	3.9396	3.9537					14	3.9396	3.9813											
15	3.9295	3.9463					15	3.9396	3.9537											
16	3.9295	3.9463					16	3.9329	3.9463											

VIII. DATA ANALYSIS

A. INTRODUCTION

In this chapter we will analyze how the sea background radiance was affected due to reflected sky thermal radiation. We will discuss how the reflectance and the emissivity of a sea surface roughened by various wind speeds affected the background radiance. Also we will calculate the apparent temperature of the sea surface, and will find the effective target to background temperature difference sensed by the Thermovision under the specific environmental conditions experienced.

B. EFFECTIVE SEA SURFACE TEMPERATURE

1. Sea Surface Radiance

As mentioned in Chapter III the infrared radiance of the sea is the sum of the radiance due to thermal emission and the radiance due to reflected incident radiation.

The reflected incident radiation in the spectral region of 8 - 14 μm is only thermal sky radiation by day and night. The contribution of this radiation to the total sea radiance depends on the reflectance of the sea surface (R).

Because the water is essentially opaque in the above spectral region the reflectance also controls the emissivity of the sea surface, since for an opaque material we can write $\epsilon = 1 - R$.

Therefore, we can write that the total radiance of the sea surface is

$$L_s = (1 - R) L_w + R L_{\text{sky}}, \quad (\text{eqn 8.1})$$

where L_s is the radiance of the sea surface. L_w is the radiance due to sea water thermal emission and L_{sky} is the radiance of the sky. To write this equation we assumed that the emissivity of the sky, as we have previously discussed in detail, is one.

2. Reflectance of the Sea Surface

An important factor in determining the reflectance of a surface is its geometry. For the sea surface this geometry depends on the slope distribution of the waves at various wind speeds.

In our discussion about the geometry of the sea surface we have shown, in Fig 3.8, the difference in reflectance between a flat sea surface and a surface roughened by a Beaufort 4 wind speed.

These results, as Fig 3.8, were obtained by Cox and Munk, working in the visible range with solar radiation. Such information is lacking for the infrared and night conditions, although the above curves seem to be helpful in this area also. We make this assumption since the reflectance of the sea water at zero angle of incidence is almost equal to the average reflectance in the infrared region from 2 - 15 μm (see Fig 3.4), and the sky radiance variation is almost the same for day and night conditions.

For our analysis we used the same curves corrected for the average index of refraction in the spectral region 8 - 14 μm . Actually we wanted to find a correction factor for the reflectance. Since we knew the index of refraction of water for both the visible and 8 - 14 μm regions, we could find the corresponding reflectances at normal incidence using the equation $R(0) = (n - 1)^2 / (n + 1)^2$. Their ratio gave us the required correction factor. This factor was used to correct the given curves, assuming that the correction we found for normal incidence applied for all incidence angles.

[Ref. 7] gives the index of refraction used to calculate the reflectance, for uncontaminated sea water, as $n = 1.338$ and quotes the corresponding calculated value of $R_v(0)$ as 0.020. Even though the reflectance equation for $n = 1.338$ gives $R_v(0) = 0.02089$, we will use for our calculations the value of 0.020 used to draw the curves. The average index of refraction for the region 8 - 14 μm was found from Fig 3.5 to be $n = 1.303$; with this index of refraction the reflectance was calculated as $R_{ir}(0) = 0.01731$. As we can see the reflectance for the region 8 - 14 μm at normal incidence is lower than the reflectance in the visible region, in the ratio of $R_{ir}(0) / R_v(0) = 0.865$. With this correction the curves were shifted a little lower.

The following Tables 19 to 23 at the end of this chapter show the reflectance (R) values and the emissivity ($1 - R$) values as they were found from the corrected curves, for a flat sea surface and one roughened by a Beaufort 4 wind, for certain angles of incidence. Here we reiterate that the values obtained for incidence angles near the horizon are less accurate, because the curves are not strictly applicable in this area, as discussed in Chapter III.

3. Apparent Temperature Calculation

As we said before in section one, the sea surface radiance can be written as the following sum (Eqn 8.1)

$$L_s = (1 - R) L_w + R L_{sky} ,$$

that is, that the radiant flux of the sea surface is the sum of the emitted radiant flux and the reflected incident radiant flux. For the whole spectral region we can write

$$\sigma T_s^4 = (1 - R) \sigma T_w^4 + R \sigma T_{sky}^4, \quad (\text{eqn 8.2})$$

where T_s is the apparent sea surface temperature, T_w is the actual sea surface temperature and T_{sky} is the temperature of the atmospheric air. Dividing both sides of the equation by σ we get the more simplified form

$$T_s^4 = (1 - R) T_w^4 + R T_{sky}^4 \quad (\text{eqn 8.3})$$

With this equation we could calculate the apparent sea surface temperature, the temperature that our thermal system would sense if it were operating in the whole spectrum region and the atmospheric attenuation was neglected.

With the above assumption, we calculated with moderate precision, for the region of observation, the apparent sea surface temperature for a flat sea surface and one roughened by Beaufort 4 wind. Calculations were done for incident angles at 89° , where we had been working, 85° , 80° , 75° and 70° . The reflectance (R) for the two kinds of surfaces and the incidence angles listed was found using the curves in Fig 3.8. after being corrected for the spectral region 8 - $14\mu\text{m}$. The actual sea and air temperatures were taken from the recorded meteorological data on the ship.

The results of these calculations are shown in the Tables 19 to 23 at the end of the chapter. Detailed analysis and discussion of these results is given in the following section.

4. Calculated Temperature Data Discussion and Presentation

From the equation we used to calculate the apparent sea surface temperature we can see that the two terms at the right side are inversely related to the reflectance of the sea surface.

Therefore, when the reflectance of the sea surface is high, the term with the sky temperature (T_{sky}) dominates, and conversely when the reflectance is low the term with the actual sea surface temperature (T_w) dominates. So whenever the reflectance was high the apparent sea surface temperature we had calculated was closer to the sky temperature. Since for our case the sky temperature was always lower than the actual sea surface temperature, the apparent sea surface temperatures we have calculated were lower than the actual. On the contrary, whenever the reflectance was low, which means that the emissivity of the sea surface was high, the apparent sea surface temperatures we have calculated were close to the actual sea surface

temperatures, but still some tenths of a degree lower, because of the small contribution from the second term.

Looking at the reflectance values given for the two kinds of surfaces, at various incident angles, in Tables 19 to 23 we see that, for large incidence angles (i.e., grazing incidence) the difference in reflectance of the two surfaces is large. But as the incidence angle decreases the difference decreases and at about 70° goes to zero. (for more details see Fig 3.8). For this reason the difference between the apparent temperatures we have calculated is large at high incidence angles (89° , 85°) but goes to a few tenths at 70° .

The calculated temperatures are shown in the T_s row of the Tables 19 to 23. In the T_d row the difference between the actual sea surface water temperature and the calculated sea surface temperature is shown. T_m is the temperature computed by the Thermovision 780 system, divided by the atmospheric attenuation. This was done because we wanted to compare this temperature with the T_s temperatures. But since the T_s temperatures do not include any atmospheric attenuation, it was necessary either to include the atmospheric attenuation into these values or amplify the Thermovision measurement, to obtain a value without the atmospheric attenuation. We followed the second method and we got the values T_m shown in the Tables 19 to 23.

Comparing these T_m values with the T_s values we have calculated for incident angle at 89° , we can see clearly how much the reflectance of the sea surface, roughened at various wind speeds, was affecting the temperature sensed by the Thermovision.

Finally in the T_{md} row of the Tables 19 to 23, the difference between the actual sea surface temperature and the T_m temperature is shown. As we have expected this difference is big at low wind speeds when the reflectance is high and the apparent temperature is closer to the sky temperature.

Generally we can say that the apparent sea surface temperatures found were lower than the actual sea surface temperatures, since the sky was always colder. Their difference was related to the incidence angle and the roughness of the sea surface, with higher values at incidence angles near the horizon and lower wind speeds.

C. TARGET-TO-BACKGROUND TEMPERATURE DIFFERENCE

1. Effective Temperature Difference

An important factor for the target detection probability of an infrared system, is the target-to-background temperature difference. The higher the temperature difference between a target and its background the greater the probability and the distance of detection.

But as we said before the effective temperature difference (ΔT) that our thermal system would sense, under various environmental conditions, looking at various incidence angles, might not be the same as the actual temperature difference.

Therefore, the precalculated detection distance, using the actual temperatures, at which we expect our system to detect a specific target, may not coincide with the actual distance at which the target is detected by the system.

In this analysis we attempted to find the effective ΔT , sensed by the Thermovision, under the various environmental conditions worked in, and compare it with the actual ΔT . The effective ΔT was found by taking the difference between the temperatures the system calculated for the hottest spot on the ship, ie. the stack, and the sea surface. These temperatures, were calculated under the ideal conditions in which a thermal imaging system operates, considering emissivity one ($\epsilon = 1$) and neglecting atmospheric attenuation ($\tau_a = 1$), and were corrected using the calibration relation we had derived. The actual ΔT was found using the temperature of the stack, computed from the radiation measurements using the exact parameters (emissivity, atmospheric attenuation, etc.).

These temperatures, after being corrected for calibration purposes, were the most accurate available for our case, since we did not have any thermocouples on the stack to give a direct indication of the actual temperature. The temperature of the sea surface was taken from the meteorological data recorded on the ship.

From this analysis we found that the effective ΔT , for the environmental conditions of the measurements and incidence angles near the horizon, was always higher, by about a factor of 1.6 to 2, than the actual ΔT . This was an indication that variations in emissivity and reflectance of the sea surface under the experienced environmental conditions had affected the effective ΔT , sensed by the Thermovision.

Our results are shown in Tables 19 to 23 at the end of the chapter. A more detailed discussion of these results is given in the following section.

2. Temperature Difference Data Discussion and Presentation

The AGA temperatures shown in the Tables 19 to 23, for the hottest spot on the ship and the sea surface are temperatures calculated by the computer program using the thermal values measured with the Thermovision 780, assuming $\varepsilon = 1$ and $\tau = 1$ and corrected for calibration.

Therefore, these temperatures correspond to the thermal radiation attenuated by the atmospheric effects and the emissivity of the measured surface. They are the effective temperatures our system was sensing under the environmental conditions experienced on each date, at high incidence angles near the horizon (about 89°).

The values we present in the Tables 19 to 23 for both the effective and actual temperatures are the average values from the data we obtained for each observation date.

Comparing the effective with the actual ΔT values we got for each observation period, we see that the effective ΔT for the environmental conditions experienced was always higher than the actual. It is obvious that there are two main factors causing the higher effective ΔT , the emissivity difference between the two surfaces and the reflected incident radiation. Since the emissivity difference was small, the dominant factor was the reflected incident radiation. Because the reflectance of the ship surface was too small ($\varepsilon = 0.95$) to cause such a difference, it was the reflectance of the sea surface we had to check. But we have already done this in the previous sections the calculation of the apparent sea surface temperature. Then the conclusion was reached that the apparent sea surface temperature was lower than the actual sea surface temperature because the sky was always colder than the sea for the local conditions. These lower temperatures were related to the incidence angle and the roughness of the sea surface, with the lower values noticed at incident angles near the horizon and low wind speeds.

Hence the Thermovision was sensing lower sea surface temperatures due to reflected thermal radiation from the colder sky. This was causing the effective ΔT to be higher than the actual. Therefore, we would expect these lower sea surface temperatures and high ΔT s to be related to the wind speed conditions which control the roughness and consequently the reflectance of the sea surface, since the incidence angle was effectively constant (near the horizon, about 89°).

From the tabulated and plotted (Fig 8.1 at the end of the chapter) ratio of the effective and the actual ΔT for the various wind speed conditions we experienced, a significant trend can be seen. Even with the assumptions and cumulative errors

inherent in the approach it can be seen that for the lower wind speed of 4.8 m/s on the 14th of May we had an effective ΔT higher than the actual by about a factor of 2.01 and for the higher wind speed 10.2 m/s on the 21st of May (17:18 - 17:37) we had an effective ΔT higher only by about a factor 1.63.

Thus as expected for the lower wind speed, higher reflectance, we had the higher ΔT and for the higher wind speed, lower reflectance, lower ΔT . It was obvious that the effective ΔT was strongly dependent on the reflected incident sky radiation. Also within the spread of the plotted points we may conclude that the ΔT ratios are proportional to the wind speeds.

D. CALCULATION EXAMPLE

1. Introduction

To help understanding of the following Tables 19 to 23, we give here a calculation example to show how the data presented were obtained. In this example we use the information we had for the 18th of May experiment.

DATE - TIME : 18th MAY 11:57 - 13:07

AIR TEMPERATURE (T_{sky}) : 9.7°C

SEA SURFACE TEMPERATURE (T_w) : 13.1°C

WIND SPEED - DIRECTION : 6.26 m/s(B-4) 280°

OVERCAST, HAZY, VISIBILITY 3 NM

ATMOSPHERIC TRANSMITTANCE : 0.8539

Average temperatures computed from Thermovision values for the hottest point on the ship (Hot Spot) and the sea surface temperature (S.S.T.), (assuming $\epsilon = 1$ and $\tau_a = 1$) are as follows:

UNCALIBRATED VALUES : Hot Spot : 22.80°C
S.S.T : 20.65°C

CALIBRATED VALUES : Hot Spot : 11.72°C
S.S.T : 9.52°C

All data for this date were collected using THERMAL RANGE 2 so the calibrated values were found using the straight line equation $Y = (1.0238) X - 11.62$.

The relation between the Beaufort sea state scale and wind speed (m.s) is shown below in Table 18.

TABLE 18
BEAUFORT SCALE

B	WIND SPEED m.s
0	0.00 - 0.46
1	0.51 - 1.54
2	2.06 - 3.08
3	3.60 - 5.14
4	5.65 - 8.23
5	8.74 - 10.80
6	11.31 - 13.89

2. Apparent Sea Surface Temperature

To calculate the sea surface apparent temperature we used Equation 8.3

$$T_s^4 = (1 - R) T_w^4 + R T_{sky}^4.$$

Using the values in Fig 3.8 for incidence angle 89° , where we have been working, we got the reflectance values for the flat sea surface and that roughened by a Beaufort 4 wind. These values, corrected for the spectral region 8 - 14 μm using the correction factor $R_{ir} R_v = 0.865$, are the following:

$$\text{FLAT SURFACE } R = 0.804$$

$$\text{ROUGHENED SURFACE } R = 0.110.$$

Therefore, from Equation 8.3 we get for the flat surface

$$T_s^4 = (1 - 0.804)(13.1)^4 + 0.110(9.7)^4$$

$$T_s = 10.65^\circ C$$

and for the rough sea surface at Beaufort 4 wind speed we get

$$T_s^4 = (1 - 0.110)(13.1)^4 + 0.110(9.7)^4$$

$$T_s = 12.84^\circ C.$$

The T_d values represent the difference ($T_w - T_s$) between the actual sea surface temperature and the apparent temperature we calculated. Hence, we have for

the flat surface $13.1 - 10.65 = 2.45^{\circ}\text{C}$ and $13.1 - 12.84 = 0.26^{\circ}\text{C}$ for the roughened surface.

The T_m value is the sea surface temperature computed by the AGA system, but without the atmospheric attenuation. To get this value we proceeded as follows. The uncalibrated value which the system calculated for the sea surface, 20.65°C , is amplified by the atmospheric transmission $\tau_a = 0.8539$; hence, we have

$$20.65 \div 0.8539 = 24.40^{\circ}\text{C} .$$

This value was corrected for calibration purposes using the straight line equation for thermal range 2 , to give

$$T_m = 24.40 (1.0238) - 11.62 = 12.83^{\circ}\text{C} .$$

As we would expect, this value must be close to the T_s value for the roughened surface (B-4), since the wind speed on this date was 6.26 m.s (B-4).

The T_{md} values are the differences $T_w - T_m$, and indicate how much colder the effective temperature sensed by the Thermovision was than the actual sea surface temperature. Hence we have

$$T_{md} = 13.10 - 12.83 = 0.27^{\circ}\text{C} .$$

3. Effective Sea Surface Temperature

As we have said before, the values given for the AGA are the values the system calculated, corrected for calibration . These values are not corrected for the atmospheric attenuation and emissivity. Therefore, for the hot spot we have the uncalibrated value 22.8°C corrected to 11.72°C , using

$$\text{AGA HOT SPOT} = 22.8 (1.0238) - 11.62 = 11.72^{\circ}\text{C} .$$

Similarly, for the value of the AGA sea surface temperature we have the uncalibrated value 20.65°C which corrected gives the value 9.52°C .

For the actual conditions, the temperature of the hottest spot on the ship, since we did not have any thermocouples on this location , was taken as the highest temperature we found for this location in the calculated temperature distribution of the ship. This value for the 18th of May was 14.28°C . The sea surface temperature was taken from the recorded data on the ship.

The ΔT value represents the hot spot to sea surface temperature difference. Hence, we have effective $\Delta T_e = 2.20^\circ\text{C}$, from

$$\Delta T_e = 11.72 - 9.52 = 2.20^\circ\text{C} .$$

The actual $\Delta T_a = 1.18^\circ\text{C}$, from

$$\Delta T_a = 14.28 - 13.10 = 1.18^\circ\text{C} .$$

The ratio $\Delta T_e/\Delta T_a = 1.864$ represents the fractional increase in effective temperature for the particular environmental conditions encountered.

TABLE 19
SEA SURFACE TEMPERATURE AND EFFECTIVE ΔT "A"

DATE / TIME : 14 MAY 09:00 - 09:25
WIND SPEED / DIRECTION : 4.8 m/sec (B-3) 290°- 300°
AIR TEMPERATURE : 10.5°C
AMBIENT TEMPERATURE : 15°C
SEA SURFACE TEMPERATURE : 12.6°C
OVERCAST, HAZY, VISIBILITY 4 NM
ATMOSPHERIC TRANSMITTANCE : 0.8679

ANGLE OF INCIDENCE AND SURFACE CONDITIONS										
	89°		85°		80°		75°		70°	
	FLAT	B-4	FLAT	B-4	FLAT	B-4	FLAT	B-4	FLAT	B-4
R	0.804	0.110	0.513	0.138	0.292	0.166	0.180	0.151	0.120	0.120
1-R	0.196	0.890	0.487	0.862	0.708	0.834	0.820	0.849	0.880	0.880
Ts	11.01	12.42	11.66	12.36	12.09	12.32	12.29	12.35	12.40	12.40
Td	1.59	0.18	0.94	0.24	0.51	0.28	0.31	0.25	0.20	0.20
Tm	11.51									
Tmd	1.09									

TEMPER.	HOT SPOT	SEA SURFACE	ΔT	RATIO
AGA	15.82	8.44	7.38	2.01
ACTUAL	16.27	12.60	3.67	

R : REFLECTANCE OF THE SEA SURFACE
FLAT: FLAT SEA SURFACE
B-4 : SEA SURFACE ROUGHENED BY BEAUFORT 4 WIND
Ts : CALCULATED APPARENT SEA SURFACE TEMPERATURE
Td : DIFFERENCE BETWEEN ACTUAL AND CALCULATED SEA TEMPERATURES
Tm : AGA SEA TEMPERATURE MEASUREMENT WITHOUT ATMOSPHERIC ATTENUATION
Tmd : DIFFERENCE BETWEEN ACTUAL AND AGA SEA TEMPERATURES

* ALL TEMPERATURES ARE IN °C

TABLE 20
SEA SURFACE TEMPERATURE AND EFFECTIVE ΔT "B"

DATE / TIME : 18 MAY 11:57 - 13:07
WIND SPEED / DIRECTION : 6.26 m/sec (B-4) 270°-280°
AIR TEMPERATURE : 9.7°C
AMBIENT TEMPERATURE : 17°C
SEA SURFACE TEMPERATURE : 13.1°C
OVERCAST, HAZY, VISIBILITY 3 NM
ATMOSPHERIC TRANSMITTANCE : 0.8539

ANGLE OF INCIDENCE AND SURFACE CONDITIONS											
	39°		35°		30°		75°		70°		
	FLAT	B-4	FLAT	B-4	FLAT	B-4	FLAT	B-4	FLAT	B-4	
R	0.804	0.110	0.513	0.138	0.292	0.166	0.130	0.151	0.120	0.120	
1-R	0.196	0.890	0.487	0.862	0.708	0.834	0.820	0.849	0.880	0.880	
T _s	10.65	12.84	11.72	12.77	12.37	12.70	12.66	12.74	12.82	12.82	
T _d	2.45	0.26	1.38	0.33	0.73	0.40	0.44	0.36	0.28	0.28	
T _m	12.83										
T _{md}	0.27										

TEMPER.	HOT SPOT	SEA SURFACE	ΔT	RATIO
AGA	11.72	9.52	2.20	1.86
ACTUAL	14.28	13.10	1.18	

R : REFLECTANCE OF THE SEA SURFACE
FLAT: FLAT SEA SURFACE
B-4 : SEA SURFACE ROUGHENED BY BEAUFORT 4 WIND
Ts : CALCULATED APPARENT SEA SURFACE TEMPERATURE
Td : DIFFERENCE BETWEEN ACTUAL AND CALCULATED SEA TEMPERATURES
Tm : AGA SEA TEMPERATURE MEASUREMENT WITHOUT ATMOSPHERIC ATTENUATION
Tmd : DIFFERENCE BETWEEN ACTUAL AND AGA SEA TEMPERATURES

* ALL TEMPERATURES ARE IN °C

TABLE 21
SEA SURFACE TEMPERATURE AND EFFECTIVE ΔT "C"

DATE / TIME : 21 MAY 00:05 - 00:13
WIND SPEED / DIRECTION : 5.2 m/sec (B-4) 270°- 300°
AIR TEMPERATURE : 11.3°C
AMBIENT TEMPERATURE : 17°C
SEA SURFACE TEMPERATURE : 11.9°C
CLEAR, VISIBILITY 9 NM
ATMOSPHERIC TRANSMITTANCE : 0.8640

ANGLE OF INCIDENCE AND SURFACE CONDITIONS											
	39°		35°		30°		75°		70°		
	FLAT	B-4	FLAT	B-4	FLAT	B-4	FLAT	B-4	FLAT	B-4	
R	0.804	0.110	0.513	0.138	0.292	0.166	0.180	0.151	0.120	0.120	
1-R	0.196	0.890	0.487	0.862	0.708	0.834	0.820	0.849	0.880	0.880	
Ts	11.42	11.84	11.60	11.82	11.73	11.81	11.80	11.81	11.83	11.83	
Td	0.48	0.06	0.30	0.08	0.17	0.09	0.10	0.09	0.07	0.07	
Tm	11.65										
Tmd	0.25										

TEMPER.	HOT SPOT	SEA SURFACE	ΔT	RATIO
AGA	12.88	7.74	5.14	1.90
ACTUAL	14.60	11.90	2.70	

R : REFLECTANCE OF THE SEA SURFACE
FLAT: FLAT SEA SURFACE
B-4 : SEA SURFACE ROUGHENED BY BEAUFORT 4 WIND
Ts : CALCULATED APPARENT SEA SURFACE TEMPERATURE
Td : DIFFERENCE BETWEEN ACTUAL AND CALCULATED SEA TEMPERATURES
Tm : AGA SEA TEMPERATURE MEASUREMENT WITHOUT ATMOSPHERIC ATTENUATION
Tmd : DIFFERENCE BETWEEN ACTUAL AND AGA SEA TEMPERATURES

* ALL TEMPERATURES ARE IN °C

TABLE 22
SEA SURFACE TEMPERATURE AND EFFECTIVE ΔT "D"

DATE / TIME : 21 MAY 17:18 - 17:37
WIND SPEED / DIRECTION : 10.2 m/sec (B-5) 320°
AIR TEMPERATURE : 12.2°C
AMBIENT TEMPERATURE : 19°C
SEA SURFACE TEMPERATURE : 13.2°C
SUN, CLEAR, VISIBILITY 10 NM
ATMOSPHERIC TRANSMITTANCE : 0.8178

ANGLE OF INCIDENCE AND SURFACE CONDITIONS										
	89°		85°		80°		75°		70°	
	FLAT	B-4	FLAT	B-4	FLAT	B-4	FLAT	B-4	FLAT	B-4
R	0.804	0.110	0.513	0.138	0.292	0.166	0.180	0.151	0.120	0.120
1-R	0.196	0.890	0.487	0.862	0.708	0.834	0.820	0.849	0.880	0.880
Ts	12.41	13.10	12.72	13.07	12.93	13.05	13.04	13.06	13.09	13.09
Td	0.79	0.10	0.48	0.13	0.27	0.15	0.16	0.14	0.11	0.11
Tm	13.18									
Tmd	0.02									

TEMPER.	HOT SPOT	SEA SURFACE	ΔT	RATIO
AGA	15.30	9.26	6.04	1.63
ACTUAL	16.89	13.20	3.69	

R : REFLECTANCE OF THE SEA SURFACE
FLAT: FLAT SEA SURFACE
B-4 : SEA SURFACE ROUGHENED BY BEAUFORT 4 WIND
Ts : CALCULATED APPARENT SEA SURFACE TEMPERATURE
Td : DIFFERENCE BETWEEN ACTUAL AND CALCULATED SEA TEMPERATURES
Tm : AGA SEA TEMPERATURE MEASUREMENT WITHOUT ATMOSPHERIC ATTENUATION
Tmd : DIFFERENCE BETWEEN ACTUAL AND AGA SEA TEMPERATURES

* ALL TEMPERATURES ARE IN °C

TABLE 23
SEA SURFACE TEMPERATURE AND EFFECTIVE ΔT "E"

DATE / TIME : 22 MAY 00:48 - 01:03
WIND SPEED / DIRECTION : 9.5 m/sec (B-5) 290°
AIR TEMPERATURE : 9.7°C
AMBIENT TEMPERATURE : 17°C
SEA SURFACE TEMPERATURE : 10.8°C
CLEAR, VISIBILITY 10 NM
ATMOSPHERIC TRANSMITTANCE : 0.8232

ANGLE OF INCIDENCE AND SURFACE CONDITIONS										
	89°		85°		80°		75°		70°	
	FLAT	B-4	FLAT	B-4	FLAT	B-4	FLAT	B-4	FLAT	B-4
R	0.804	0.110	0.513	0.138	0.292	0.166	0.190	0.151	0.120	0.120
1-R	0.196	0.890	0.487	0.862	0.708	0.834	0.820	0.849	0.880	0.880
Ts	9.94	10.69	10.28	10.67	10.51	10.64	10.62	10.65	10.68	10.68
Td	0.86	0.11	0.52	0.13	0.29	0.16	0.18	0.15	0.12	0.12
Tm	10.76									
Tmd	0.04									

TEMPER.	HOT SPOT	SEA SURFACE	ΔT	RATIO
AGA	8.54	6.80	1.74	1.70
ACTUAL	11.82	10.80	1.02	

R : REFLECTANCE OF THE SEA SURFACE
FLAT: FLAT SEA SURFACE
B-4 : SEA SURFACE ROUGHENED BY BEAUFORT 4 WIND
Ts : CALCULATED APPARENT SEA SURFACE TEMPERATURE
Td : DIFFERENCE BETWEEN ACTUAL AND CALCULATED SEA TEMPERATURES
Tm : AGA SEA TEMPERATURE MEASUREMENT WITHOUT ATMOSPHERIC ATTENUATION
Tmd : DIFFERENCE BETWEEN ACTUAL AND AGA SEA TEMPERATURES

* ALL TEMPERATURES ARE IN °C

WIND SPEED TO DT RATIO RELATION

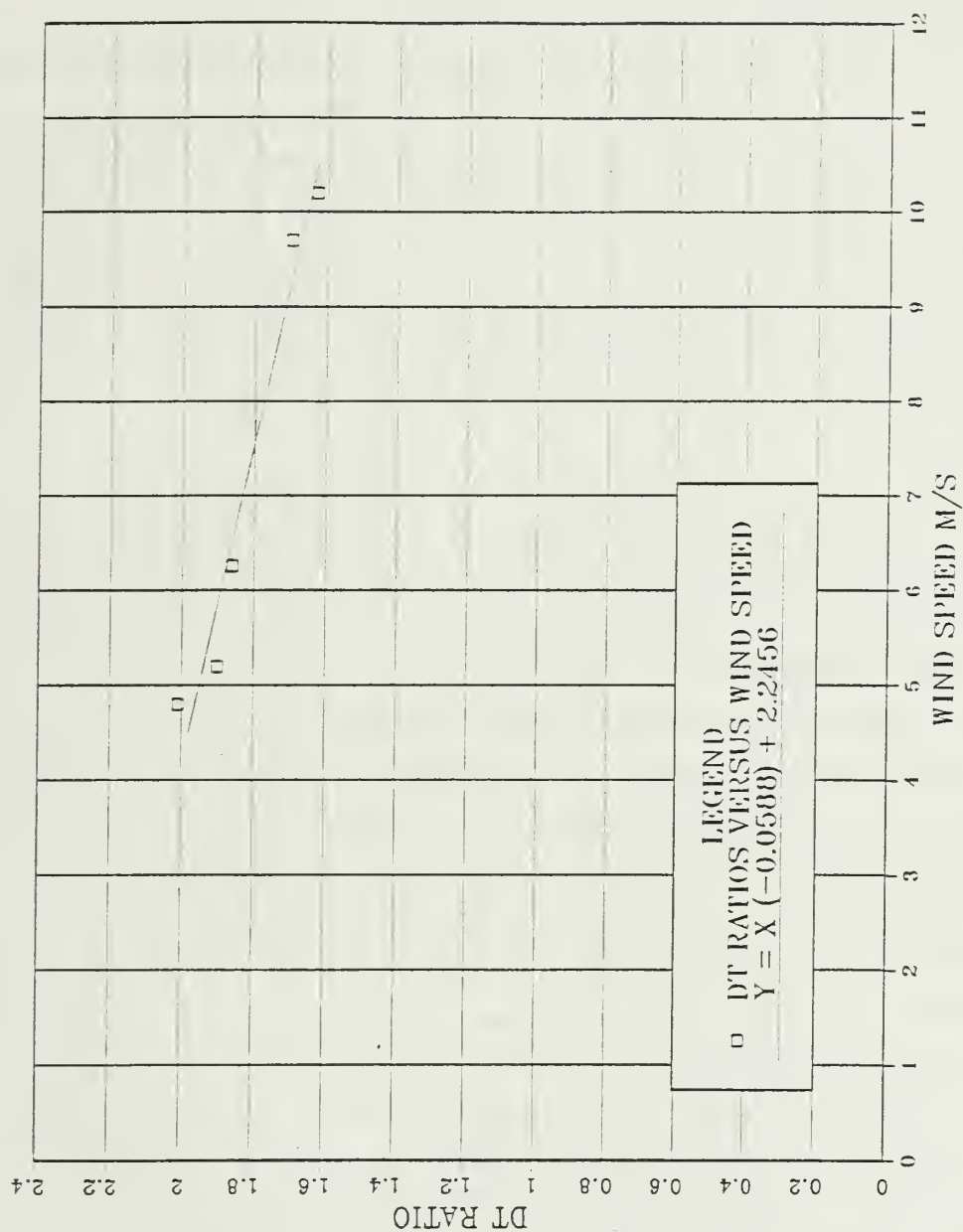


Figure 8.1 ΔT ratios plotted versus wind speed (m/s).

IX. CONCLUSIONS AND RECOMMENDATIONS

A. CONCLUSIONS

Temperature and radiance distributions of an instrumented target measured remotely by radiometric imaging with the AGA Thermovision 780 system have been compared with locally measured environmental parameters. The ship-to-background temperature difference, frequently used as a measure of the contrast, was compared as measured thermometrically with local temperature sensors and radiometrically using the Thermovision. Significant differences have been observed, depending on the time of the day, windspeed, and atmospheric conditions. These differences have been assigned to effects of the low emissivity and high reflectivity of the sea surface at near grazing angles.

Reflected thermal radiation from the sky contributed greatly to the sea surface radiance sensed by the system. Comparison of target-to-background temperature differences from radiance and from thermometric measurements showed large discrepancies due to the effect of the reflected sky radiation, characteristic of the atmospheric temperature. This reflected radiation was strongly dependent on the roughness of the sea surface under conditions of varying wind speed. The differences in the air and sea surface temperatures caused the effective (radiometric) temperature differences between the target and background to deviate both positively and negatively from the true temperature difference. With the sky colder than the sea surface, as was always found in the first series of measurements, the reflected sky radiation caused the sea surface temperature measured by the Thermovision to be lower than the actual. As a result, the effective temperature difference as observed with the Thermovision was higher than the actual difference. Both the temperature decrease and the increase in the effective temperature difference were related inversely to the sea state conditions.

An expression for the sea surface radiance including the reflected sky radiation has been developed and used to model the radiometric effective ship-to-background temperature difference. This model can be evaluated for known atmospheric conditions using the LOWTRAN 6 computer code and has been found to be consistent with observations to date.

In analysis of radiometric images of the ship taken at different aspect angles, apparent differences in radiance distribution were observed. This is considered to result from thermal radiation from hotter portions of the ship reflecting from cooler regions, increasing the apparent surface temperature. Consequently, temperature values from only those surfaces more nearly perpendicular to the line of sight were averaged to obtain representative temperature and radiance distributions.

Although the quantitative results cannot be considered to be of great accuracy, they show clearly the strong dependence of the reflected sky thermal radiation on the sea roughness due to the wind speed at the times of the observations.

B. RECOMMENDATIONS

Since we had to calibrate our system empirically to achieve the accuracy of our measurements it is obvious that we have inserted some error factors into our results. Therefore, we recommend a new series of target and background measurements to be taken with the whole system being accurately calibrated.

A few months before this work was completed the Thermovision was tested and calibrated accurately. The gain of the preamplifier in the scanner was adjusted and new calibration curves were derived. However there remained a problem in that the computer did not calculate the exact temperatures because the thermal values inserted by the system into the computer program were off by four thermal units, even though a few weeks before this work was completed we took a new series of measurements of the same target. Our results and analysis are shown in Appendix A.

All our measurements were taken at an incidence angle near the horizon where the curves in Fig 3.8, used to find the reflectance, are not strictly applicable. Therefore, depending on the operational use, we may need this information with greater accuracy, we recommend:

For systems like missiles or airborne forward looking infrared devices a series of measurements should be taken for incidence angles between 70° and 80° where the curves in Fig 3.8 are applicable, and where more accurate results can be obtained.

For forward looking devices operating on ships, with incidence angles near the horizon, long series of measurements, under all possible kinds of environmental conditions, may be needed to provide sufficiently accurate information.

APPENDIX A

DATA ANALYSIS OF LATER MEASUREMENTS

1. GENERAL

A second set of thermal imaging data were collected in mid November, 1986. All measurements were taken in the spectral region 8 -14 μm as before, using the AGA Thermovision supplemented with a microcomputer. The ship target was again the R V "POINT SUR", scheduled on an operational oceanography student cruise, and the geographic location where the thermal imaging device and the ship were positioned during the experiment was also the same.

These data were collected in order to obtain further, more accurate, measurements, under different environmental conditions, after the Thermovision had been calibrated. This was done to check our previous results and improve the information on the reflected sky thermal radiation and the effective target-to-background temperature difference relation.

2. CALIBRATION TEST

The Thermovision was accurately calibrated after the first measurements had been taken. The preamplifier gain of the scanning device which was found to be incorrectly set, was adjusted and new calibration constants were derived and inserted in the computer program. However, even if the Thermovision was operating accurately on this occasion, the temperatures calculated by the computer were not accurate. The problem lay in the thermal values transmitted to the computer from the Thermovision. The thermal values received by the computer were about 3 to 4 thermal units lower than measured directly on the Thermovision. The error was minimized by adjusting the THERMAL LEVEL control to read about 4 thermal units higher, using the THERMAL LEVEL ADJ control on the Black/White monitor chassis. In this way the the computer received almost exactly the thermal values corresponding to the object in view. Of course this was not the right way to solve the problem, since now the Thermovision was measuring thermal values 4 thermal units higher than previously. However, the system was empirically calibrated again, following exactly the same procedure described in Chapter VI.

The calibration temperature measurements for the two thermal ranges used in these series of measurements (2 and 5) are shown in the following Tables 25 and 26. The data were plotted as shown in the following Figures A.1 and A.2 and the best fit straight line was found. As can be seen from the mean and variance of the difference between the exact and calculated temperatures, the temperatures the computer calculated were very close to the exact temperatures. The correction error found this time was within 2.9 % for the thermal range 2 and 3.5 % for the thermal range 5. Of course again we have to keep in mind that these calibration functions are valid only for temperatures in the region from 5°C to 25°C.

3. MEASURED DATA

Thermal images of the target and its background were collected on the 14th of November (09:07 - 09:12), on the 16th of November (17:58 - 18:02) and on the 18th of November (08:34 - 08:36). All measurements were taken using the same equipment as before, in the same spectral region and geographic location as is described in Chapter VII. The only difference was that this time the R. V "POINT SUR" did not maneuver near the buoy to show different aspects but passed by the buoy on her way into and out of the Monterey harbor. The distance between the lab station and the ship was about 650 m on the 14th and 18th when the ship was going out of Monterey Bay showing the port side and about 750 m on the 16th on her way into the harbor showing the starboard side.

The environmental conditions experienced during these measurements are shown in the data presentation tables for each observation period (Tables 27,28,29). Generally we had low speed winds blowing from the North West, overcast skies and fog on the last day. The air temperature was always higher on this occasion (within 0.5°C to 1.9°C) than the sea surface temperature.

To analyze the data the same procedure described in Chapter VIII was followed. The apparent sea surface temperature was calculated and the effective target-to-background temperature difference, sensed by the Thermovision under the local environmental conditions, was found. These results are presented in Tables 27,28,29 at the end of this appendix. Also a plot of the ratios of the effective to actual ΔT s versus wind speed is presented in Figure A.3 after the tables.

TABLE 24
THERMAL RANGE 2
NEW CALIBRATION TEMPERATURE DATA

TEMPERATURES IN DEGREES C		
BLACKBODY EXACT	AGA COMPUTED	DIFFERENCE
5.0	4.7	0.3
6.0	5.8	0.2
7.0	6.7	0.3
8.0	7.8	0.2
9.0	8.7	0.3
10.0	9.7	0.3
11.0	11.1	-0.1
12.0	12.2	-0.2
13.0	12.8	0.2
14.0	13.7	0.3
15.0	14.9	0.1
16.0	15.9	0.1
17.0	17.2	-0.2
18.0	18.2	-0.2
19.0	18.9	0.1
20.0	20.2	-0.2
21.0	20.9	0.1
22.0	22.0	0.0
23.0	23.0	0.0
24.0	24.1	-0.1
25.0	25.2	-0.2

MEAN DIFFERENCE : 0.0286

STANDARD DEVIATION : 0.2305

VARIANCE : 0.0506

BEST FIT STRAIGHT LINE : $Y = (0.9798) X - 0.3628$

AGA CALIBRATION CURVE

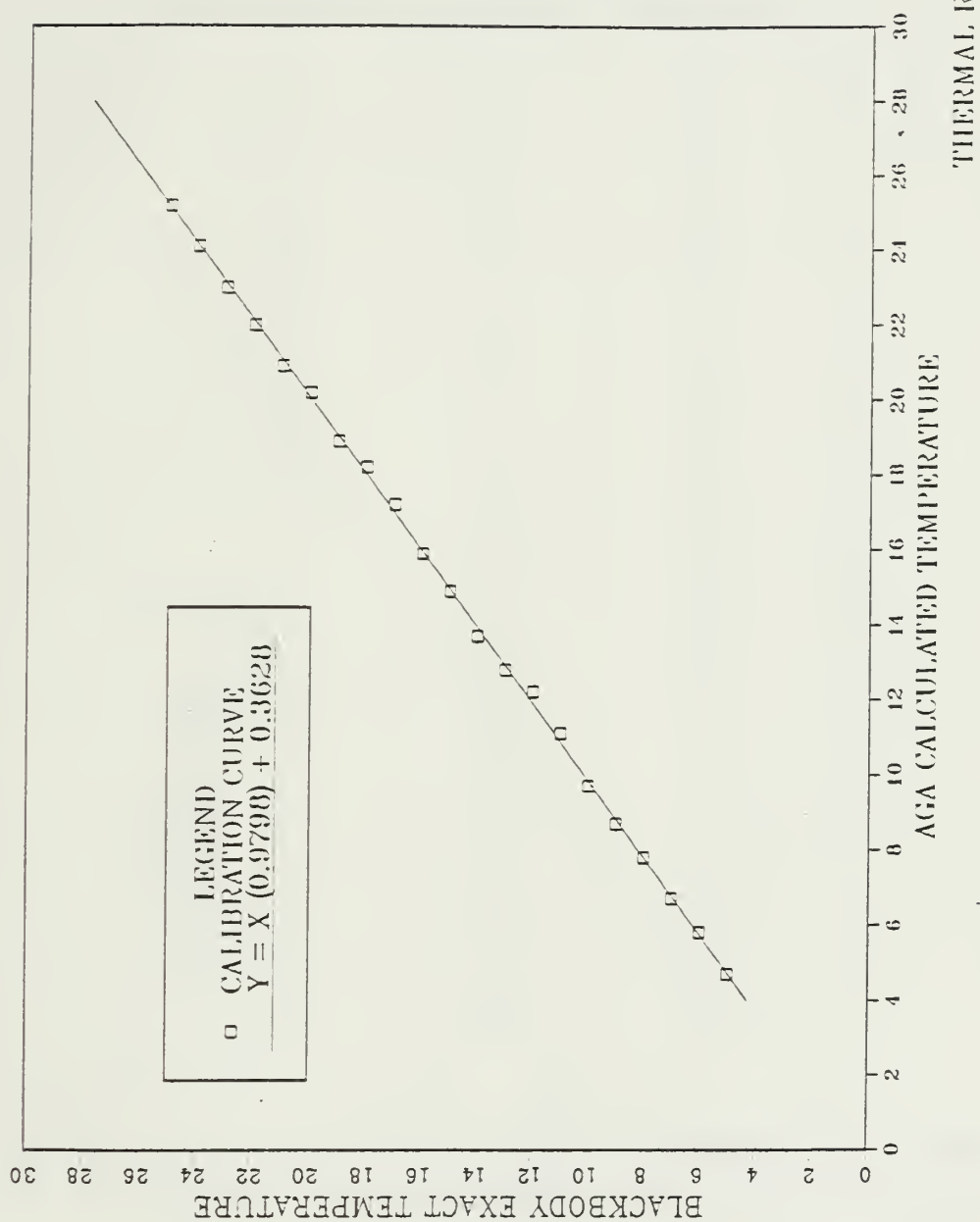


Figure A.1 Thermal Range 2 new calibration temperature data.

TABLE 25
THERMAL RANGE 5
NEW CALIBRATION TEMPERATURE DATA

TEMPERATURES IN DEGREES C		
BLACKBODY EXACT	AGA COMPUTED	DIFFERENCE
5.0	4.6	0.4
6.0	5.5	0.5
7.0	6.6	0.4
8.0	7.6	0.4
9.0	8.4	0.6
10.0	9.6	0.4
11.0	10.5	0.5
12.0	11.4	0.6
13.0	12.5	0.5
14.0	13.6	0.4
15.0	14.6	0.4
16.0	15.7	0.3
17.0	16.7	0.3
18.0	17.7	0.3
19.0	18.6	0.4
20.0	19.6	0.4
21.0	20.7	0.3
22.0	21.7	0.3
23.0	22.6	0.4
24.0	23.7	0.3
25.0	24.6	0.4

MEAN DIFFERENCE : 0.4047

STANDARD DEVIATION : 0.0921

VARIANCE : 0.0081

BEST FIT STRAIGHT LINE : $Y = (0.9920) X - 0.5217$

AGA CALIBRATION CURVE

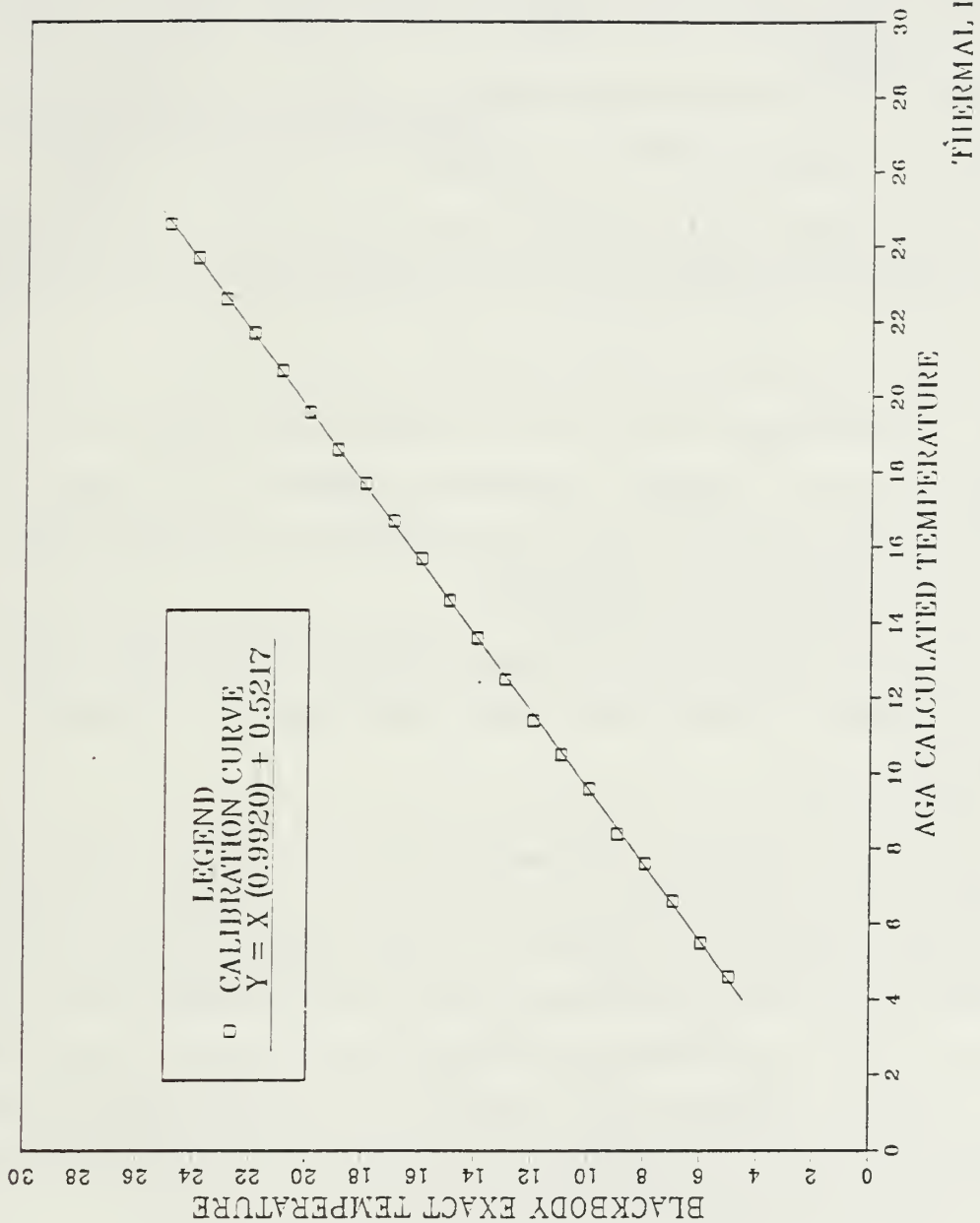


Figure A.2 Thermal Range 5 new calibration temperature data.

4. DISCUSSION AND ANALYSIS OF THE RESULTS

As was expected, reflected thermal radiation from the warmer sky affected the sea background radiance under the various sea state conditions due to the wind speeds encountered. Therefore, the apparent and the effective sea surface temperatures were found to be higher than the actual. As before, the differences between the apparent and actual sea surface temperatures were higher at incident angles near the horizontal and at lower wind speeds.

Since the effective sea surface temperature sensed by the Thermovision was higher than the actual, the effective ΔT sensed by the detector was lower than the actual ΔT .

The major error factor occurred because we did not have an indication of the actual temperature of the stack, the hottest spot on the ship, and we had to trust again the temperature the system calculated for this spot. On this exercise we did not have thermocouples positioned at various locations on the ship as we had before, to calibrate the measurements. An attempt was made to record a measure of the stack temperature, using a common thermometer fastened to the stack surface. Unfortunately since we could not place the thermometer on the surface viewed by the system, we did not get accurate measurements.

Even with all the uncertainties about the exact ΔT s and their ratios, the results show again that the variations in emissivity and reflectance of the sea surface under the local environmental conditions had affected the effective ΔT sensed by the Thermovision.

From the tabulated and plotted ratios (Fig A.3) of the effective and actual ΔT s it can be seen that for the lower wind speed of 1.5 m/s (16th Nov.), and the higher reflectance, we find the lower ΔT ratio of 0.939 . This ratio increases to 0.954 when the wind speed increases to 2 m/s (18th Nov.) and the reflectance decreases. Normally one would expect to have the higher ratio on the 14th of November when the wind speed was 2.9 m/s, but unfortunately the measured data do not seem to be consistent for that date. The temperature value recorded for the stack on this day appears inconsistent with the reliably measured values of air temperature. However, the ratio is close to one, not too far from what it is expected.

5. CONCLUSIONS AND RECOMMENDATIONS

It is noticable again in this series of measurements that reflected sky radiation affected the sea surface radiance sensed by our system. Since the sky was warmer than the sea surface , during the time periods of observation, reflected sky thermal radiation caused the sea surface temperatures sensed by the Thermovision to look higher than the actual sea surface temperature. The higher effective sea surface temperatures caused the effective ΔT s sensed by the Thermovision to be lower than the actual ΔT s under the various wind speeds experienced.

To improve the accuracy of the data set, it is recommended that a series of measurements be taken, with the whole system correctly calibrated and with a measurement of the actual temperature of the side of the stack viewed by the system.

TABLE 26
SEA SURFACE TEMPERATURE AND EFFECTIVE ΔT "F"

DATE / TIME : 14 NOV 09:07 - 09:12
WIND SPEED / DIRECTION : 2.9 m/sec (B-2) 320°
AIR TEMPERATURE : 13.9°C
AMBIENT TEMPERATURE : 15°C
SEA SURFACE TEMPERATURE : 12.2°C
TARGET DISTANCE : 650m
OVERCAST, VISIBILITY 4 NM
ATMOSPHERIC TRANSMITTANCE : 0.8864

ANGLE OF INCIDENCE AND SURFACE CONDITIONS										
	89°		85°		80°		75°		70°	
	FLAT	B-4	FLAT	B-4	FLAT	B-4	FLAT	B-4	FLAT	B-4
R	0.804	0.110	0.513	0.138	0.292	0.166	0.180	0.151	0.120	0.120
1-R	0.196	0.890	0.487	0.862	0.708	0.834	0.820	0.849	0.880	0.880
Ts	13.60	12.34	13.11	12.39	12.71	12.45	12.48	12.42	12.36	12.36
Td	-1.40	-0.14	-0.91	-0.19	-0.51	-0.25	-0.28	-0.22	-0.16	-0.16
Tm	12.56									
Tmd	-0.36									

TEMPER.	HOT SPOT	SEA SURFACE	ΔT	RATIO
AGA	15.00	11.13	3.87	1.04
ACTUAL	15.90	12.20	3.70	

R : REFLECTANCE OF THE SEA SURFACE
FLAT: FLAT SEA SURFACE
B-4 : SEA SURFACE ROUGHENED BY BEAUFORT 4 WIND
Ts : CALCULATED APPARENT SEA SURFACE TEMPERATURE
Td : DIFFERENCE BETWEEN ACTUAL AND CALCULATED SEA TEMPERATURES
Tm : AGA SEA TEMPERATURE MEASUREMENT WITHOUT ATMOSPHERIC ATTENUATION
Tmd : DIFFERENCE BETWEEN ACTUAL AND AGA SEA TEMPERATURES

* ALL TEMPERATURES ARE IN °C

TABLE 27
SEA SURFACE TEMPERATURE AND EFFECTIVE ΔT "G"

DATE / TIME : 16 NOV 17:58 - 18:02
WIND SPEED / DIRECTION : 1.5 m/sec (B-1) 320°
AIR TEMPERATURE : 15.9°C
AMBIENT TEMPERATURE : 17.5°C
SEA SURFACE TEMPERATURE : 14°C
TARGET DISTANCE : 750m
PARTIALLY CLOUDY, VISIBILITY 5 NM
ATMOSPHERIC TRANSMITTANCE : 0.8842

ANGLE OF INCIDENCE AND SURFACE CONDITIONS											
	89°		85°		80°		75°		70°		
	FLAT	B-4	FLAT	B-4	FLAT	B-4	FLAT	B-4	FLAT	B-4	
R	0.804	0.110	0.513	0.138	0.292	0.166	0.180	0.151	0.120	0.120	
1-R	0.196	0.890	0.487	0.862	0.708	0.834	0.820	0.849	0.880	0.880	
Ts	15.58	14.25	15.06	14.31	14.63	14.74	14.40	14.39	14.27	14.27	
Td	-1.58	-0.25	-1.06	-0.31	-0.63	-0.74	-0.40	-0.39	-0.27	-0.27	
Tm	14.95										
Tmd	-0.95										

TEMPER.	HOT SPOT	SEA SURFACE	ΔT	RATIO
AGA	17.38	13.22	4.16	0.939
ACTUAL	18.38	13.95	4.43	

R : REFLECTANCE OF THE SEA SURFACE
FLAT: FLAT SEA SURFACE
B-4 : SEA SURFACE ROUGHENED BY BEAUFORT 4 WIND
Ts : CALCULATED APPARENT SEA SURFACE TEMPERATURE
Td : DIFFERENCE BETWEEN ACTUAL AND CALCULATED SEA TEMPERATURES
Tm : AGA SEA TEMPERATURE MEASUREMENT WITHOUT ATMOSPHERIC ATTENUATION
Tmd : DIFFERENCE BETWEEN ACTUAL AND AGA SEA TEMPERATURES

* ALL TEMPERATURES ARE IN °C

TABLE 28
SEA SURFACE TEMPERATURE AND EFFECTIVE ΔT "H"

DATE / TIME : 18 NOV 08:34 - 08:36
WIND SPEED / DIRECTION : 2.0 m/sec (B-2) 335°
AIR TEMPERATURE : 14.8°C
AMBIENT TEMPERATURE : 16°C
SEA SURFACE TEMPERATURE : 14.38°C
TARGET DISTANCE : 650m
OVERCAST, FOGGY, VISIBILITY 1 NM
ATMOSPHERIC TRANSMITTANCE : 0.8890

ANGLE OF INCIDENCE AND SURFACE CONDITIONS											
	89°		85°		80°		75°		70°		
	FLAT	B-4	FLAT	B-4	FLAT	B-4	FLAT	B-4	FLAT	B-4	
R	0.804	0.110	0.513	0.138	0.292	0.166	0.180	0.151	0.120	0.120	
1-R	0.196	0.890	0.487	0.862	0.708	0.834	0.820	0.849	0.880	0.880	
Ts	14.72	14.42	14.60	14.44	14.50	14.45	14.46	14.44	14.43	14.43	
Td	-0.34	-0.04	-0.22	-0.06	-0.12	-0.07	-0.08	-0.06	-0.05	-0.05	
Tm	14.62										
Tmd	-0.24										

TEMPER.	HOT SPOT	SEA SURFACE	ΔT	RATIO
AGA	14.67	13.00	1.67	0.954
ACTUAL	16.13	14.38	1.75	

R : REFLECTANCE OF THE SEA SURFACE
FLAT: FLAT SEA SURFACE
B-4 : SEA SURFACE ROUGHENED BY BEAUFORT 4 WIND
Ts : CALCULATED APPARENT SEA SURFACE TEMPERATURE
Td : DIFFERENCE BETWEEN ACTUAL AND CALCULATED SEA TEMPERATURES
Tm : AGA SEA TEMPERATURE MEASUREMENT WITHOUT ATMOSPHERIC ATTENUATION
Tmd : DIFFERENCE BETWEEN ACTUAL AND AGA SEA TEMPERATURES

* ALL TEMPERATURES ARE IN °C

WIND SPEED TO DT RATIO RELATION

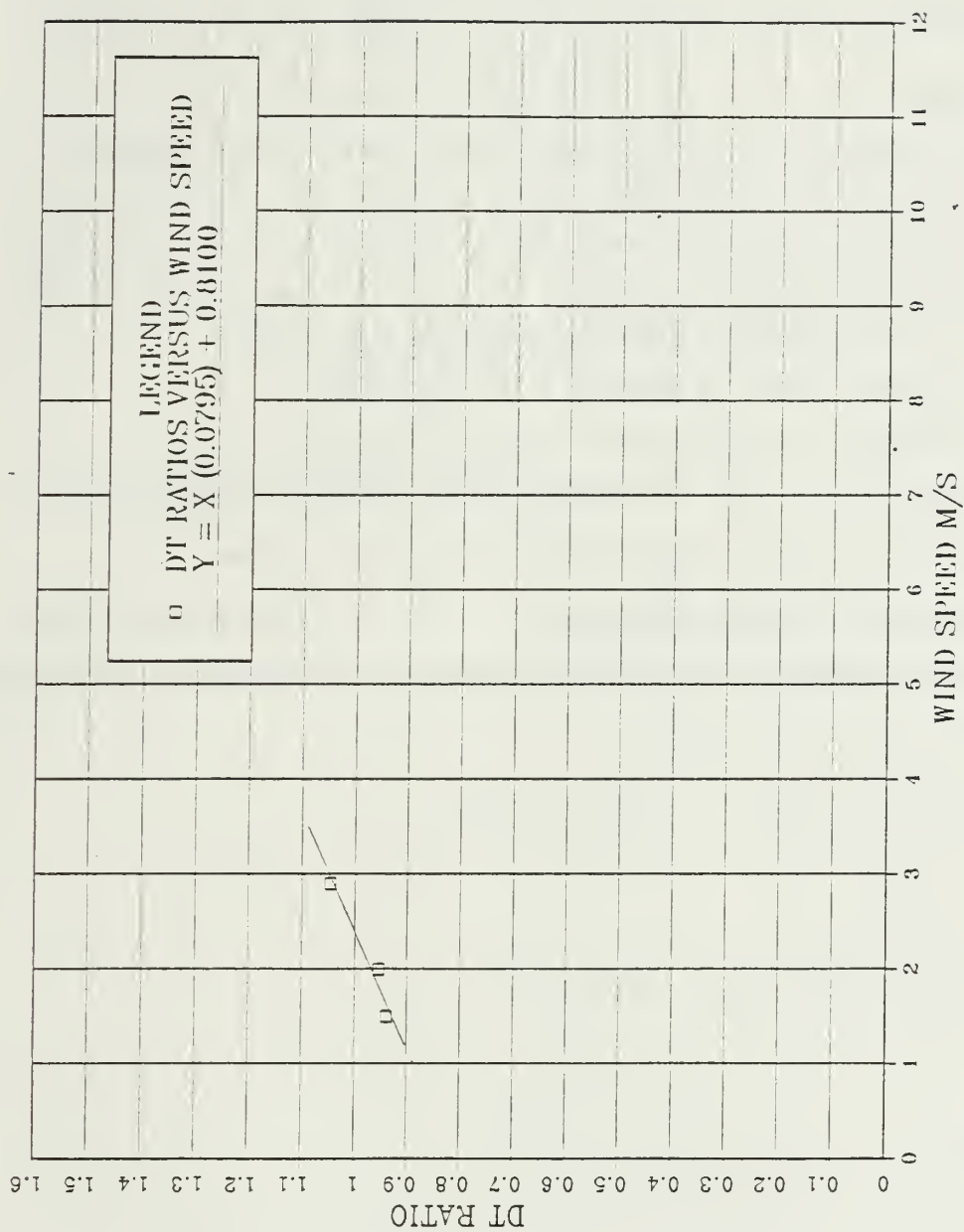


Figure A.2 ΔT ratios plotted versus wind speed.

APPENDIX B

IN-BAND FLUX CALCULATION USING TI-59 PROGRAM

1. GENERAL

The program for the TI-59 calculator used to calculate the in-band flux makes use of the Simpson's approximation program included in the master library module. It was originally written for the HP-67 calculator by Robert Pitlak (Appolo Lasers, 6357 Arizona Circle, Los Angeles CA., 90045), and has been translated for the TI-59.

To use this program the following values have to be inserted:

- a. The initial and final wavelengths of the spectral band.
- b. The temperature of the object (in °K or °F or °C).
- c. The even number of intervals to be used by the Simpson's approximation of the integral.

The calculated flux is given in Watts/cm² or photons/cm²sec

2. FORMULAE AND CONSTANTS

As we discussed in Chapter VI, Section E, Planck's blackbody law can be written in the form

$$Q = \int_{\lambda_1}^{\lambda_2} C_0 q \, d\lambda \quad \text{photons/cm}^2\text{sec}$$

$$\text{or} \quad M = \int_{\lambda_1}^{\lambda_2} C_1 (q/\lambda) \, d\lambda \quad \text{Watts/cm}^2$$

$$\text{Where} \quad q = \frac{1}{\lambda^4 (e^x - 1)} \quad x = \frac{C_2}{\lambda T}$$

$$C_0 = 2\pi c = 1.883651556 \times 10^3 \, (\mu\text{m}^3/\text{cm}^2\text{sec})$$

$$C_1 = 2\pi hc^2 = 37418.42875 \, (\text{Watts } \mu\text{m}^4/\text{cm}^2)$$

$$C_2 = hc/k = 14388.32334 \, (\mu\text{m } ^\circ\text{K})$$

The integrations are done numerically using Simpson's approximation.

3. PROCEDURE

How to use the program

- a. Load the magnetic card
- b. Press RST
- c. Enter λ_1 initial wavelength in μm , press R S
- d. Enter λ_2 final wavelength in μm , press R S
- e. Enter temperature (T), press
 - (1) A if in $^{\circ}\text{K}$
 - (2) B if in $^{\circ}\text{F}$
 - (3) C if in $^{\circ}\text{C}$
- f. Enter even number of integration intervals
- g. Press
 - (1) D to get the answer in Watts/cm^2
 - (2) E to get the answer in $\text{photons/cm}^2\text{sec}$

4. PROGRAM LISTING

In the following Table 24 we give the listing of the program used in the TI-59 calculator.

TABLE 24
TI-59 PROGRAM LISTING

000	42	STO	055	07	7	114	02	2	174	23	LHX
001	01	01	056	03	3	115	03	3	175	42	STO
002	99	PRT	057	95	=	116	03	3	176	06	06
003	91	R/S	058	42	STO	117	04	4	177	36	PGM
004	42	STO	059	00	00	118	55	+	178	09	09
005	02	02	060	91	R/S	119	43	RCL	179	14	D
006	99	PRT	061	75	LSL	120	07	07	180	22	INV
007	91	R/S	062	13	0	121	55	+	181	52	EE
008	75	LSL	063	42	STO	122	43	RCL	182	99	PPT
009	11	A	064	00	00	123	00	00	183	98	ADV
010	42	STO	065	01	1	124	54)	184	91	P/S
011	00	00	066	05	5	125	54)	185	75	LSL
012	02	2	067	00	0	126	75	-	186	15	E
013	06	6	068	00	0	127	01	1	187	98	ADV
014	00	0	069	00	0	128	54)	188	42	STO
015	00	0	070	00	0	129	54)	189	05	05
016	00	0	071	69	DP	130	35	1/X	190	99	PRT
017	00	0	072	04	04	131	65	X	191	99	ADV
018	69	DP	073	43	RCL	132	43	RCL	192	50	(
019	04	04	074	00	00	133	08	08	193	42	RCL
020	43	RCL	075	69	DP	134	54)	194	02	02
021	00	00	076	06	06	135	92	RTH	195	75	-
022	69	DP	077	69	DP	136	75	LSL	196	43	RCL
023	06	06	078	00	00	137	14	D	197	01	01
024	69	DP	079	43	RCL	138	98	ADV	198	54)
025	00	00	080	00	00	139	42	STO	199	55	+
026	91	R/S	081	85	+	140	05	05	200	43	RCL
027	75	LSL	082	02	2	141	99	PPT	201	05	05
028	12	8	083	07	7	142	98	ADV	202	95	=
029	42	STO	084	03	3	143	53	(203	42	STO
030	00	00	085	95	=	144	43	RCL	204	03	03
031	02	2	086	42	STO	145	02	02	205	01	1
032	01	1	087	00	00	146	75	-	206	93	.
033	00	0	088	91	R/S	147	43	RCL	207	08	8
034	00	0	089	75	LSL	148	01	01	208	08	8
035	00	0	090	16	A'	149	54)	209	03	3
036	00	0	091	42	STO	150	55	-	210	06	6
037	69	DP	092	07	07	151	43	RCL	211	05	5
038	04	04	093	53	(152	05	05	212	01	1
039	43	RCL	094	53	(153	95	=	213	06	6
040	00	00	095	43	RCL	154	42	STO	214	52	EE
041	69	DP	096	07	07	155	03	03	215	02	2
042	06	06	097	45	YX	156	03	3	216	03	3
043	69	DP	098	43	RCL	157	93	.	217	42	STO
044	00	00	099	09	09	158	07	7	218	08	08
045	75	-	100	65	X	159	04	4	219	04	4
046	03	3	101	53	(160	01	1	220	42	STO
047	02	2	102	53	(161	05	5	221	09	09
048	95	=	103	43	RCL	162	00	0	222	01	1
049	65	X	104	06	06	163	07	7	223	22	INV
050	05	5	105	45	YX	164	04	4	224	23	LHX
051	55	+	106	53	(165	52	EE	225	42	STO
052	09	9	107	01	1	166	04	4	226	06	06
053	85	+	108	04	4	167	42	STO	227	36	PGM
054	02	2	109	03	3	168	03	03	228	09	09
			110	03	3	169	05	5	229	14	D
			111	08	8	170	42	STO	230	22	INV
			112	93	.	171	09	09	231	52	EE
			113	03	3	172	01	1	232	99	PRT
						173	22	INV	233	98	ADV
									234	91	R/S

LIST OF REFERENCES

1. Khalil Sevrafi, *Electro Optical System Analysis*, pp. 127-143, 234-237. Electro-Optical Research Company, 1985.
2. Lloyd, J.M., *Thermal Imaging Systems*, pp. 18-66, Plenum Press, 1975.
3. Hudson, Richard Jr., *Infrared System Engineering*, pp. 1-60, 104-109, 557, John Wiley & Sons Inc., 1969.
4. Wolf, William L. and Zissis, George J., *The Infrared Handbook*, pp. 3-105 to 3-109, Office of Naval Research, Department of the Navy, 1966.
5. Ewing, G.C., *Oceanography From Space*, pp. 183-214, Woods Hole Oceanographic Institution, 1965.
6. Mc Alister, E.D., "Application of IR Optical Techniques to Oceanography", *Applied Optics*, Vol. 3, No 5, pp. 609, May 1954.
7. Cox, C. and Munk, W., *Bulletin of the Scripps Institution of Oceanography*, pp. 401-488, Vol. 6, 1956.
8. Bell, E.E., Eisner, L., Young, J., and Oetjen, R.A., "Spectral Radiance of Sky and Terrain at Wavelengths 1 and 20 microns. II Sky Measurements", *Journal of the Optical Society of America*, Vol. 50, pp. 1313-1320, December 1960.
9. Hobbs, Petter V. and Deepak, Adarsh, *Clouds, their Formation, Optical Properties and Effects*, Academic Press, 1981.
10. Feigel'son, E. M., *Radiation in a Cloudy Atmosphere*, pp. 221-225, D. Reidel Publishing Co.
11. Kneizys, F.X., and others, *Atmospheric Transmittance Radiance Computer Code LOWTRAN 6*, Air Force Geophysics Laboratory, AFGL-TR-83-0187, 1983.
12. AGA *Thermovision 780 Operating Manual*, publication No 556 556 492 Ed II, AGA Infrared Systems AB, 1980.
13. Due, Christopher T., *Optical - Mechanical, Active Passive Imaging Systems Volume II*, ERIM and Office of Naval Research- Department of the Navy, T53200-2-t II, 1982.
14. AGEMA Infrared Systems, *DISCO 3.0 Operating Manual*, publication Pharos Company, AGEMA, 1 July 1985.

INITIAL DISTRIBUTION LIST

		No. Copies
1.	Defense Technical Information Center Cameron Station Alexandria, Virginia 22304-6145	2
2.	Library, Code 0142 Naval Postgraduate School Monterey, California 93943-5002	2
3.	Department Chairman, Code 61 Department of Physics Naval Postgraduate School Monterey, California 93943	1
4.	Prof. A.W. Cooper, Code 61Cr Department of Physics Naval Postgraduate School Monterey, California 93943	3
5.	Prof. E.C. Crittenden, Code 61Ct Department of Physics Naval Postgraduate School Monterey, California 93943	1
6.	Department of the Navy Naval Environmental Prediction Research Facility Weapons Effects Assessment Division ATTN: John Cook Monterey, California 93943- 5006	1
7.	Hellenic Navy General Staff GEN / B2 Stratopedon Papagou Hollargos Athens GREECE	4
8.	George Dimitriadis 13-15 Xipetis St., GR-16121 Kaisariani Athens GREECE	5

220396

Thesis
D57648 Dimitriadis
c.1 Thermal image measure-
ments of infrared signa-
tures.

220396

Thesis
D57648 Dimitriadis
c.1 Thermal image measure-
ments of infrared signa-
tures.

thesD57648

Thermal image measurements of infrared s



3 2768 000 75861 9

DUDLEY KNOX LIBRARY